THE UNIVERSITY OF WARWICK

Library Declaration and Deposit Agreement

1. STUDENT DETAILS

Please complete the following:

Full name: …JIA YANG……

University ID number: …0866211……

2. THESIS DEPOSIT

2.1 I understand that under my registration at the University, I am required to deposit my thesis with the University in BOTH hard copy and in digital format. The digital version should normally be saved as a single pdf file.

2.2 The hard copy will be housed in the University Library. The digital version will be deposited in the University's Institutional Repository (WRAP). Unless otherwise indicated (see 2.3 below) this will be made openly accessible on the Internet and will be supplied to the British Library to be made available online via its Electronic Theses Online Service (EThOS) service.
[At present, theses submitted for a Master's degree by Research (MA, MSc, LLM, MS or MMedSci) are not being deposited in WRAP and not being made available via EthOS. This may change in future.]

2.3 In exceptional circumstances, the Chair of the Board of Graduate Studies may grant permission for an embargo to be placed on public access to the hard copy thesis for a limited period. It is also possible to apply separately for an embargo on the digital version. (Further information is available in the *Guide to Examinations for Higher Degrees by Research*.)

2.4 *If you are depositing a thesis for a Master's degree by Research, please complete section (a) below. For all other research degrees, please complete both sections (a) and (b) below:*

(a) Hard Copy

I hereby deposit a hard copy of my thesis in the University Library to be made publicly available to readers (please delete as appropriate) ~~EITHER~~ immediately ~~OR after an embargo period of …….. months/years as agreed by the Chair of the Board of Graduate Studies~~.

I agree that my thesis may be photocopied. YES / ~~NO~~ (*Please delete as appropriate*)

(b) Digital Copy

I hereby deposit a digital copy of my thesis to be held in WRAP and made available via EThOS.

Please choose one of the following options:

EITHER My thesis can be made publicly available online. YES / ~~NO~~ (*Please delete as appropriate*)

OR My thesis can be made publicly available only after…..[date] (Please give date)
YES / NO (*Please delete as appropriate*)

OR My full thesis cannot be made publicly available online but I am submitting a separately identified additional, abridged version that can be made available online.
YES / NO (*Please delete as appropriate*)

OR My thesis cannot be made publicly available online. YES / NO (*Please delete as appropriate*)

3. GRANTING OF NON-EXCLUSIVE RIGHTS

Whether I deposit my Work personally or through an assistant or other agent, I agree to the following:

Rights granted to the University of Warwick and the British Library and the user of the thesis through this agreement are non-exclusive. I retain all rights in the thesis in its present version or future versions. I agree that the institutional repository administrators and the British Library or their agents may, without changing content, digitise and migrate the thesis to any medium or format for the purpose of future preservation and accessibility.

4. DECLARATIONS

(a) I DECLARE THAT:

- I am the author and owner of the copyright in the thesis and/or I have the authority of the authors and owners of the copyright in the thesis to make this agreement. Reproduction of any part of this thesis for teaching or in academic or other forms of publication is subject to the normal limitations on the use of copyrighted materials and to the proper and full acknowledgement of its source.

- The digital version of the thesis I am supplying is the same version as the final, hard-bound copy submitted in completion of my degree, once any minor corrections have been completed.

- I have exercised reasonable care to ensure that the thesis is original, and does not to the best of my knowledge break any UK law or other Intellectual Property Right, or contain any confidential material.

- I understand that, through the medium of the Internet, files will be available to automated agents, and may be searched and copied by, for example, text mining and plagiarism detection software.

(b) IF I HAVE AGREED (in Section 2 above) TO MAKE MY THESIS PUBLICLY AVAILABLE DIGITALLY, I ALSO DECLARE THAT:

- I grant the University of Warwick and the British Library a licence to make available on the Internet the thesis in digitised format through the Institutional Repository and through the British Library via the EThOS service.

- If my thesis does include any substantial subsidiary material owned by third-party copyright holders, I have sought and obtained permission to include it in any version of my thesis available in digital format and that this permission encompasses the rights that I have granted to the University of Warwick and to the British Library.

5. LEGAL INFRINGEMENTS

I understand that neither the University of Warwick nor the British Library have any obligation to take legal action on behalf of myself, or other rights holders, in the event of infringement of intellectual property rights, breach of contract or of any other right, in the thesis.

Please sign this agreement and return it to the Graduate School Office when you submit your thesis.

Student's signature: .....…… Date: .....

Melting and Solidification Models and Thermal Characteristics of Microencapsulated Phase Change Materials

by

Jia Yang

A thesis submitted to The University of Warwick

for the degree of Doctor of Philosophy in Engineering

University of Warwick, Department of Engineering

March 2013

Table of Contents

List of Tables

List of Figures

Acknowledgements

The author thanks School of Engineering, The University of Warwick for the award of a studentship, and EPSRC for financial support of the experiments in this project.

My sincere appreciation goes to Prof. David Hutchins and Dr. Changying Zhao for their help and supervision.

I would like to thank senior electrical technician Mr. Stewart Edris, electronics laboratory technician Mr. Jonathan Meadows, Dr. Zhigen Wu and Mr. Guanhua Zhang for their help in development of the new test rig.

I acknowledge the contributions of Dr Roger Thorpe and Mr. Guanhua Zhang in measurements of thermophysical parameters of microcapsule phase change materials.

I acknowledge the suggestions offered by Prof. Robert Critoph and Dr. Zacharie Tamainot-Telto benefited my work on this thesis.

Finally, I want to thank my parents for their support and encouragement, as well as my husband Dr Fude Wang and my son James Wang for their support and beneficial academic discussions.

Declaration

This thesis is submitted to The University of Warwick in support of my application for the degree of Doctor of Philosophy. I hereby declare that this thesis is my own work and effort except where specifically stated. The theoretical analysis, proposal and construction of the new models, as well as development of all algorithm programs in this thesis were carried out by the author. The development of the new test rig and all experimental data presented were carried out by the author, or (where stated in Acknowledgement) by specialists under the author's direction.

Abstract

Microencapsulated phase change material (MPCM) as a new thermal energy storage material and a heat transfer medium have attracted considerable attention in the thermal energy storage field.

Solidification and melting models of a single PCM particle are constructed in this thesis. An effective numerical method for the problem of a spherical particle with a moving boundary was developed and validated by an iterative analytical series solution.

A new liquid-solid interface model was proposed for modelling the effect of binary phase composition on the solidification of an alloy and a mixture PCM particle based on solid fraction. A full two-phase melting model of differently-sized micro/nano particles was also built. The initial melting point of particles is defined and depends on the minimum melting temperature of particles measured by DSC, the particle size and the Gibbs-Thomson equation. The model can predict the melting time of micro-particles flowing in a heat transfer channel, which agrees with the group melting behaviour of MPCM as observed by experiments.

A test rig was built to explore the melting heat transfer behaviour of microcapsule phase change slurry (MPCS) flowing through a circular tube for a given constant heat flux.

DPNT06-0182 slurries were investigated on the test rig. The experimental results indicate that the flow rate is a key factor in determining heat transfer coefficients of slurries. For the same energy efficiency, and in the situation of low flow rate and phase change, the pressure drop and local heat transfer coefficients of 10% DPNT slurry are lower compared with water, but the most heat energy is stored during the passage through the heated test section. However, in the case of high flow rates and no phase change, the local heat transfer coefficients of 10% DPNT slurry are higher with comparison to water under turbulent flows.

Nomenclature

a_i, b_i, c_i	Coefficients in discretized equations of Implicit Euler Method
a_{li}, b_{li}, c_{li}	Coefficients in discretized equations of Implicit Euler Method of liquid phase
a_{sj}, b_{sj}, c_{sj}	Coefficients in discretized equations of Implicit Euler Method of solid phase
A_i	Tube inner surface area, m^2
$A_n(x)$	Coefficients in the expression of the iterative analytic series solution
$A_{11}(x)$, $A_{12}(x)$	Variables in the iterative analytic series solution
c	Specific heat capacity, $\mathrm{kJ(kgK)^{-1}}$
c_m	Mass concentration, %
$c_{p,eff}$	Effective specific heat capacity of slurry, $\mathrm{kJ(kgK)^{-1}}$
$c_{p,l}$	Specific heat capacity of carried fluid, $\mathrm{kJ(kgK)^{-1}}$
$c_{p,PCM}$	Specific heat capacity of PCM particles, $\mathrm{kJ(kgK)^{-1}}$
$c_{p,s}$	Specific heat capacity of a suspension, $\mathrm{kJ(kgK)^{-1}}$
$c_{p,w}$	Specific heat capacity of water, $\mathrm{kJ(kgK)^{-1}}$
$C_{12}(x)$	Variable in the iterative analytic series solution
cof_1, cof_2, cof_3	Intermediate variables in discretized equation of Implicit Euler Method
cof_{l1}, cof_{l2}, cof_{l3}	Intermediate variables in discretized equation of Implicit Euler Method of liquid phase

cof_{s1} , cof_{s2} , cof_{s3}	Intermediate variables in discretized equation of Implicit Euler Method of solid phase
D , D_i	Inside diameter of the tube, m
D_h	Hydraulic diameter, m
f_D	Darcy friction factor
f_s	Solid Fraction, $\%$
f_{ks}, $f_{(k+1)s}$	Solid fraction of discrete points in measurements, $\%$
$f_1(\delta)$	Variable in the iterative analytic series solution
h	Local convective heat transfer coefficient, $\mathrm{W(m^{-2}K^{-1})}$
k	Thermal conductivity, $\mathrm{W(mK)^{-1}}$
K , n	Quantities are defined to describe the power law fluids
K' , n'	Quantities are defined to describe the τ_w – flow characteristic curve
k_b	Conductivity of particles, $\mathrm{W(mK)^{-1}}$
k_e	Effective conductivity of composite, $\mathrm{W(mK)^{-1}}$
k_f	Conductivity of the liquid in a liquid matrix which contains a dispersion of particles , $\mathrm{W(mK)^{-1}}$
k_l	Thermal conductivity of liquid phase, $\mathrm{W(mK)^{-1}}$
k_r	Ratio of thermal conductivity in the solid phase to that in the liquid phase
k_s	Thermal conductivity of solid phase, $\mathrm{W(mK)^{-1}}$
k_w	Thermal conductivity of tube wall material, $\mathrm{W(mK)^{-1}}$

L	Latent heat of PCM, $\mathrm{kJ(kg)^{-1}}$;
	Length of the test tube, m
L_E	Hydrodynamic entrance length of a tube, m
$\dot{m}$	Mass rate of flow, $\mathrm{kg(s)^{-1}}$
n	Empirical shape factor
Nu_D	Nusselt number
P_r	Prandtl number
Q	Total heat supplied by the heater, W
Q_x	Heat supplied by the heater at the distance x to inlet of tube, W
q_w	Heat flux at the inner surface of wall, $\mathrm{Wm^{-2}}$
r	Dimensionless radial coordinate
r^*	Radial coordinate, m
R	Dimensionless position of liquid-solid interface
R_o	Outer tube radius, m
R_i	Inner tube radius, m
R^*	Position of liquid-solid interface, m
$R^*_{\max}$	Radius of sphere, m
$R^*_{\max,\min}$	Radius of the smallest particle, m
Re_D	Reynolds number
Re'	Generalized Reynolds number
t	Dimensionless time
t^*	Time, s

t_c	Time for complete solidification
t_{1c} , t_{2c} , t_{3c}	Three terms of t_c in the iterative analytic series solution
T	Dimensionless temperature of solid for single-phase solidification model
T_b , T_{bx}	Local bulk mean temperature, K
T_f	Dimensionless freezing temperature of liquid-solid interface
T_{in}	Temperature of tube inlet, K
T_l	Dimensionless temperature of liquid phase
$T_{mR}(R)$	Dimensionless melting point of a crystal of dimensionless radius R
T_s	Dimensionless temperature of solid phase
T_{bt}	Dimensionless shell boundary temperature of a particle as a function of dimensionless time
T^*	Temperature of solid for single-phase solidification model, K
T_b^*	(Initial) shell boundary temperature of a particle, K
T_{bt}^*	Shell boundary temperature of a particle as a function of time, K
T_f^*	Freezing temperature Freezing temperature of liquid-solid interface, K
T_{f1}^*	Maximum freezing temperature, K
T_{f2}^*	Minimum freezing temperature, K
T_i^*	Initial temperature of solid phase in melting model, K

T_k^*, T_{k+1}^*	Freezing temperatures of discrete points in measurements, K
T_l^*:	Temperature of liquid phase, K
T_m^* :	Bulk melting point, K
$T_{mR}^*\left(R^*\right)$	Melting point of a crystal of radius R^*, K
$T_{mR}^*\left(R_{\max}^*\right)$	Initial melting point of a micro/nano particle, K
$T_{m,\min}^*$	Minimum melting temperature of micro/nano PCM powder, K
T_s^*:	Temperature of solid phase, K
T_{wc}	Wall temperature based on Petukhov correlation, K
T_{wi}	Inner wall temperature of tube, K
T_{wim}	Based measurement inside wall temperature, K
T_{wo}	Outer wall temperature of tube, K
u_m	Mean velocity of fluid in a tube, ms^{-1}
$u_{mR}(R)$	Variable from $T_{mR}(R)$
$u(r,t)$	Defined variable from $T(r,t)$
$u_l(r,t)$	Defined variable from $T_l(r,t)$
$u_s(r,t)$	Defined variable from $T_s(r,t)$
v	Dimensionless cooling rate of shell boundary
v_x	Velocity profile in laminar flow, ms^{-1}
$\bar{v}_x$	Velocity profile in turbulent flow, ms^{-1}
v^+	Dimensionless velocity from the wall for turbulent fluid

v^* Cooling rate of shell boundary, Ks^{-1}

$v^*_{\max}$ Maximum cooling rate of shell boundary to obtain an equilibrium state structure, Ks^{-1}

V_p Particle volume fraction

x: Defined variable from dimensionless radial variables

x_l Defined variable from dimensionless radial variables of liquid phase

x_s Defined variable from dimensionless radial variables of solid phase

y: Defined variable to represent R

y^+ Dimensionless distance from the wall for turbulent fluid

$\hbar$ Variable in finite difference solution for singe-phase solidification model

$\hbar_l$ Variable in finite difference solution of liquid phase

$\hbar_s$ Variable in finite difference solution of solid phase

ΔP Pressure loss, Pa

ΔT_m Melting point depression for a small crystal, K

$8u_m/D_i$ Flow characteristic, s^{-1}

Greek symbols

α Thermal diffusivity, $\mathrm{m}^2\mathrm{s}^{-1}$

α_l Thermal diffusivity in liquid phase, $\mathrm{m}^2\mathrm{s}^{-1}$

α_s Thermal diffusivity in solid phase, $\mathrm{m}^2\mathrm{s}^{-1}$

α_r Ratio of thermal diffusivity in the solid phase to that in the liquid phase

γ Parameter in the iterative analytic series solution

$\dot{\gamma}_W$ Wall shear rate, s^{-1}

$\dot{\gamma}_{WN}$ Wall shear rate for a Newtonian fluid, s^{-1}

δ Calculate variable in the iterative analytic series solution;

Coefficient related to dimensionless liquid-solid interface temperature under the linear rule

$\delta_k, \delta_{kf1}, \delta_{kf2}$ Coefficients related to dimensionless liquid-solid interface temperature under the local linear rule

ε Roughness height, m

ζ Stefan number;

Coefficient in liquid-solid interface condition in binary phase solidification model

ζ' Stefan number in binary phase solidification model

ζ'' Dimensionless parameter in two-phase melting model

η Solidified volume fraction;

Coefficient related to dimensionless shell boundary temperature in binary phase solidification model

θ Dimensionless parameter in two-phase melting model

κ Variable in finite difference solution for liquid-solid two-phase

$\hat{\lambda}$ Defined variable in the Gibbs-Thomson equation, m

μ Dynamic viscosity, Pa s

μ_{ap} Apparent viscosity for pipe flow, Pa s

ρ	Density, kgm^{-3}
ρ_s	Density of crystal, kgm^{-3}
σ	Parameter in the iterative analytic series solution
σ_{sl}	Surface energy of the solid-liquid interface, Jm^{-2}
υ	Dimensionless parameter in two-phase melting model;
	Kinematic viscosity, $\mathrm{m}^2\mathrm{s}^{-1}$
τ_W	Wall shear stress, Pa
$\phi(x,y)$	Transformed variable from $u(r,t)$
$\phi_l(x_l,y)$	Transformed variable from $u_l(r,t)$
$\phi_s(x_s,y)$	Transformed variable from $u_s(r,t)$
$\varpi(\delta)$	Variable in the iterative analytic series solution
ψ	Dimensionless parameter in two-phase melting model

Chapter 1
Introduction

1.1 Motivation

The main motivation behind efforts to find more effective ways of utilising renewable energy is the increasing level of greenhouse gas emissions and the cost of fuel. One of the difficulties in using renewable sources of energy effectively is the development of suitable forms of energy storage. It is crucially important that the stored energy can be easily converted into its required form, and it is often quite challenging to achieve this. Solar energy is considered to be a particularly favourable source of renewable energy in many parts of the world. Suitable heat transfer and energy storage can improve performance and reliability of energy systems and help to conserve energy.

Latent heat energy storage is a particularly attractive approach, since it provides a high energy storage density. It can store the energy as the latent heat of fusion at a certain temperature, a value characteristic of the chosen phase change material (PCM). Indeed, one of the main applications of PCMs is to store thermal energy. In recent years, micro- or even nano-scale encapsulated PCMs can be produced in a large quantity, thanks to the rapid development of suitable manufacturing techniques. This can not only solve problems associated with the leakage of liquid (which can occur after a solid/liquid phase change of a PCM), but also the shell of the micro/nano-capsules can provide protection of PCMs by avoiding direct contact between

the PCMs and the heat transfer media. Encapsulated PCMs are one of the most promising solutions for the next generation of heat transfer media and thermal energy storage.

For microencapsulated PCM (MPCM) slurries, the heat transfer or storage performance depends on both the heat release or absorption rate per particle and the particle concentration (the number of particles per unit volume of the slurry) [1]. The factors influencing the heat transfer properties of a single particle are the liquid-solid interface location and the rate of phase change. Moreover, MPCM slurries can be used in mini-channels for cooling purposes, but it is unknown whether or not the melting process of the particles can be completed at the channel exit for such a short distance, particularly at a high flow speed. Accordingly, it is very important to study the phase change behavior of a single encapsulated PCM particle in order to obtain both the evolution of melting or solidification, and to determine the dynamics of the moving liquid-solid interface for a particular particle. Therefore one of the areas studied in this thesis is heat transfer during a phase change within a single encapsulated PCM particle, and development of effective melting or solidification models. This is needed in order to further analyze the thermal characteristics of microencapsulated PCM particles and slurries.

In addition, MPCM slurries have great potential to increase the efficiency of a pumped heat transfer system, and are also promising for application to thermal energy systems such as secondary refrigeration and air conditioning loops. Thus, another important motivation of this study was to develop effective methodologies in experiments and numerical methods for characterizing new and hybrid MPCM slurries, so as to be able to design

future MPCM slurries with optimal energy efficiency in a pumped heat transfer system.

1.2 Background

Thermal energy can be stored as a change in internal energy of a material as sensible heat, latent heat or thermochemical energy (or a combination of these) [2]. Latent heat of phase change is generated at a specific phase change temperature (for single materials) or over a phase change temperature range (for a more complicated situation involving mixtures). When a solid is heated to its melting temperature, the energy needed to melt the solid is referred to as the latent heat of fusion. In the reverse liquid-solid transformation, the energy released is referred to as the latent heat of crystallization. Latent heat in liquid-solid transitions has proved to be economical for use in thermal energy storage systems [3]. Any latent heat energy storage system possesses at least the following three components: a suitable PCM with its melting point in the desired temperature range; a suitable heat exchange surface, and a suitable container compatible with the PCM [3, 4].

There are large numbers of PCMs that melt and solidify at a wide range of temperatures, making them attractive in a number of applications such as heat pumps, solar engineering, and spacecraft thermal control [3]. However, due to a phase change involving a large amount of latent energy over small temperature ranges, PCMs are suitable for temperature stabilization and for storing heat with large energy densities in combination with rather small temperature changes [5]. It is preferable for PCMs to have a high melting enthalpy and a high density.

1.2.1 Phase change materials (PCMs)

There are a large number of PCMs that are available, and these can be classified into organic, inorganic and eutectic materials. This classification of PCMs is shown in Fig. 1.1. Paraffins and salt hydrates are two typical groups of PCMs. The organic paraffins are chemically and thermally stable and are not corrosive. However, they have a lower melting enthalpy and a lower density than some other types of PCM. Inorganic salt hydrates have a high melting enthalpy and a high density, but they are corrosive, exhibit sub-cooling in solidification and have cycling stability [6]. Metallics are likely candidates for high temperature operation because of the high latent heat per unit volume and high thermal conductivity. A eutectic is a minimum-melting composition of two or more components, each of which melts and freezes congruently forming a mixture of the component crystals during crystallization [7]. A eutectic alloy has the constant lowest melting point compared with other alloys which consist of the same components. The eutectic liquid has good fluidity because there is no proeutectoid phase precipitation, whilst eutectic crystals possess rather uniform compositions which make them have great potential in thermal energy storage systems.

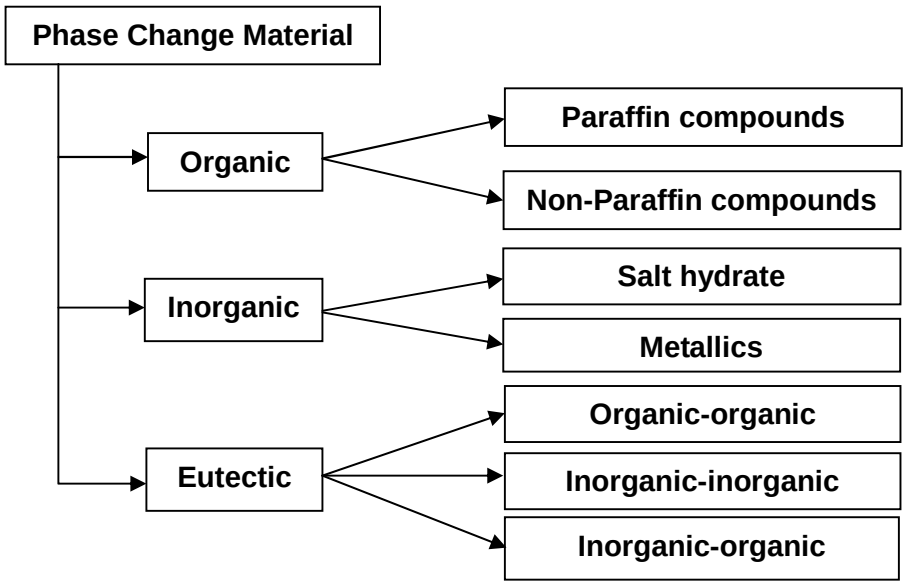

Figure 1.1: A simple classification system for PCMs [3]

The thermal conductivity of most PCMs is relatively low, and this problem can be solved in two ways [5]. The first method encapsulates the materials within small capsules or uses heat exchangers with large surface areas or low separate volumes of PCM. This can shorten the distance for heat transfer by conduction in the PCM. For example, the PCM can be encapsulated into spherical particles, and then integrated into a tank by mixing with a heat exchange fluid. A French company “Cristopia” developed such a product, called STL [8]. STL is composed of a tank filled with spherical balls, which are blow-moulded from a proprietary blend of polyolefins and filled with PCM. A range of PCMs allows thermal energy to be stored at temperatures between -33°C and +27°C. The spherical nodules are manufactured in 77 mm and 98 mm diameters for use at very low phase change temperatures (-18 to -33°C), intermediate phase change

temperatures (-3 to -15°C) and conventional building air conditioning ice storage temperature (0°C), respectively [8].

The second solution involves embedding structures of materials with high conductivity into the PCM. This can enhance the thermal conductivity. For example, the German company “SGL Carbon” developed this type of PCM with an ECOPHIT® graphite matrix. The composite materials produced the thermal conductivity values enhanced by a factor of up to 100 in comparison with pure PCM materials [9].

PCMs have been used in buildings to enhance the thermal comfort of lightweight construction since the 1970s [10], but there are several unsolved drawbacks. One occurs where the PCM is not encapsulated [11-12], and an uncontrolled factor is that they may change the properties of the building matrix material. Another arises for macrocapsules containing PCM [13], in that they may influence the safety of buildings and much more work need to be done at the building site; this means additional expenditure is required. Therefore none of these PCM products has been successfully integrated within the wider construction industry. However, progress in material science has made it possible to produce microcapsules whose structure and composition are controlled on the micro/nanoscale [14-15], and formaldehyde-free microencapsulation of paraffins has been proven to reduce limitations due to possible chemical contamination, and has allowed PCMs to be integrated into conventional construction materials [10].

In conventional heat exchange systems, thermal energy is transferred by the sensible heat of the single phase working fluid. If small temperature differences between source and sink are in operation, the single phase fluid

must be pumped at a high volume flow rate. This means a large amount of pumping power will be consumed. A fluid incorporating PCM can augment the efficiency of a pumped heat transfer system, since the PCM can increase the thermal capacity of the fluid due to the latent heat of phase change. Cleary et al. [16] found that the thermal capacity of an ice slurry could attain 2-4 times higher than that of chilled water. However, the PCM materials tended to clog heat transfer and distribution pipes, since non-encapsulated PCM particles are slightly sticky and coalesce to form large lumps [17]. Nevertheless, previous research has indicated that the problem may be solved by microencapsulating the PCM.

1.2.2 Microencapsulated phase change materials (MPCMs)

Microencapsulation may be achieved by a myriad of techniques and is usually categorized as falling within two groupings: chemical processes and physical processes. The chemical processes mainly include complex coacervation, interfacial polymerization (IFP) and in-situ polymerization. Physical processes include spray drying, fluid bed coating and the rotational suspension separation method [18]. For example, capsules containing n-octadecane with a melamine-formaldehyde shell can be fabricated by in-situ polymerization. Analytical measurements, using FT-IR (Fourier Transform Infrared) spectroscopy, SEM (scanning electron microscopy), DSC (differential scanning calorimetry) and TG (thermogravimetry) for example, can be used to explore the effects of stirring rate, the presence of an emulsifier, particle diameters, morphology, phase change properties and thermal stabilities of the capsules respectively [19]. In the commercial field, the company BASF has developed microencapsulated paraffin powder

products, known as Micronal® PCMs [20]. These products can be used as an emulsion or powder grade for modification of building materials of all types, with the purpose of adjusting the temperature of an internal room, and hence reducing costs in cooling and heating. In addition, MPCMs have been widely studied and used as active or pumped coolants, and in solar and nuclear heat storage systems as well as packed bed heat exchangers. They have also been used in the fabrication of thermo-regulated fibres, fabrics, coatings and foams [19]. The U.S. Navy has also investigated the use of MPCMs inside divers' dry suits to enhance thermal protection in extremely cold water applications [21].

1.2.3 Microcapsule phase change slurries (MPCS)

Microencapsulated powders can be fabricated into different mass fraction slurries with water. These slurries are often referred to as microcapsule phase change slurries (MPCS) when used as energy transport and storage media. MPCS have great potential in decreasing costs, as well as improving the energy efficiency of pumped cooling applications such as ventilation, air-conditioning, refrigeration and heat exchanger systems. An EU project has investigated the development of a MPCS which are stable enough to withstand the harsh conditions in piping systems [22]. The results indicated that microencapsulated paraffin can be pumped through a piping system for durations of up to 12 weeks. It was also shown that capsules with a smaller diameter, together with a thicker shell, have good stability. Natural convection of a MPCS was investigated by Diaconu et al. [23], using a 45% PCM concentration and a melting temperature range of approximately 4-7°C in a tank, fitted with a helically-coiled tube heat exchanger. They found that

the natural convection coefficient improved significantly during the phase change interval when compared to the performance of water. MPCS as the next-generation PCM slurries have thus attracted considerable attention.

1.2.4 Applications of MPCM and MPCS in thermal energy storage systems

The use of MPCM has become a new energy concept and has begun to be applied in the construction industry. MPCM usage has advantages when integrated within specially-optimized building materials. In principle, the capsule shell prevents contact between the PCM and the matrix material, and the microcapsules are small enough that there is almost no need to protect them against destruction. The distribution of the microcapsules in the wall offers a much larger heat exchange surface, so the heat transfer rate to charge and discharge the stored heat is increased. Air-conditioning consumes 15 percent of the total energy consumed in Europe [24], so there are significant potential benefits in making the use of MPCM an energy-efficient alternative.

Micronal® PCMs manufactured by the company BASF are a kind of formaldehyde-free MPCMs which have acted as a great role in the intelligent temperature management of building. Micronal® PCMs are designed for integration into various kinds of building materials and building systems, and can contribute towards a more comfortable indoor environment and a more optimal energy efficiency [25]. Micronal® PCMs present a durable and efficient method for isothermal storage of the peak loads, which usually occur during the day, in a defined temperature of human comfort range i.e. at 21°C, 23°C or 26°C, and releasing these again with a time delay (e.g. in the

evening time or at night). Micronal® PCMs can be incorporated into building materials in different forms, such as dispersions or slurries (microcapsules are dispersed in water) or as a powder (dry blends with plaster or cement mortar). The properties of some Micronal® PCM products are presented in Table 1.1. The microstructure of Micronal® DS 5001 power is illustrated in Fig.1.2. It can be seen from the surface morphology that the powder consists of various different micro-size spherical particles and the shape of most particles is very smooth, which helps to ensure that the MPCM is dispersed into the carrier fluids, e.g. water, the fluidity of slurry is good. Intelligent construction materials using this approach have been successfully demonstrated in the Badenova building in Offenburg and the Haus der Genwart in Munich [24].

Research into full-size rooms equipped with MPCM had been performed at Fraunhofer ISE, within project funded by the German government over five years [10]. At Fraunhofer ISE, the effect of MPCM was tested by the use of two full-size test rooms with a lightweight construction. Detailed measurement sensors were used in each room, and the interior walls of each room were coated with both a plaster containing MPCM and a conventional reference plaster. A dispersion-based plaster with 40% weight MPCM and 6mm thickness and a gypsum plaster with 20% weight PCM and 15mm thickness were tested for one year. The resulting temperature curves of a 6mm PCM plaster coating are presented in Fig.1.3. It is clear from the graph that the number of hours above 26 °C is noticeably less for the room coated with the MPCM material [10].

Table 1.1: Micronal® PCM products [25]

Product	Type	Melting point approx. (°C)	Solid content Approx.	Latent heat capacity approx. ($kJ(kg)^{-1}$)
DS 5000	Dispersion	26	42%	45
DS 5007	Dispersion	23	42%	41
DS 5030	Dispersion	21	42%	37
DS 5001	Powder	26		110
DS 5008	Powder	23		100
DS 5029	Powder	21		90

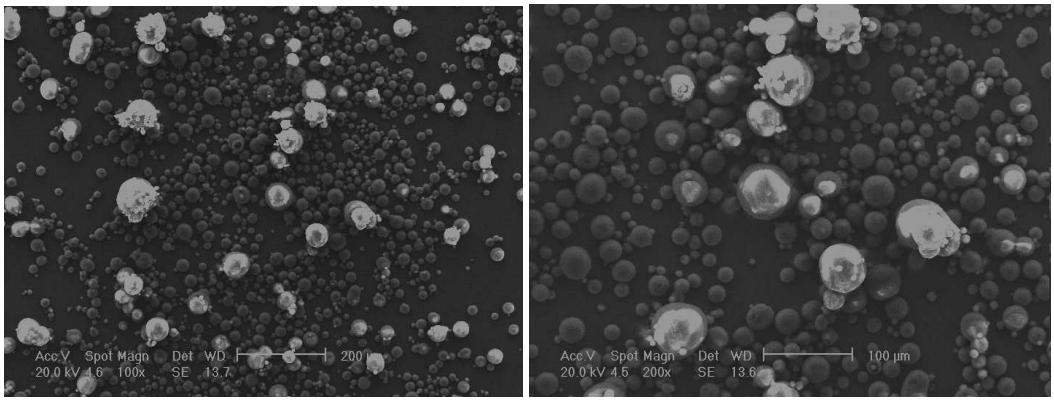

Figure 1.2: Microstructure of Micronal® DS 5001, observed using a Philips XL30 SEM

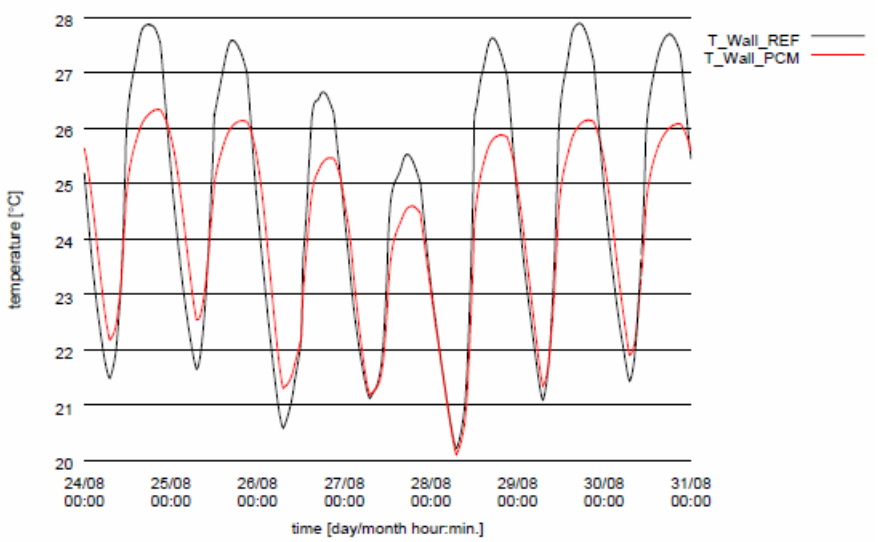

Figure 1.3: Measured wall-temperatures profiles in the two test rooms with night ventilation [10]. T_Wall_REF is for conventional plaster, and T-Wall_PCM for one containing MPCM.

It was reported that the application of MPCMs in concrete floors resulted in a reduction of maximum floor temperatures up to 16 ± 2% in the charging process, i.e. the thermal energy provided by the sun stored in a mix of concrete and PCMs. This was accompanied by an increase of minimum temperatures up to 7 ± 3% in the discharging process while PCMs was being released – in moderate sea climates during the evening and early night [26].

PCMs can also be used in domestic heating systems. A domestic electrical hot water cylinder incorporating encapsulated PCM placed in 57 vertical pipes was investigated by Gracia et al. [27]. The operational mode of the system was based on heating the water and melting the PCM during night time. After the first discharge of hot water, the PCM would transfer heat to the recently-introduced cold water, and hence increase its temperature without using electricity. The measured experimental data demonstrated the efficiency of the use of PCM in these systems.

One potentially large market sector is the electronics industry. Tan and Tso [28] investigated the cooling of mobile electronic devices experimentally, including personal digital assistants (PDAs) and wearable computers, using a heat storage unit (HSU) filled with the PCM of *n*-eicosane inside the device. The PCM in the HSU absorbed the heat dissipation from the chips and maintained the chip temperature below the allowable service temperature of 50°C for 2h of transient operations of the PDA. The effectiveness of HSU depends on the amount of PCM that was being used. The larger the amount of PCM, the longer it can stabilize the temperature of the PDA.

In addition, some experiments have been done to test some important parameters of MPCMs in other applications. Hunger et al. [29] directly mixed MPCM and concrete as well as studied its influence on the material properties. The result showed that the increasing PCM amounts resulted in a lower thermal conductivity and increased heat capacity, and therefore saved energy, but the work also indicated that a large fraction of the capsules were destroyed during the mixing process and paraffin wax was released into the surrounding matrix. However, the result of compressive strength experiments still met the requirements of most structural applications.

Rady [30] studied the thermal characteristics of granular phase change composites of small particle diameter (1–3 mm). Parameters including phase change temperature, latent heat, and energy storage capacity were determined using DSC and temperature-history methods. The author also concluded that the evolution of latent heat with temperature during phase change was related to the transformation of liquid fraction with temperature. The potential of the phase change composites for packed bed thermal

energy storage was investigated.

Revankar and Croy [31] presented the analysis of concentrated shrinkage voids in thermal energy storage systems employing PCM capsules. Rectangular flat plate, spherical, and torus shape capsules were chosen to investigate void formation. Transparent capsules such as cyclohexane, hexadecane, butanediol and octadecane were prepared for photographic analysis. They concluded that a low viscosity PCM (e.g. cyclohexane) and a high initial PCM temperature produced larger voids. In addition, a larger surface area provided faster cooling rates, and hence the initial voids were easily trapped - the correspondingly larger conduction depth then led to larger segregation of the voids.

Most PCMs used in low temperature applications have a very low thermal conductivity, which results in longer charging and discharging times. ECOPHIT [32] is a composite material developed by the SGL group which is designed to mitigate this problem. For example, the thermal conductivity of paraffin is 0.2 $W(mK)^{-1}$. However, the thermal conductivity of a composite with 85% volume paraffin and 10% volume expanded graphite can attain 25 $W(mK)^{-1}$. The resultant composite has great promise in active and passive air conditioning applications.

In energy storage and transportation applications, the advantage of MPCS is that the phase change with latent heat is involved, and thus the effective specific heat of the fluid is remarkably increased. However, the pumping power has to be considered when MPCS is used in a practical application [33]. Griffiths and Eames [34] have shown via four months of continuous testing that a concentration of 40% microcapsules MPCS can be

successfully used as the heat transfer fluid in a chilled ceiling application. It needed a significantly slower fluid flow rate, which reduced pumping requirements and allowed energy to be absorbed at a particular set point, thereby avoiding increases in panel surface temperature as gains increased. Wang et al. [35] proposed a low-energy air-conditioning strategy which was a combination of a cooled ceiling (CC), MPCS storage and evaporative cooling technologies. The assessment of evaporative cooling availability and utilization was done for five representative climatic cities in China, and the energy saving potential of the proposed air-conditioning system was analyzed using a well-validated building simulation code. The results indicated that the new system offers energy saving potential of up to 80% under North-Western Chinese climatic conditions, and up to 10% for the South-Eastern Chinese climate. Optimal design of the slurry storage tank depended on the slurry cooling storage behaviour and cooling demand variations of the ceiling panels.

1.3 State-of-the-art studies of MPCM and MPCS

The incorporation of MPCM and MPCS in a particular application calls for an analysis that will enable the researcher to optimize performances of thermal energy systems [36]. Experimental investigation, theoretical and numerical analysis are generally required to obtain appropriate solutions for the thermal behaviour of systems. Therefore, a large amount of research has been carried out to predict and analyse the behaviour of PCMs. This includes both theoretical and experimental studies.

1.3.1 Mathematical modelling and numerical analysis of PCM: a review

The phase transition of a material is described by a particular kind of boundary value problem, where the phase boundary can be allowed to move with time. This type of problem is named the Stefan problem after Jozef Stefan, the Slovenian physicist who introduced the general class of such problems in 1889 [37] in relation to problems of ice formation [36].

In initial studies of the Stefan problem, simple initial and boundary conditions as well as constant thermal properties are mainly considered for the one-dimensional case of an infinite or semi infinite region. These exact solutions usually take the form of functions of the single variable and are known as similarity solutions [38, 39]. In the last thirty years, an analytical iteration technique [40-41], a perturbation approach [42-43] and a semi-analytical technique [44-45] have been developed to solve the Stefan problem of a sphere or a cylinder. However, numerical methods are more convenient for solving Stefan-type problems in thermal engineering. On the other hand, numerical methods need to incorporate special mathematical transformations for changing the moving boundary into a fixed computational field. Relevant numerical methods [46-52] have thus been reported to exhibit solutions to one-dimensional Stefan problems of semi infinite region.

Although the Stefan problem is the most basic problem in a latent heat storage system, the behaviour of phase change systems is difficult to predict due to the inherent non-linear nature of moving interfaces. Alternately, by introducing an enthalpy method, the phase change problem becomes much

simpler, since the governing equation is the same for the two phases; interface conditions are automatically achieved, and create a mushy zone between the two phases [36]. An enthalpy function defined as a function of temperature is given by Voller [53] and this numerical method has been applied to various phase change problems [54–58]. For example, Voller [54] presented an enthalpy formulation based upon a fixed grid methodology in order to numerically solve the mushy region phase change problem controlled by convection-diffusion. The basic feature of the proposed method lies in the representation of the latent heat of evolution and complete freedom within the methodology to model a variety of phase change situations by suitable chosen sources. An application of this method was demonstrated by a test problem of freezing in a thermal cavity under natural convection. However, the enthalpy method can not be applied to more general problems, e.g. in that case that the melting temperature is not constant [59].

Since most PCMs have a low thermal conductivity, increasing the surface/volume ratio is important so as to increase the heat transfer rate. Spherical particles are preferable for heat storage applications, as they can store a larger amount of energy due to a more favorable ratio of volume to heat transfer surface area [60]. This can be done by packing a volume with a large number of PCM spherical capsules [61]. For example, spheres are often used in packed beds. Due to the complexity of such systems, it is often more efficient to first model the Stefan problem of an individual sphere, and to then describe it with a simple parametric model to be used in the packed bed modelling [36].

Numerical models have been studied extensively for many applications. Notably, the use of PCMs for thermal energy storage in solar heating system has received considerable attention. The heat storage capacities of different PCMs were investigated theoretically and experimentally in a cylindrical energy storage tank linked to a solar powered heat pump system by Esen et al. [62-64]. In the tank, the PCM was packed within cylinders, with the heat transfer fluid (HTF) flowing parallel to them. A simulation model defining the transient behaviour of the phase change unit was used and the heat transfer problem of the model was solved numerically by an enthalpy-based finite-difference method; the theoretical temperature and stored heat energy distribution within the tank were determined, and validated against experimental data.

Regin et al. [65] analysed the thermal behavior of a packed bed, composed of spherical capsules filled with paraffin wax as PCM, and used in a solar water heating system. The phase change phenomena of PCM inside the capsules were analyzed using the enthalpy method. The results indicated that the heat transfer coefficient, the Stefan number, the radius of capsules and the phase transition temperature range were the important factors which influenced the thermal performance in both charging and discharging processes.

Zhang et al. [66] simulated the effects of different PCM thermophysical properties (heat of fusion H_m, melting temperature T_m and thermal conductivity k) on the thermal performance of PCM wallboard for the residential buildings. In the study, an enthalpy method was applied for numerical simulation of PCM board. The nonlinear heat transfer

characteristics of the PCM wallboard was dealt with by taking enthalpy as the only variable instead of temperature and specific heat capacity. This simplified theoretical analysis method, called a ‘‘quasi-steady state” method, ignored the sensible heat of the wall when it was much smaller than the latent heat.

A mathematical model for a single rectangular duct filled with PCM has also been developed, based on an enthalpy formulation [67]. Here, the effect of PCM thickness on temperature distributions within the PCM and melting fraction was investigated. The results indicated that the melting time changed linearly with the amount of PCM, and that smaller thicknesses resulted in an improved performance.

Mosaffa et al. [68] recently presented a numerical solution of the performance enhancement of a free-cooling system, using a thermal energy storage (TES) unit employing multiple PCMs. The TES unit consisted of a number of rectangular channels containing flowing heat transfer fluid, separated by PCM slabs. The forced convective heat transfer inside the channels was analyzed by solving the energy equation, which was coupled with the heat conduction equation in the container wall. The melting and solidification problem of the PCM was solved using an effective heat capacity method. The system was optimized by the effect of design parameters such as PCM slab length, thickness and fluid passage gap on the storage performance.

Heat transfer fluid can flow through various physical configurations within PCM thermal energy storage devices. For this reason, U-tubes, U-tubes with in-line fins, U-tubes with staggered fins and a novel festoon design immersed

in a pool of PCM were evaluated numerically by Kurnia et al. [69]. The conjugate heat transfer between the heat transfer fluid and PCM, which underwent a cyclic melting and freezing process, was solved numerically using the method of computational fluid dynamics and enthalpy-porosity formulation. The simulations indicated that the novel festoon channel design would result in improved heat transfer rates for both charging and discharging stages.

P. Dolado et al. [70] developed models to simulate the performance of a TES unit in a real scale PCM-air heat exchanger. The modelling was accomplished by following two main paths: the thermal analysis of a single plate, and the thermal behaviour of the entire TES unit. The organic PCM utilized was macroencapsulated in aluminium rigid slabs, and the slabs were located parallel to the air flow in the TES unit. The models were based on a one-dimensional conduction analysis and were solved by an implicit finite difference method. The work used thermophysical data of the PCM that were measured in the laboratory.

An air source heat pump water heater which used PCM for thermal storage was designed by Long and Zhu [71] to take advantage of off-peak electrical energy. A quasi-steady state method was used to solve a based pure conduction formulation heat transfer model of PCM, and the temperature distribution and phase front location of PCM during thermal storage process were both calculated. A temperature and thermal resistance iteration approach was also developed for the analysis of temperature variations within the heat transfer fluid, and to determine the phase front location of PCM during the thermal release process.

Finally, it is necessary to mention the specific field of quantum mechanics, molecular dynamics and multiple-scale approaches. The above-mentioned fields provide novel approaches to the analysis of micro- and nano-particles in heat energy storage systems. Liu et al. [72] summarized the strengths and limitations of currently available multiple-scale techniques and presented the latest perspective approaches such as the bridging scale method, multi-scale boundary conditions, and multi-scale fluidics.

1.3.2 Experimental investigation and numerical analysis on convective heat transfer of MPCS: a review

MPCS present potential advantages when used as pumpable heat transfer fluids and as heat storage materials, but there is a lack of technical experience. The main issues encountered as a thermal storage material are sub-cooling and the unstable processes presented by slurries [73]. This research field was first explored by Charunyakor et al. [1]. They formulated a model for heat transfer of MPCS flow in circular ducts based on the energy equation. Heat generation or absorption due to phase change in the particles was derived from solutions for the solidification of a sphere, and included in the energy equation as a source term. The enhancement of thermal conductivity due to the particle/fluid interactions was also taken into consideration. Results have demonstrated that bulk Stefan number and MPCS concentration are the dominant governing parameters in the system for low temperature applications.

Experimental investigation has been reported by Goel et al. [74] for a suspension of *n*-eicosane microcapsules in water flowing in a circular duct with a constant wall heat flux. The suspension was in a state of fully-

developed laminar flow, and the inlet temperature of the suspension was maintained at or below the melting point of the PCM. The results indicated that the PCM suspensions can reduce the rise in wall temperature by up to 50% as compared to a single phase fluid for the same non-dimensional parameters. This experimental result has become the validation evidence for most of the later numerical studies reported in the literature. However, *n*-eicosane microcapsules have a melting temperature range and a freezing temperature range, and sub-cooling clearly occurs on freezing [75]. Generally, the melting point denotes the peak value of the melting temperature range. If the temperature of the inlet was not lower than the lowest freezing point of the PCM, there is an implication that the PCM microcapsule cannot be guaranteed to be in the solid state, and phase change may occur only partially during the heating test section. From these two initial studies, we find that the two primary parameters they determined, either the bulk Stefan number or the volumetric concentration, had no relationship with flow rate. The conclusion that the bulk Stefan number was found to be the most dominant parameter is questionable, because mass flow rate is one of most important factor which influences the bulk mean temperature of fluid. In the cases of higher flow rates, the phase change cannot occur, and for this situation, the Stefan number is irrelevant since no latent heat is stored.

Zhang and Faghri [76] improved the laminar forced convection heat transfer model of Charunyakor [1], and used a temperature transforming model instead of quasi-steady model to solve the melting of a spherical particle. Three factors i.e., the microcapsule's crust, the initial subcooling,

and the fact that melting takes place over a range of temperatures below the melting point of PCM were considered for modelling their effects on the variation of the dimensionless tube wall temperatures. The results showed that the effect of MPCM on the forced convective heat transfer in a tube can be significantly reduced by increasing the width of the phase change temperature range, and the authors suggested that further experimental work was necessary to better determine the width of the phase change temperature range.

It should be noted that these models using spherical solidification (or melting) source terms are very complicated, and are not easily implemented using standard computer-based fluid dynamics packages. For this reason, a simple effective specific heat capacity model was proposed [77, 78] and applied by Roy and Avanic [79] to turbulent heat transfer for MPCS in a circular tube with a constant wall heat flux. The numerical predictions were found to agree with the experimental results of Choi [80, 81]. Further work by Hu and Zhang [82, 83] used an effective specific heat capacity to analyze the forced convective heat transfer enhancement of MPCS flowing through a circular tube with constant heat flux as well as constant wall temperature. They validated the model by comparisons with the above mentioned experimental and numerical results.

In summary, the previous numerical studies use dimensionless parameters (dimensionless wall temperature, Nussselt number etc.) to evaluate the heat transfer of MPCS following a circular tube under laminar or turbulent conditions. These studies agree that the most influential parameter is the Stefan number. Due to these results being dependent on numerous

assumptions, it is difficult to obtain firm conclusions for analysing the performance of a practical MPCS heat transfer system directly from the models.

The lack of a general and systematic study makes it difficult to interpret or evaluate many of the previous results. However, some relevant experimental studies have been reported. For example, Choi et al. [81] investigated convection heat transfer with PCM slurries in turbulent flow of a circular tube on a test rig with a long heating section (627 diameters). The results indicated the pressure drop significantly decreased at the point where the PCM particles in the slurry melted. The local convective heat transfer coefficient increased in the region where the bulk mean temperature was below the melting temperature of the PCM, decreased sharply where phase change occurred, and increased again slightly further downstream in region with no solid particles existed. Yamagishi *et al.* [84] experimentally investigated the hydrodynamic and heat transfer characteristics of MPCS, consisting of octadecane (C18H38) contained in 2-10 μm diameter particles, for use as a heat transfer fluid. Both the pressure drop and local convective heat transfer coefficients of slurry flowing within a circular tube with a uniform heat flux were measured. The results showed that increases in particle volume fractions caused the structure of the flow to change from turbulent to laminar, and under the same flow rate conditions the pressure-drop reduced compared to single phase water. When the MPCM melted, the local heat-transfer coefficients for turbulent flow increased relative to those for non-melting slurry. However, the local heat transfer coefficients for the turbulent flow of MPCS exhibiting a phase change were not greater than those for the

flow of pure water at the same mean flow velocity. They explained that high heating rates from the tube wall were necessary for the complete melting of the slurry within the limited-length test section, and therefore, a large increase in the effective specific heat (which they defined) was difficult to achieve. They also indicated that the heat transfer performance of MPCS is strongly related to the flow conditions. Alvarado et al. [85] also obtained lower heat transfer coefficients in comparison to water at the same velocities under turbulent conditions via experiments. In contrast, the study of Wang et al. [86] showed that heat transfer coefficients of MPCS were significantly higher than for those for single-phase fluid flow in laminar conditions, but exhibited more complicated phenomena at low turbulent conditions. They concluded that a higher volume fraction of solid particles may further degrade the heat transfer performance, in agreement with the predictions of Liu et al. [87].

Experiments under conditions of laminar flow were carried out by Rao et al. for MPCS through rectangular copper mini-channels at varying mass flow rates [88]. They concluded that the cooling performance of MPCS depended strongly on the mass flow rate and the MPCM mass concentration. Suspensions with higher mass concentrations were only more effective than water at low mass flow rates.

In the recent study by Sabbah et al. [89, 90], significant enhancements in heat transfer coefficient (higher than 50%) and reductions in tube wall temperature (higher than 40%) were obtained, and the heat transfer enhancement curves were similar in shape to the expected MPCM specific heat capacity curve. Delgado et al. [73] analyzed the causes of the system

errors in experimental installations and proposed a new methodology for the determination of convective heat transfer coefficients. The results demonstrated an improvement of approximately 25% on the convective heat transfer coefficient when compared to water in laminar conditions.

1.3.3 Discussion

As seen from the above analysis, existing theoretical and experimental studies have not obtained clear conclusions especially in turbulent flow. The existing results for the heat transfer behaviour of MPCS, even if in the simplest circular tube to give a constant heat flux, are incomplete and conflictive in some cases. Table 1.2 summarizes the current research.

It has been demonstrated above that MPCM has received considerable interests from both academic and industrial fields as a new energy storage material, but less attention has been paid to the effect of latent heat in a single encapsulated particle. However, analyzing the thermal characteristics of a single particle is the most important theoretical basis for modelling MPCM behaviour, when in use as either a heat transfer medium or as the material within an energy storage system. In addition, existing studies have not presented clear evidence on the improvement of heat transfer for MPCS in comparison to a single phase flow. It is imperative to clarify the effect of various factors that take place within a MPCS system, if such approaches are to be used in practice.

Table 1.2: Summary of current research

Methods	Solutions	Method of heat transfer estimation	Dominant governing parameters	Laminar flow	Turbulent flow
Numerical investigation	Use melting or solidification model of a sphere; effective specific heat capacity model; energy equation	Dimensionless wall temperature; local or modified local Nussselt number.	Bulk Stefan number MPCS concentration	Heat transfer enhancement	Local Wall temperatures decrease
Experimental investigation	Experiments on a Test rig	Local heat transfer coefficient	Flow rate MPCS concentration	Local heat transfer coefficients increase compared with water	Local heat transfer coefficients decrease or increase as MPCM melt is uncertain; Heat transfer coefficients decrease compared with water

1.4 Outline of the thesis

We can classify some important influential factors which should be considered in a more extensive analysis of MPCS systems into two types. One class involves the thermophysical properties of MPCM, such as the melting temperature range, the degree of sub-cooling and viscosity characteristics. These properties can be measured experimentally. Another class is related to more complicated cases which can not be directly measured by instruments and devices, for example, the unknown melting time of MPCM particles when they flow through a heating test tube. This class of problem will have to be solved by building a theoretical model and employing a suitable numerical algorithm. Furthermore, these factors can be combined with hydrodynamic conditions and heat flux conditions in order to quantify the latent heat effect of MPCM particles. The result would be a more complete analysis for the melting heat transfer behaviour of MPCS.

The research in this thesis mainly concentrates on two aspects of this problem: melting/solidification models for a single MPCM particle, and the melting heat transfer characteristics of novel MPCS, including both theoretical and experimental studies.

This thesis consists of 7 Chapters. Chapter 1 has presented the motivation for this study, and introduces the background and reviews state-of-the-art studies of MPCM and MPCS. In Chapter 2, a spherical solidification model will be built for a single encapsulated PCM particle, and a robust and effective numerical method will be developed to solve the solidification of a sphere with a moving boundary; this numerical method will be used as a basic algorithm to solve more complicated phase change models in Chapters

3 and 6. In Chapter 3, a new liquid-solid interface model is proposed and solved for alloys and mixture materials; furthermore, a full two-phase model and solution for melting of differently-sized micro/nano PCM particles will be presented. Chapter 4 will demonstrate a test rig, which is designed and developed to realize a melting heat transfer of MPCS flowing through a circular tube for a given constant heat flux. In Chapter 5, experimental results of DPNT06-0182 slurries with different mass fractions of MPCM particles on the test rig will be presented and discussed. Chapter 6 will analyze the melting behavior of micro-particles of DPNT06-0182 slurries in a heat transfer pipe flow. Finally, Chapter 7 presents the main conclusions arising from this work, and suggests future areas of research.

Chapter 2

Solidification model for a single encapsulated PCM particle

Summary

The heat diffusion equation of a sphere with a liquid-solid moving interface model is used to analyze the solidification of PCM within a single encapsulated particle. The nonlinearities associated with a moving boundary problem are simplified via the transformation of dimensionless variables within the relevant equations. A technique which combines the Explicit Euler method with the Implicit Euler method within a finite difference scheme is thus developed to solve the Stefan problem. The results are compared to those of an iterative analytical series solution, and good agreement is obtained. The evolution of both solidification and the moving front surface are predicted for different particle sizes, with paraffin encapsulated within the core, and the solidified volume fraction as a function of time is also determined.

2.1 Solution analysis for inward solidification of a sphere

Among various shapes of encapsulated particles, spherical particles are the most preferred for various applications. This is because they can store a larger amount of energy than other volumetric shapes, due to a more favorable ratio of volume to heat transfer surface area [60]. For this reason, the heat conduction or diffusion equation of a sphere with a liquid-solid

moving interface model is investigated in this Chapter, and a method is proposed to describe the solidification process (the Stefan problem) of a single encapsulated PCM particle.

For solidification within a sphere containing initially molten PCM inside, solid transformation starts from the outer shell due to the wall temperature being below the freezing point, and develops inward to the centre until all the liquid changes into solid [60, 91]. However, it is difficult to analytically calculate the inward solidification, due to the moving liquid-solid interface that exists during the phase change stage. In the previous research, Shih et al. [40, 41] obtained an analytical solution for the solidification of cylinders and spheres with constant heat transfer coefficient by using an analytical iteration technique. The success of this method lies in transforming the diffusion equation from cylindrical coordinates or spherical coordinates into a form of rectangular configuration with position-dependent coefficients. Moreover, a perturbation approach has been applied to obtain the analytical solution for spherical solidification. Due to the divergence of the regular perturbation solution when the freezing front approaches towards the center of the spherical particle, the method of strained coordinates was used by Pedroso and Domoto [42]. The treatment, which assumed that the parameter β (the ratio of the latent heat to the sensible heat of the substance) was large, was adopted in the analytical solution by Riley et al. [43]. Another semi-analytical technique which simplifies the non-linearity associated with the moving boundary and enables an iterative analytic series solution was proposed by Davis and Hill [44] and the technique was further developed in [45] to give successive estimates of the time for complete solidification of a sphere.

However, the analytical solution is not able to solve more complicated thermophysical problems which are sometimes encountered. Therefore, numerical methods are also appropriate for solving Stefan problems. Numerical methods have been reported which effectively work out the general one-dimensional Stefan problem [46-52]. Initially, an explicit finite difference (FD) method was used for the Stefan problem with time-dependent boundary conditions and compared with the nodal integral method. High accuracy and agreement can be obtained for both solutions [46]. The variable space grid method based on an FD approach was further used by Savovic and Caldwell [47] and the result exhibited good agreement with the exact solution. In addition, the FD method was also used to solve one-dimensional Stefan problem with periodic boundary conditions [48]. The weak or Galerkin formulation of the initial-boundary value problem was also used to derive a system of initial-value problems in ordinary differential equations by Asaithambi in a one-dimensional Stefan problem [51, 52]. Furthermore, the full two-phase Stefan problem has been considered by applying a small-time perturbation scheme and by presenting numerical results calculated using an enthalpy method [92]. The two methods of matched asymptotic expansions and a finite difference scheme based on the enthalpy method were used by Tabakova et al. for the freezing of a supercooled spherical droplet [93].

In this chapter, the above work is extended via a technique which combines numerical calculations with the transformation of dimensionless variables in equations. The purpose of transforming variables is to simplify the moving boundary problem to one with a fixed boundary for the diffusion

equation of a sphere. Based on the transformed dimensionless variables and the new boundary conditions, an FD method is developed, and the results are compared to an iterative analytical series solution [44]. The evolution of the solidification and the temperature profile in the solidified region is also predicted and discussed. In addition, the solidification of differently-sized particles within a core of encapsulated paraffin PCM is analyzed in detail.

2.2 The spherical solidification model

A 1D model of a partially-solidified PCM sphere is shown in Fig. 2.1, and shows a solidified region surrounding an inner liquid core. The outer radius of the sphere is $R^*_{\max}$.

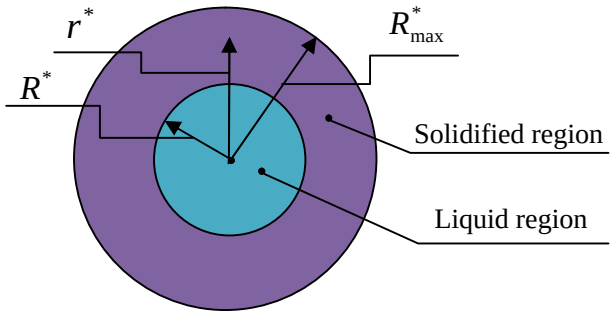

Figure 2.1: Inward solidification of a spherical PCM particle

During the solidification stage, the two phases (liquid and solid) co-exist until the solidification process is completed. Heat conduction within the outer solid region is the sole transport mechanism, assuming that the temperature of the liquid is uniform and is equal to the fusion temperature, thereby precluding the possibility of natural convection.

The heat transfer equation in the solid area can be described by:

$$\frac{\partial T^*}{\partial t^*} = \alpha\left(\frac{2}{r^*}\frac{\partial T^*}{\partial r^*} + \frac{\partial^2 T^*}{\partial r^{*2}}\right) \qquad R^* < r^* < R^*_{\max} \ , \tag{2.1}$$

where T^* is the temperature of solid, t^* is time; r^* is the radial coordinate within the solid region; α is the thermal diffusivity in the solid phase, where $\alpha = k/\rho c$; k is thermal conductivity; ρ is density and c is specific heat capacity.

The boundary condition that is used is:

$$T^* = T^*_b \qquad at \qquad r^* = R^*_{\max} \ , \tag{2.2}$$

where T^*_b is the boundary temperature of a particle (assumed to be a constant and lower than the freezing point). The condition of the liquid-solid interface can be expressed as:

$$T^* = T^*_f \quad at \quad r^* = R^* \ , \tag{2.3}$$

where T^*_f is the freezing temperature. Moreover, if L is the latent heat of the PCM in the liquid-solid interface, the heat balance equation can be written as:

$$\rho L \frac{dR^*}{dt^*} = k \frac{\partial T^*}{\partial r^*}\Big|_{R^*} \ , \tag{2.4}$$

noting that the initial condition is:

$$R^*\big|_{t=0} = R^*_{\max} \ . \tag{2.5}$$

The relevant dimensionless variables are defined as [45]:

$$T = \frac{T^*_f - T^*}{T^*_f - T^*_b} \quad r = \frac{r^*}{R^*_{\max}} \quad R = \frac{R^*}{R^*_{\max}} \quad t = \frac{\alpha t^*}{R^{*2}_{\max}} \ . \tag{2.6}$$

The dimensionless forms of Equation (2.1) – (2.5) can be constructed as follows:

$$\frac{\partial T}{\partial t} = \frac{2}{r}\frac{\partial T}{\partial r} + \frac{\partial^2 T}{\partial r^2} \qquad R(t) < r < 1 \tag{2.7}$$

$$T = 1 \quad at \quad r = 1 \tag{2.8}$$

$$T = 0 \quad at \quad r = R(t) \tag{2.9}$$

$$\frac{dR}{dt} = -\zeta \frac{\partial T}{\partial r}\Big|_R \tag{2.10}$$

$$R\big|_{t=0} = 1 \tag{2.11}$$

Here, $\zeta = \dfrac{c\left(T_f^* - T_b^*\right)}{L}$ is the Stefan number.

2.3 Methods of solution

By use of the transformation $u(r,t) = T(r,t)r$, equation (2.7) can be further simplified and equations (2.7) – (2.10) are changed into:

$$\frac{\partial u}{\partial t} = \frac{\partial^2 u}{\partial r^2} \quad R(t) < r < 1 \tag{2.12}$$

$$u = 1 \quad at \quad r = 1 \tag{2.13}$$

$$u = 0 \quad at \quad r = R(t) \tag{2.14}$$

$$\frac{dR}{dt} = -\frac{\zeta}{R}\frac{\partial u}{\partial r}\Big|_R \tag{2.15}$$

The above equations deal with the moving boundary problem. In the one-dimensional Stefan problems associated with a moving boundary, a coordinate transformation can be used to transform the changing physical domain into a fixed computational domain in the first steps of the solution [44, 51, 52]. The coordinate transformation depends on the geometrical domain

of solidification. For this Stefan problem of a sphere, $u(r,t)=\phi(x,y)$ is assumed, and both $x=(r-1)/[R(t)-1]$, $y=R(t)$ are defined.

Consider the following expressions:

$$du=\frac{\partial u}{\partial t}dt+\frac{\partial u}{\partial r}dr \tag{2.16}$$

$$d\phi=\frac{\partial \phi}{\partial x}dx+\frac{\partial \phi}{\partial y}dy \tag{2.17}$$

$$\frac{\partial u}{\partial t}=\frac{\partial \phi}{\partial x}\frac{\partial x}{\partial t}+\frac{\partial \phi}{\partial y}\frac{\partial y}{\partial t}=-\frac{\partial \phi}{\partial x}\frac{xR'(t)}{R(t)-1}+\frac{\partial \phi}{\partial y}R'(t) \tag{2.18}$$

$$\frac{\partial u}{\partial r}=\frac{\partial \phi}{\partial x}\frac{\partial x}{\partial r}+\frac{\partial \phi}{\partial y}\frac{\partial y}{\partial r}=\frac{\partial \phi}{\partial x}\frac{1}{R(t)-1} \tag{2.19}$$

$$\frac{\partial^2 u}{\partial r^2}=\frac{\partial}{\partial x}\left(\frac{\partial u}{\partial r}\right)\frac{\partial x}{\partial r}+\frac{\partial}{\partial y}\left(\frac{\partial u}{\partial r}\right)\frac{\partial y}{\partial r}=\frac{\partial^2 \phi}{\partial x^2}\left(\frac{1}{R(t)-1}\right)^2 \tag{2.20}$$

Because of these, equations (2.12) - (2.15) and (2.11) become:

$$y\frac{\partial^2 \phi}{\partial x^2}=\zeta\frac{\partial \phi}{\partial x}(1,y)\left[x\frac{\partial \phi}{\partial x}-(y-1)\frac{\partial \phi}{\partial y}\right] \tag{2.21}$$

$$\phi(x,y)=1 \quad at \quad x=0 \tag{2.22}$$

$$\phi(x,y)=0 \quad at \quad x=1 \tag{2.23}$$

$$\frac{\partial \phi}{\partial x}(1,y)=-\frac{y(y-1)}{\zeta}\frac{dy}{dt} \tag{2.24}$$

$$y\big|_{t=0}=1 \tag{2.25}$$

As seen in equation (2.23), the condition of liquid-solid interface is presented by the new variable x. This means that the problem is changed from that seen in equation (2.14), which is a moving boundary condition with time, to one that is fixed. An FD solution can then be developed to solve the

transformed equations.

2.3.1 Finite difference solution

In the FD solution, h is the space grid size for the variable x, and $i=0,1,2,\cdots,M$ is set for grid points of x. Here, $i=0$ corresponds to the position of the liquid-solid interface, and $i=M$ is towards the position of outer boundary of the sphere. Δt is the time step. $\phi_0^n, \phi_1^n \; and \; \phi_2^n$ are neighbouring points within the solidified region front at a time $n\Delta t$. If it is supposed that $\hbar$ represents the second-order difference for $\frac{\partial \phi}{\partial x}(1,y)$, then $\hbar = \frac{3\phi_0^n - 4\phi_1^n + \phi_2^n}{2h}$, and the forward Euler scheme for the time derivative is employed to make equation (2.24) discrete. Equation (24) can be expressed in discretized form as:

$$y^{n+1} = y^n - \frac{\zeta \hbar \Delta t}{y^n\left(y^n - 1\right)} \; . \tag{2.26}$$

Since the new position of the moving front y at time $(n+1)\Delta t$ has been determined by the iterative equation (2.26), then equation (2.21) will solve the only unkown new position of variable ϕ, and hence the Implicit Euler method can be applied to equation (2.21) in order to improve stability and accuracy. The following discretized form for equation (2.21) is produced by the Implicit Euler scheme for the time derivative and the central difference scheme for the space derivative.

$$y^{n+1}\left(\frac{\phi_{i+1}^{n+1} - 2\phi_i^{n+1} + \phi_{i-1}^{n+1}}{h^2}\right) = \zeta \hbar \left(x_i^{n+1} \frac{\phi_{i-1}^{n+1} - \phi_{i+1}^{n+1}}{2h} - \left(y^{n+1} - 1\right)\frac{\phi_i^{n+1} - \phi_i^n}{y^{n+1} - y^n} \right) \tag{2.27}$$

The truncation error is $O\left(h^2\right)$ for the space derivative and the solution is first-order in time.

The equation (2.27) can be simplified as:

$$a_i\phi_{i-1}^{n+1}+b_i\phi_i^{n+1}+c_i\phi_{i+1}^{n+1}=\phi_i^{n}\ , \tag{2.28}$$

where

$$a_i=\frac{cof_1-cof_3}{cof_2},\ b_i=1-\frac{2cof_1}{cof_2},\ c_i=\frac{\left(cof_1+cof_3\right)}{cof_2}$$

$$cof_1=\frac{y^{n+1}}{\zeta\hbar h^2},\ cof_2=\frac{y^{n+1}-1}{y^{n+1}-y^{n}},\ cof_3=\frac{x_i^{n+1}}{2h}.$$

Equation (2.28) can be written into a matrix form, as follows:

$$\begin{bmatrix} b_1 & c_1 & 0 & \cdots & \cdots & 0 \\ a_2 & b_2 & c_2 & 0 & \cdots & 0 \\ \cdots & \cdots & \cdots & \cdots & \cdots & 0 \\ 0 & \cdots & 0 & a_{M-2} & b_{M-2} & c_{M-2} \\ 0 & 0 & 0 & 0 & a_{M-1} & b_{M-1} \end{bmatrix}\begin{bmatrix} \phi_1^{n+1} \\ \phi_2^{n+1} \\ \cdots \\ \phi_{M-2}^{n+1} \\ \phi_{M-1}^{n+1} \end{bmatrix}=\begin{bmatrix} \phi_1^{n}-a_1\phi_0^{n+1} \\ \phi_2^{n} \\ \cdots \\ \phi_{M-2}^{n} \\ \phi_{M-1}^{n}-c_{M-1}\phi_M^{n+1} \end{bmatrix} \tag{2.29}$$

In this way, the tridiagonal matrix algorithm (TDMA) can be used to solve equation (2.28).

The initial profile is important if the numerical procedure is to attain a high accuracy. Savovic and Caldwell *et al*. [47, 48] used the relevant exact solution to initialize their numerical procedures for solving one-dimensional Stefan problems. Since the exact solution of this Stefan problem is unavailable, the initial profile of temperature distribution in the solidified region may be derived from the analytical solution of the relevant problems. Here an iterative analytical series solution for the moving boundary problems of a sphere is adopted.

2.3.2 Iterative analytical series solution

The iterative analytical series solution was developed to solve the moving boundary problems of a sphere by Davis and Hill [44]. It is an approximate analytical solution which avoids the difficulty of a regular perturbation series solution by appropriate choice of variables [45]. The convergence of the analytical series method was first checked in the freezing of a sphere under the convective boundary condition in reference [45]. The numerical values of successive estimates time t_c for complete solidification under the three different terms in the expression of t_c indicated the satisfactory convergence. In this solution, equation (2.30) is the expression of the transformed variable $\phi(x, y)$.

$$\phi(x, y) = \sum_{n=0}^{\infty} A_n(x)(y-1)^n \tag{2.30}$$

If we only consider the first two terms of equation (2.30), the following equations are obtained from the original derivation in [44] to carry out the calculation of $\phi(x, y)$ for the Stefan problem which we build in this chapter.

$$A_0(x) = \int_x^1 e^{-\gamma\lambda^2/2}\, d\lambda \left\{ \int_0^1 e^{-\gamma\lambda^2/2}\, d\lambda \right\}^{-1} \tag{2.31}$$

$$A_1(x) = \int_0^x \frac{f_1(\delta)}{\varpi(\delta)} [A_{11}(x)A_{12}(\delta) - A_{11}(\delta)A_{12}(x)] d\delta + C_{12}A_{12}(x) \tag{2.32}$$

$$f_1(\delta) = -\frac{3\gamma^2 \delta e^{\gamma(1-\delta^2)/2}}{\zeta(3+\gamma)} \tag{2.33}$$

$$\varpi(\delta) = -e^{-\gamma\delta^2/2} \tag{2.34}$$

$$A_{11}(x) = e^{-\gamma x^2/2} + \gamma x \int_0^x e^{-\gamma \lambda^2/2}\, d\lambda \tag{2.35}$$

$$A_{12}(x) = x \tag{2.36}$$

$$C_{12} = \int_0^1 \frac{f_1(\delta)}{\varpi(\delta)} \left\{ A_{11}(\delta) - \frac{A_{11}(1)}{A_{12}(1)} A_{12}(\delta) \right\} d\delta \tag{2.37}$$

The position of the liquid-solid interface y at time t which is deduced by the first three terms of the equation (2.30) is presented by equation (2.38) [44]:

$$t = \frac{1}{\gamma} \left\{ \frac{(y-1)^2}{2} + \frac{(y-1)^3}{(3+\gamma)} - \frac{\sigma (y-1)^4}{2(3+\gamma)^2} + \ldots \right\} \tag{2.38}$$

$$\sigma = \left\{ \frac{\gamma(\gamma^2 + 2\gamma - 3) + \zeta(\gamma^3 + 3\gamma^2 - 3\gamma + 3)}{\gamma(\gamma + 5) + \zeta(\gamma^2 + 6\gamma + 3)} \right\}, \tag{2.39}$$

where $\gamma = -\zeta A_0'(1)$. The above equations are the iterative analytical series solution of equations (2.21)-(2.25) and they can also used to estimate the initial values of finite difference solution.

In the following, the two solutions are compared in order to validate an effective numerical method, which has great potential to solve more complicated phase change problems of PCM particles.

2.4 Results analysis for inward solidification of a PCM particle

2.4.1 Analysis of dimensionless results by using both solutions

The Stefan number ζ is the only constant of the transformed equations (2.21) and (2.24). The small Stefan number means a large amount of latent

heat is being produced at the solid–liquid interface, and as a result the interface moves relatively slowly. For each different Stefan number ζ, the dimensionless times to complete solidification are calculated by using the finite difference and the iterative series solution respectively and are shown in Tables 2.1 and Table 2.2. In order to examine the temporal error and the spatial error in finite difference solution, nine groups of parameters for each different time step matching each different number of grid points are adopted, *i.e.* for $\Delta t = 0.0002/0.00002/0.000002$ and $M = 5/10/20$, assembled into 9 groups of parameters. The parameters of the nine groups guarantee stability of the FD schemes applied. The stability can be estimated by the relative errors of dimensionless temperatures of each grid points under the different time steps and a fixed number of grid points. For example, for $\zeta = 0.1$ and $M = 10$, the relative errors of dimensionless temperature of grid points for time step values of $\Delta t = 0.000002$ and $\Delta t = 0.00002$, and $\Delta t = 0.000002$ and $\Delta t = 0.0002$ at the three different solidification positions are shown in Fig. 2.2. The maximum error appears in the grid point which is closest to the liquid-solid interface while the solidification is just complete for both comparisons (one is 0.00034, another is 0.0026). However, the relative errors are small and a good numerical stability is achieved.

As shown in Tables 2.1 and 2.2, concurrence is obtained between the two solutions. In Table 2.1, for the same time step, the dimensionless time estimated by the FD solution tends to increase to an exact value as the number of grid points increases; for a fixed number of grid points, the dimensionless time also decreases or stays constant with a decrease in time step. The results indicate that the FD solution has converged. In Table 2.2,

the dimensionless times to complete solidification estimated by iterative series solution are presented under the three different terms of equation (2.38), i.e.

$$t_{1c} = \frac{1}{\gamma}\left\{\frac{(y-1)^2}{2}\right\};\ \ t_{2c} = \frac{1}{\gamma}\left\{\frac{(y-1)^2}{2} + \frac{(y-1)^3}{(3+\gamma)}\right\};$$

$$t_{3c} = \frac{1}{\gamma}\left\{\frac{(y-1)^2}{2} + \frac{(y-1)^3}{(3+\gamma)} - \frac{\sigma(y-1)^4}{2(3+\gamma)^2}\right\}. \qquad (2.40)$$

The results of t_{2c} are very close to those of t_{3c} which indicate reasonable convergence of this solution.

The principal reason for using encapsulated PCM in heat energy storage is to utilise the latent heat of a phase change, so it is preferable for PCM capsules to have a high ratio of latent heat to sensible heat. Accordingly, small values of the Stefan number of $\zeta = 0.02$ and $\zeta = 0.1$ were selected for the analysis of the results that follow.

Table 2.1: Dimensionless time to complete solidification estimated by the finite difference solution

Stefan number ζ	**Finite difference solution**								
	$\Delta t = 0.000002$			$\Delta t = 0.00002$			$\Delta t = 0.0002$		
	$M = 20$	$M = 10$	$M = 5$	$M = 20$	$M = 10$	$M = 5$	$M = 20$	$M = 10$	$M = 5$
0.01	**16.8231**	**16.8200**	**16.8079**	**16.8231**	**16.8200**	**16.8080**	**16.8234**	**16.8203**	**16.8083**
0.02	**8.4863**	**8.4832**	**8.4715**	**8.4863**	**8.4833**	**8.4715**	**8.4866**	**8.4834**	**8.4718**
0.1	**1.8068**	**1.8041**	**1.7938**	**1.8068**	**1.8041**	**1.7938**	**1.8069**	**1.8043**	**1.7939**
0.2	**0.9654**	**0.9630**	**0.9539**	**0.9654**	**0.9630**	**0.9539**	**0.9656**	**0.9632**	**0.9542**
1	**0.2747**	**0.2736**	**0.2695**	**0.2747**	**0.2737**	**0.2695**	**0.2748**	**0.2738**	**0.2696**

Table 2.2: Dimensionless time to complete solidification estimated by the iterative series solution

Stefan number ζ	Iterative series solution		
	t_{3c}	t_{2c}	t_{1c}
0.01	16.8327	16.8329	50.1664
0.02	8.4987	8.4991	25.1662
0.1	1.8272	1.8291	5.1645
0.2	0.9887	0.9921	2.6625
1	0.2970	0.3052	0.6502

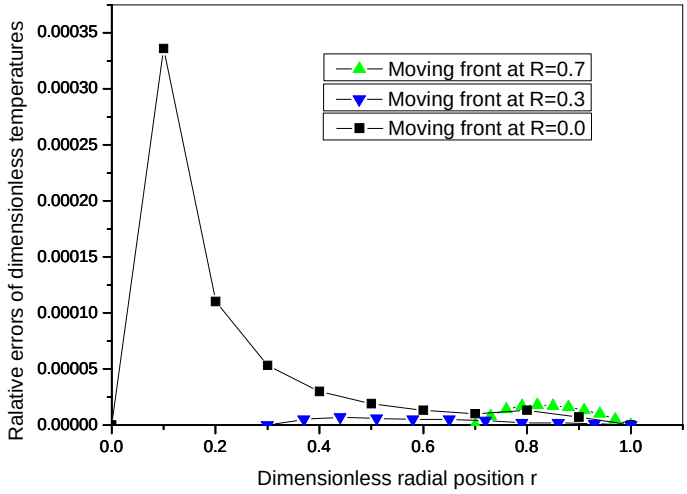

(a)

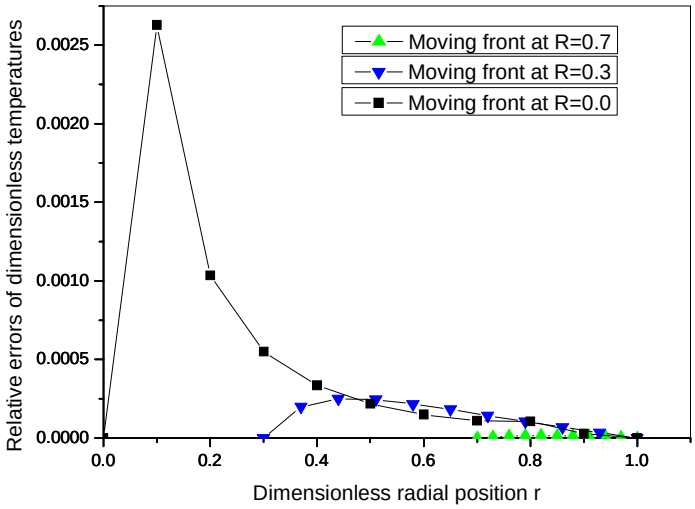

.

(b)

Figure 2.2: Relative errors of dimensionless temperatures of grid points at ζ *=0.1 and M =10 (a) Errors between* Δt *=0.000002 and* Δt *=0.00002; (b) Errors between* Δt *=0.000002 and* Δt *=0.0002.*

The evolution of the solidification front, and the related temperature distribution, were calculated by using the finite difference and the iterative series solution respectively at $\zeta = 0.02$ and $\zeta = 0.1$. The time step Δt = 0.00002 and the number of grid points M =10 for the finite difference solution were adopted for this calculation. The relationship between the dimensionless moving solidification front and the dimensionless time is shown in Fig. 2.3. It can be seen that the solidification time predicted by the finite difference method is very close to the result of the iterative series solution, and as the Stefan number ζ is reduced, the moving velocity of the liquid-solid interface is slower and the solidification takes a longer time to complete. In Fig. 2.4, the dimensionless temperature distribution in the solidified region is given at radial distances within the spherical particle for $R(t) = 0.9, 0.8, \cdots, 0.1, 0$ and with $\zeta = 0.02$. In addition, the corresponding result for $\zeta = 0.1$ is shown in Fig. 2.5. The temperature distribution is rational in each solidified stage in both solutions, although there is a small difference between them at individual grid points, especially for the larger Stefan number. The temperatures of grid points are gradually increased, along with the decrease of $R(t)$ and the corresponding increase in size of the solidified region, but until the solidification is complete, the temperatures of grid points are well controlled within the boundary range. The results reveal that both solutions are stable and reliable. When the Stefan number ζ is smaller, the temperature distribution is more extensive once solidification is complete. This can be explained by the fact that the smaller Stefan number ζ means a slower velocity of the interface, which in turn allows more time for heat diffusion behind the moving front.

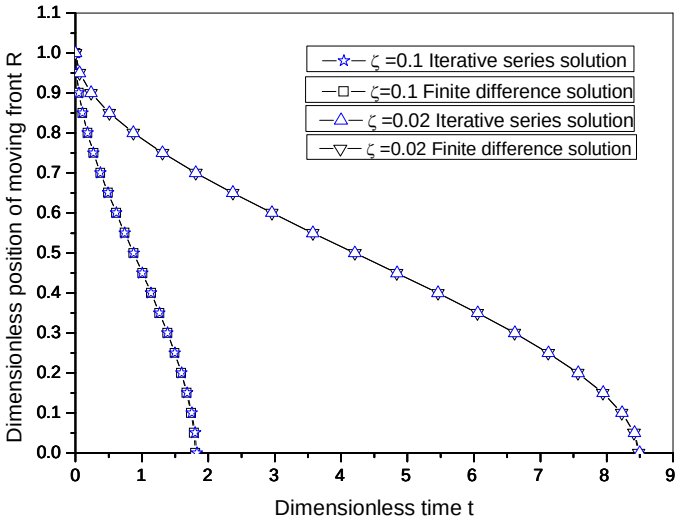

Figure 2.3: Dimensionless solidification front versus time at ζ = 0.1 and ζ = 0.02

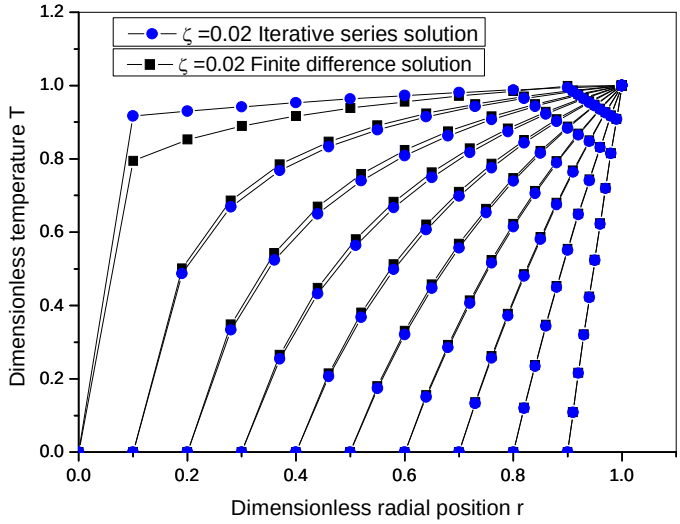

Figure 2.4: Dimensionless temperature evolution in solidified region at ζ = 0.02

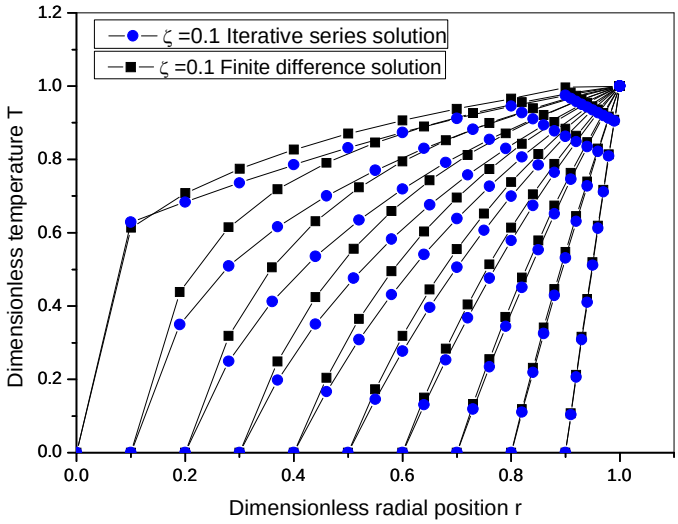

Figure 2.5: Dimensionless temperature evolution in solidified region at ζ = 0.1

2.4.2 Analysis of paraffin solidification in a single particle

For a spherical particle with encapsulated PCM, the above model can be used to estimate several variables. This includes the time required to complete solidification, the solidified volume fraction, and the temperature evolution within the solidified region at various time intervals until full solidification has occurred. It assumes that the liquid remains at the freezing temperature during the solidification stage. Paraffins are a typical group of PCMs in heat energy storage, so a single particle with core paraffin is chosen to test in the model. The thermophysical parameters of paraffin RT27 are given in Table 2.3 [91]:

Table 2.3: Thermophysical parameters of paraffin RT27

PCM	$k\left(\mathrm{W(mK)^{-1}}\right)$	$\rho\left(\mathrm{kgm^{-3}}\right)$	$c\left(\mathrm{kJ(kgK)^{-1}}\right)$	$L\left(\mathrm{kJ(kg)^{-1}}\right)$	$T_f^*\left(\mathrm{K}\right)$
paraffin	0.24	870	1.8	179	301

The four different boundary temperatures, namely $T_b^* = 300\ \mathrm{K} / 298\ \mathrm{K} / 295\ \mathrm{K} / 290\ \mathrm{K}$ (with corresponding Stefan numbers of $\zeta = 0.0101 / 0.0302 / 0.0603 / 0.1106$ respectively) were used for the calculation of a microcapsule particle with $R_{\max}^* = 30\ \mu\mathrm{m}$. Another set of boundary temperatures $T_b^* = 298\ \mathrm{K} / 296\ \mathrm{K} / 292\ \mathrm{K} / 288\ \mathrm{K}$ (the corresponding Stefan numbers being $\zeta = 0.0302 / 0.0503 / 0.0905 / 0.1307$ respectively) were used for the calculation of a microcapsule particle with $R_{\max}^* = 500\ \mu\mathrm{m}$.

The solidified front, the temperature evolution in the solidified region and the solidified volume fraction for different size particles were calculated by the FD method, as shown in Fig. 2.6–Fig. 2.11. The time step Δt = 0.00002 and the number of grid points M = 10 were used in these calculations.

In Fig. 2.6, for a $R_{\max}^* = 30\ \mu\mathrm{m}$ particle, the solidification times are 0.0982 s, 0.0333 s, 0.0171 s and 0.0096 s respectively under the four different boundary temperatures. The solidification time is reduced with the fall of the boundary temperature or the increase of the Stefan number. However, at $\zeta = 0.0101$, the solidification time is much longer than the other three cases. This implies that the further decrease of boundary temperature does not dramatically shorten the solidification time. As shown in Fig. 2.7, the temperature distributions under $T_b^* = 300\ \mathrm{K} / 290\ \mathrm{K}$ for a range of time periods are exhibited until solidification is complete. During the solidification stages,

the temperatures of grid points are well controlled between the boundary temperature and the temperature of liquid-solid interface, and gradually decrease until the solidification is complete. Under a smaller Stefan number, the temperatures of grid points keep closer to the boundary temperature as the solidified front arrives at the center due to a longer solidification time. In Fig. 2.8, the solidified volume fraction versus time is shown for the $R^*_{\max} = 30\,\mu\text{m}$ particle.

In Fig. 2.9, for the $R^*_{\max} = 500\,\mu\text{m}$ particle, the solidification times are 9.2526 s, 5.6416 s, 3.2298 s and 2.2993 s respectively under the different boundary temperatures. Under the same boundary temperature $T_b^* = 298\ \text{K}$, the solidification time of $R^*_{\max} = 500\,\mu\text{m}$ particle is much longer than the particle with $R^*_{\max} = 30\,\mu\text{m}$, as would be expected. As seen in Fig. 2.10, the temperature distribution of $R^*_{\max} = 500\,\mu\text{m}$ particle under $T_b^* = 298\ \text{K} / 288\ \text{K}$ follows the same rule as $R^*_{\max} = 30\,\mu\text{m}$.

The solidified volume fraction is given by $\eta = 1 - \left(R^* / R^*_{\max}\right)^3 = 1 - R^3$, and so its value depends on the change of dimensionless variable R . As seen from Figs. 2.8 and 2.11, the solid transformation is complete after a longer time with the decrease of Stefan number, for both the $R^*_{\max} = 30\,\mu\text{m}$ and $R^*_{\max} = 500\,\mu\text{m}$ particles. The solidification rate is higher in the initial stages, because the initial solidified region is close to the cool boundary. As the solidified front approaches the center, the rate of solidification gradually decreases due to heat transfer during continuous extension of the solid region.

In summary, the actual solidification time of particles in the form of microcapsules is proportional to the radius squared at a certain dimensionless time and thermal diffusivity (due to $t^* = R_{\max}^{*2} t/\alpha$). This is indicated by the results shown above, where the solidification time of the $R_{\max}^* = 30\,\mu\text{m}$ particle is much shorter than that for a particle with the larger radius of $R_{\max}^* = 500\,\mu\text{m}$ for the same Stefan number. The solidification time is approximately 0.1 s for $R_{\max}^* = 30\,\mu\text{m}$ and for the smallest value of the Stefan number ($\zeta = 0.0101$), although the boundary temperature of the shell is a slightly lower than the freezing temperature (the difference between the boundary temperature of the shell and the freezing temperature is just $1\ ^{\circ}\text{C}$). This result can be used as important evidence in determining the size range of microcapsule particles when they are used within a heat energy storage system, noting that PCMs are suitable for temperature stabilization and for storing heat with large energy densities in combination with rather small temperature changes [5].

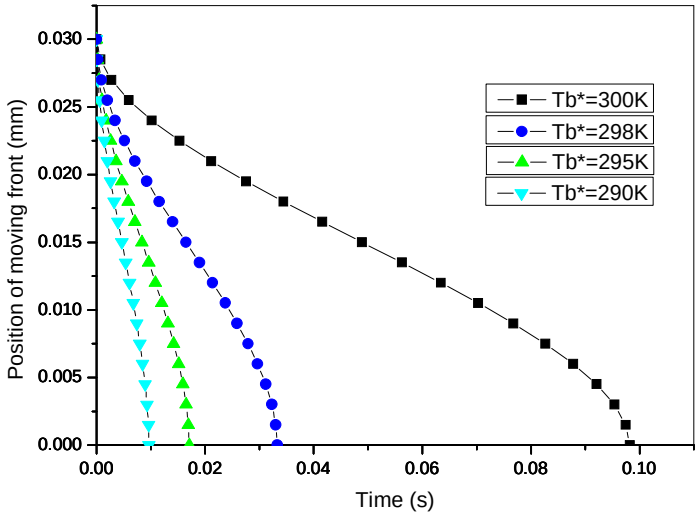

Figure 2.6: Solidification front versus time for $R_{\max}^*$ = 30 μm

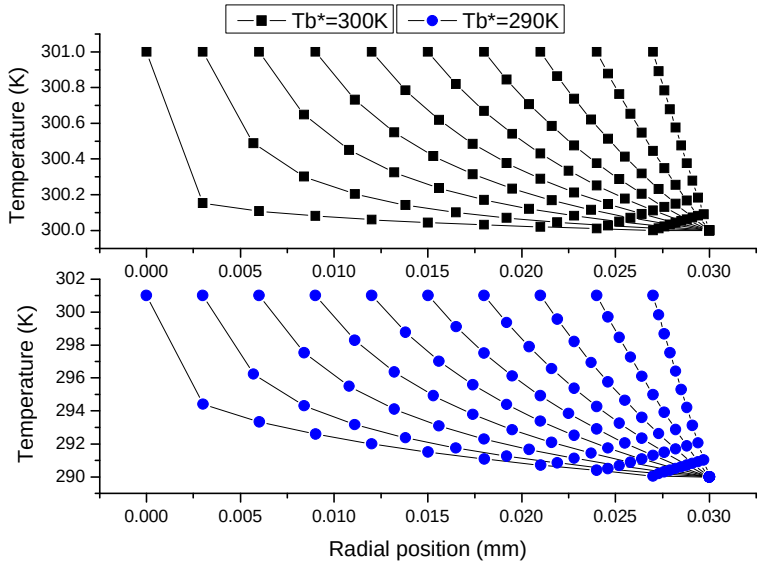

Figure 2.7: Temperature evolution within the solidified region for R^*_{max} *= 30* μm

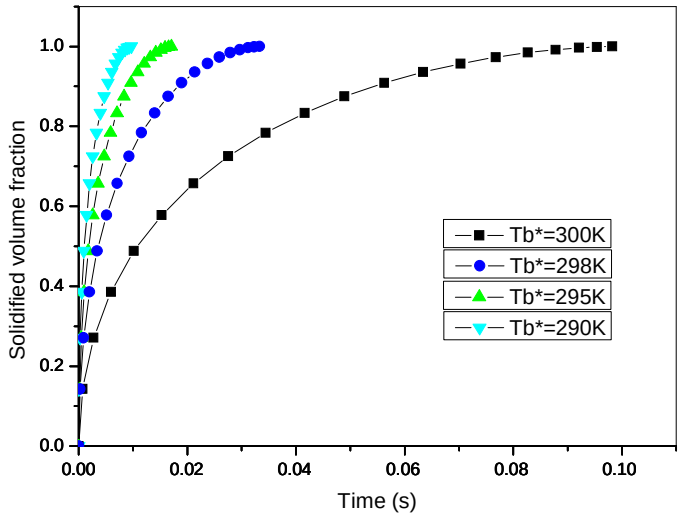

Figure 2.8: Solidified volume fraction versus time for R^*_{max} *= 30* μm

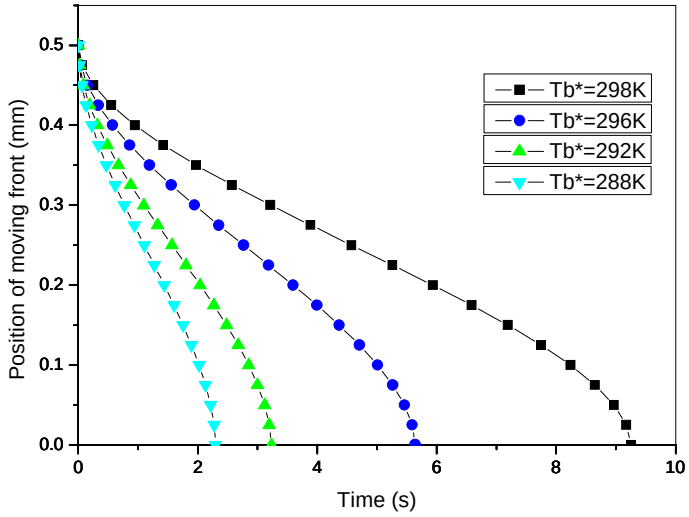

Figure 2.9: Solidification front versus time for R^*_{max} *= 500* μm

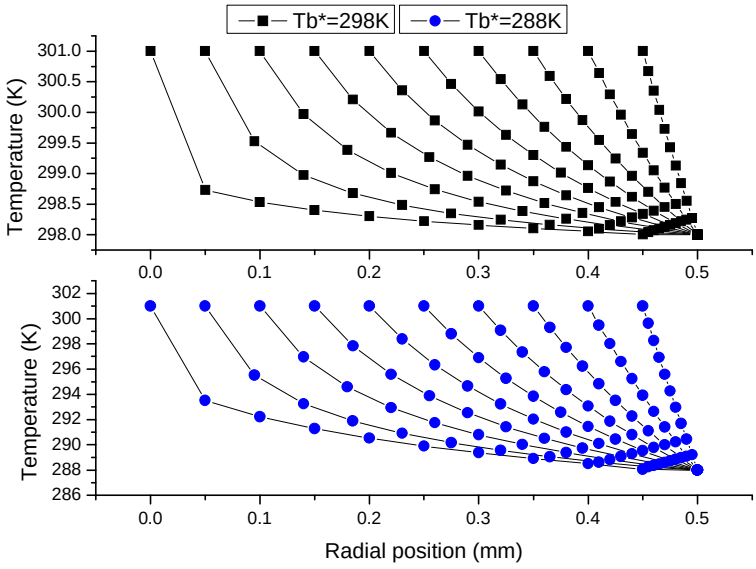

Figure 2.10: Temperature evolution within the solidified region for R^*_{max} *= 500* μm

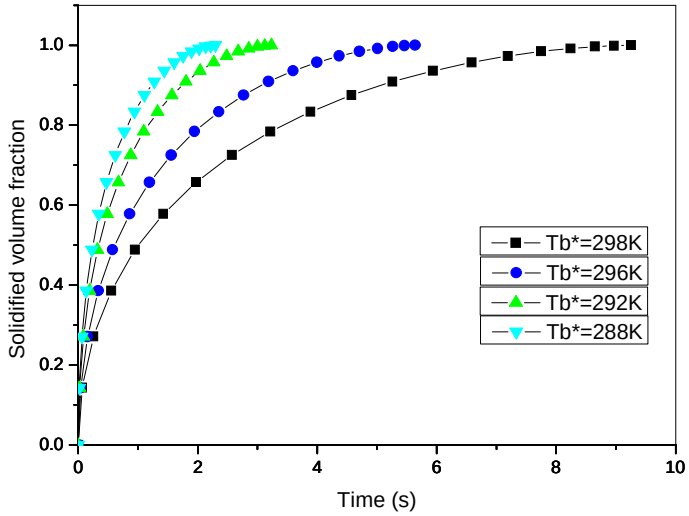

Figure 2.11: Solidified volume fraction versus time for R^*_{max} *= 500* μm

2.5 Conclusions

A spherical diffusion equation with a liquid-solid moving interface is proposed to describe the solidification of a single encapsulated PCM particle. The moving boundary problem is simplified by transformation of variables within the resulting equations. An effective finite difference scheme which takes advantages of both Explicit and Implicit Euler methods is developed, and agrees well with the iterative series solution for the inward solidification of single particles. Differently-sized particles of paraffin were tested in the model. The solidification time, temperature evolution within the solidified region, and the solidified volume fraction were calculated and analyzed. For microencapsulated PCM particles, the size effect of particles on the solidification time is noticeable, even for small Stefan numbers. In other words, in the case of high ratio of latent heat to sensible heat, the smaller microcapsules can exhibit rapid solidification under the constant temperature boundary condition.

The numerical solution described in this Chapter, which has been shown to be an effective approach for such problems, will be used as a basic method to solve more complicated physical situations, as will be described later in Chapters 3 and 6.

Chapter 3

New liquid-solid interface models for the solidification and melting of PCM particles

Summary

Two liquid-solid interface models are proposed in this chapter. For materials with a binary phase composition, a new liquid–solid interface model is proposed for encapsulated PCM particles, based on solid fraction. This is because the solid fraction acts as the bridge between the temperature at which phase change occurs and the liquid/solid two-phase composition. The new model determines a corresponding relationship between the position of the liquid-solid moving interface and the decreasing freezing temperature, and it was first used to study the solidification of a single encapsulated copper alloy particle. In addition, a new liquid-solid interface model for a single particle is explored using an initial melting point and the Gibbs-Thomson equation. This is needed for the study of PCM powder, which consists of a group of differently-sized micro/nano particles. The concept of initial melting point was proposed because the initial melting temperature at liquid-solid interface for different size micro/nano particles is different from the measured melting point of powder. The initial melting point of a single particle depends on various factors, including the minimum melting temperature of the powder, as determined by DSC tests, and the particle size. The model predicts depression of the melting point during a phase

change, caused by the surface energy of the curved interface between the solid and its own liquid.

3.1 Introduction

There is known to be a relationship between the composition of the PCM, the size of the particles and the freezing/melting temperature. In the traditional phase change model of a sphere, the temperature of the liquid-solid interface assumes a constant melting and freezing point. However, it is very common for many different materials to both melt and freeze over a range of temperatures. This change in the melting/freezing temperature directly influences the progress of phase changes.

The problem of how to build a relationship between the changing liquid-solid interface temperature and the moving liquid-solid interface is, in fact, quite challenging. The mechanisms that affect temperature changes during a phase change cycle are extremely complicated if all possible situations are considered. For these reasons, new models are proposed for the evolution of liquid-solid interface temperatures, and these are based on two specific situations:

(i) A new liquid-solid interface model for particles of metallic composites is proposed. This is because the compositions of metallic PCMs have an explicit effect on the phase change temperatures, and their relationship can be demonstrated by using alloy phase diagrams. In addition, PCMs based on metallic composites are also studied. These materials have great potential for use in solar and nuclear power plants, as they operate at a high temperature and have good thermal properties. This potential is being demonstrated by a current research

project at MIT, entitled “Metallic composites phase change materials for high temperature thermal energy storage” [94]). This involves the study of new metallic composite PCMs to support the development of utility-scale solar and next-generation nuclear energy plants. It is thus very relevant to study the phase change behaviour of these materials.

(ii) The conventional freezing and melting models for a sphere neglect the thermal characteristics of particles with a particular structure on the micro or nano scale. The surface energy of the curved interface between the solid and its own liquid is related to the changes in the volumetric Gibbs free energy, which results in modification of both the melting and freezing temperature [59, 95-96]. Moreover, for most of the commercially-available microencapsulated PCMs used for heat energy engineering, the particles size is usually distributed within a finite range, and the way in which these particles are distributed throughout a given volume will have a direct impact on the melting and freezing process. Thus, another new liquid-solid interface model for differently-sized micro/nano particles will also be addressed in this Chapter.

3.2 Modeling the effect of binary phase composition on inward solidification of a particle

3.2.1 The approach taken

As stated earlier in Chapter 2, the inward solidification of a sphere can be used as a basic model to describe the liquid-solid phase change of an

encapsulated PCM particle. In previous research related to inward solidification of a sphere [41-43, 45], the temperature of the moving liquid-solid interface was considered to be at a constant value (that of the freezing point). However, this does not consider an important physical phenomenon - namely that for a binary material with two components, for example, the solidification process occurs over a finite temperature range. This means that the relative proportions of the liquid and solid phases will change with decreasing temperature as the material starts to freeze. For example, in a simple binary phase diagram, as shown in Fig. 3.1, for a composition $M\%$ of one of the two components of the binary material, the liquid starts to freeze at a temperature of T_{f1}^{*} and is fully frozen at T_{f2}^{*}. At temperature T^{*}, the composition of L-phase (liquid) is $Lp\%$, and the composition of α-phase (solid) is $Sp\%$. The solid fraction f_s can be estimated using the Lever Rule [97], which is:

$$f_s = \frac{Lp\% - M\%}{Lp\% - Sp\%} \quad . \tag{3.1}$$

Accordingly, within the liquid-solid mixture region of the phase diagram, an increasing proportion of solid will form as the temperature decreases until solidification is complete. The temperature of the liquid-solid interface should thus reflect the continued change of the freezing temperature. The evolution of solidification for a binary alloy particle is presented diagrammatically in Fig. 3.2. The liquid and solid densities are assumed to be equal. When the solidification starts, the liquid is assumed to have a uniform temperature T_{f1}^{*}. The evolution of solidification is embodied by the moving of the liquid-solid

interface when the boundary temperature T_{bt}^* is less than T_f^*. When the liquid-solid interface R^* moves from $R_{\max}^* \to R_1^* \to R_2^* \to 0$, the equilibrium temperature of the liquid-solid interface T_f^* decreases from $T_{f1}^* \to T^* \to T'^* \to T_{f2}^*$. The composition of the L-phase at the liquid-solid interface changes along the liquidus, and the composition of the α-phase at the solid-liquid interface changes along the solidus in the phase diagram. Thus, the solid fraction f_s changes as follows:

$$f_s = 0 \to f_s = \frac{Lp\% - M\%}{Lp\% - Sp\%} = 1 - \left(\frac{R_1^*}{R_{\max}^*}\right)^3 \to f_s = \frac{Lp'\% - M\%}{Lp'\% - Sp'\%} = 1 - \left(\frac{R_2^*}{R_{\max}^*}\right)^3 \to f_s = 1$$

Here, it can be seen that a certain freezing temperature corresponds to a given solid fraction.

A new model is now proposed for the condition of a moving liquid-solid interface. Consider the case where the freezing temperature varies at a constant gradient with respect to the solid fraction (we shall denote this as 'linear'). A simple expression for this is

$$T_f^* = T_{f1}^* - \left(T_{f1}^* - T_{f2}^*\right) f_s \ . \tag{3.2}$$

A more complicated condition can be expressed as a function, as follows:

$$T_f^* = F\left(f_s\right). \tag{3.3}$$

Here, $F\left(f_s\right)$ depends on the characteristics of the materials in question, and these could be determined for example from either experimental measurements or from prior knowledge of equilibrium phase diagrams. The relationship between the binary phase composition and the liquid-solid

interface condition will be determined by Eq. (3.1) and either (3.2) or (3.3).

In this chapter, the new model is first applied to solve inward solidification of a sphere. The purpose is to quantify the effect of the binary phase composition on the liquid-solid phase change of an encapsulated PCM particle. Two copper-based materials with different compositions are chosen as case studies. The first is pure copper (Cu), with a fixed melting and freezing point, so that its liquid-solid interface maintains a constant temperature. The second is a copper-aluminium alloy (Cu-Al), for which the freezing temperature range is very wide. This allows the liquid-solid interface temperature to be studied using the fitting function of Eq. (3.3), with data based on DSC measurements. The work compares results for these two copper-based substances as they solidify, including solid fraction versus time, motion of the solidification front surface, and the temperature evolution of solidification.

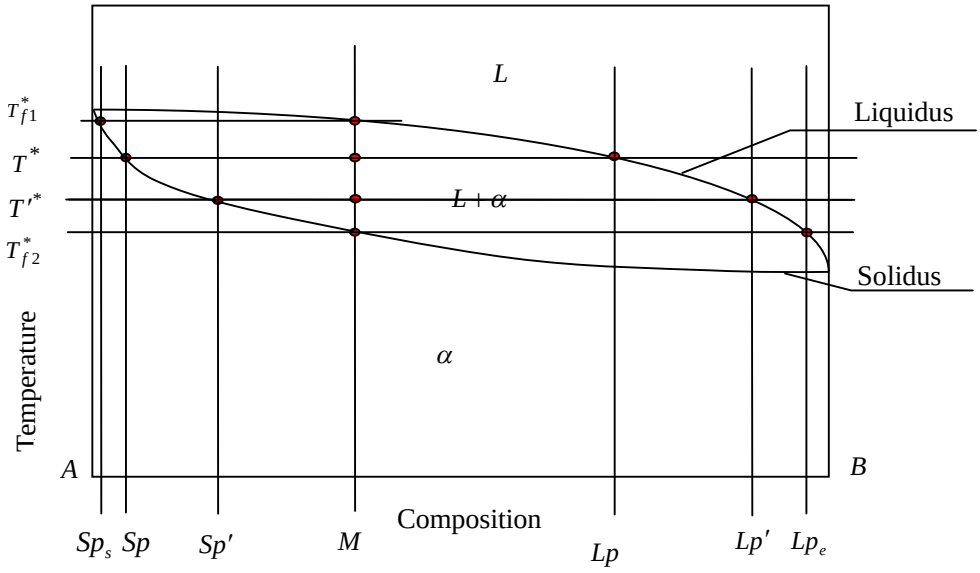

Figure 3.1: Binary phase diagram

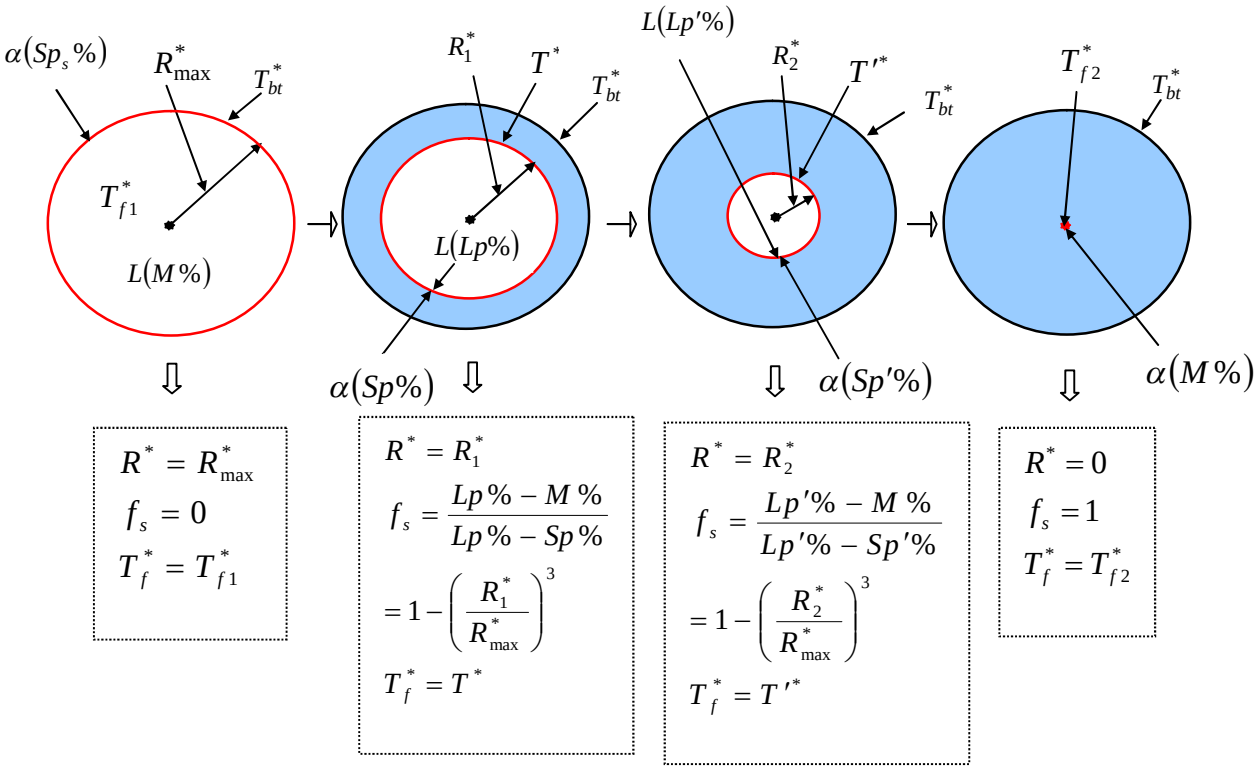

Figure 3.2: Schematic illustration of inward solidification of a binary alloy (the liquid-solid interface is shown by the red colour and the solid region by the blue colour)

3.2.2 Construction of a new liquid-solid interface model based on solid fraction

For the inward solidification of a sphere, the heat transfer equation in spherical coordinates in the solidified area can be described as:

$$\frac{\partial T^*}{\partial t^*} = \alpha\left(\frac{2}{r^*}\frac{\partial T^*}{\partial r^*} + \frac{\partial^2 T^*}{\partial r^{*2}}\right) \qquad R^* < r^* < R^*_{\max} \ , \tag{3.4}$$

where the shell boundary condition is

$$T^*_{bt} = T^*_b - \nu^* t^* \qquad at \qquad r^* = R^*_{\max} \ . \tag{3.5}$$

Here, T^*_b is initial boundary temperature, and ν^* is a cooling rate introduced

into the boundary condition. Note that if $v^* = 0$, then T_{bt}^* has a constant boundary temperature T_b^*. It is assumed that the density of the liquid is the same as that of solid in the particle. At $r^* = R^*$, T_f^* is the equilibrium temperature of the liquid-solid interface, in a very small freezing temperature range, as shown in Fig. 3.3. It is reasonable to assume that the freezing temperature and solid fraction meet the linear rule, namely

$$\frac{T_{f1}^* - T_f^*}{T_{f1}^* - T_{f2}^*} = f_s \quad \text{or} \quad T_f^* = T_{f1}^* - \left(T_{f1}^* - T_{f2}^*\right) f_s \ . \tag{3.6}$$

Meanwhile, the solid fraction satisfies the equation

$$f_s = 1 - \left(\frac{R^*}{R_{\max}^*}\right)^3 ,$$

so that

$$T_f^* = T_{f1}^* - \left(T_{f1}^* - T_{f2}^*\right)\left[1 - \left(\frac{R^*}{R_{\max}^*}\right)^3\right] . \tag{3.7}$$

When the freezing temperature range is wide, the solid fraction versus temperature can be determined from experiments. For example, the solid fraction against temperature for aluminium (Al-3004) has been measured by DSC [98] and the results are shown in Fig. 3.4. Note that the freezing temperature and solid fraction present a complicated non-linear relationship. It is difficult to obtain the analytical expression for the function $T_f^* = F\left(f_s\right)$ in this case. However, many discrete points can be obtained in experimental measurements. Between two neighbouring discrete points, it is reasonable to assume that the temperature has a linear relationship with solid fraction, and

this fact can be used for numerical calculations.

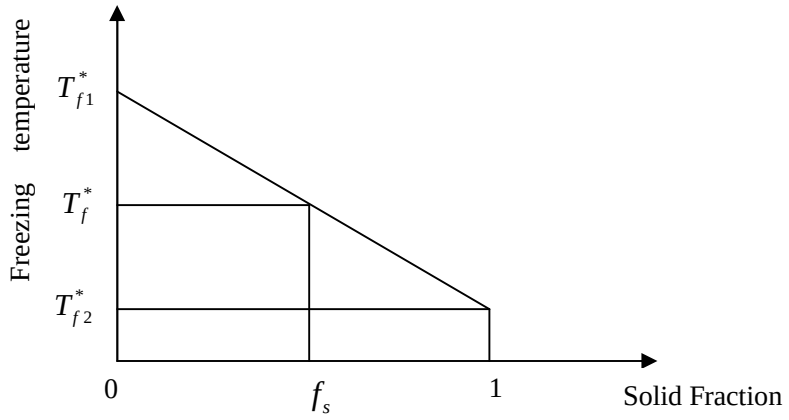

Figure 3.3: Illustration of the linear relationship between the equilibrium temperature of a liquid-solid interface and the solid fraction

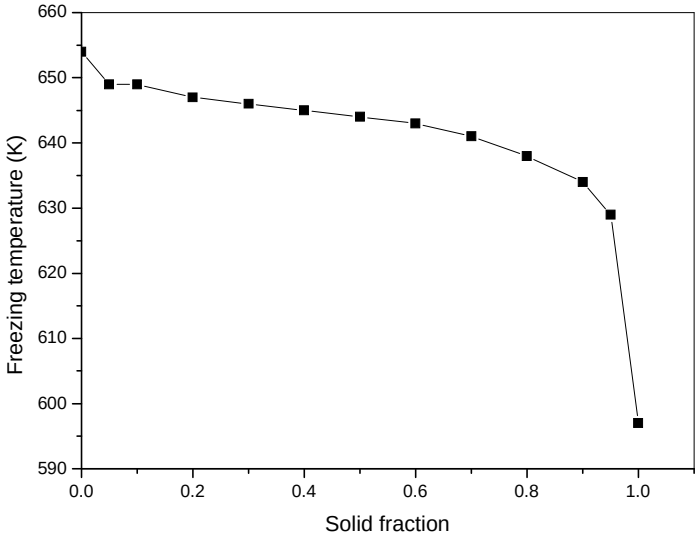

Figure 3.4: Temperature of Al-3004 within the solidification range as a function of solid fraction (f_s), at a cooling rate of 10 Kmin^{-1}

As shown in Fig. 3.5, the general temperature condition of a moving liquid-solid interface based on solid fraction can be constructed as:

$$\frac{T_k^* - T_f^*}{T_k^* - T_{k+1}^*} = \frac{f_s - f_{ks}}{f_{(k+1)s} - f_{ks}} \quad \text{or}$$

$$T_f^* = T_k^* - \frac{\left(T_k^* - T_{k+1}^*\right)\left(f_s - f_{ks}\right)}{f_{(k+1)s} - f_{ks}} = T_k^* - \frac{\left(T_k^* - T_{k+1}^*\right)}{f_{(k+1)s} - f_{ks}}\left(1 - \left(\frac{R^*}{R_{\max}^*}\right)^3 - f_{ks}\right) \quad 0 \le k < N \tag{3.8}$$

$$k = 0, T_k^* = T_{f1}^*,\ f_{ks} = 0; \quad k = N-1, T_{k+1}^* = T_{f2}^*,\ f_{(k+1)s} = 1; \quad N = 1, T_k^* = T_{f1}^*, T_{k+1}^* = T_{f2}^* \tag{3.9}$$

Here, T_k^*, T_{k+1}^*, f_{ks} and $f_{(k+1)s}$ are the known values of discrete points which can be obtained from DSC measurements or the equilibrium phase diagrams of some materials, and N is the number of discrete points used. In addition, the liquid-solid interface also meets the following criteria:

$$\rho L \frac{dR^*}{dt^*} = k \frac{\partial T^*}{\partial r^*}\Big|_{R^*}, \tag{3.10}$$

plus the initial condition:

$$R^*\big|_{t=0} = R_{\max}^*. \tag{3.11}$$

The relevant dimensionless variables are defined as:

$$T = \frac{T_{f1}^* - T^*}{T_{f1}^* - T_b^*} \quad r = \frac{r^*}{R_{\max}^*} \quad R = \frac{R^*}{R_{\max}^*} \quad t = \frac{\alpha t^*}{R_{\max}^{*2}} \quad v = \frac{v^*}{v_{\max}^*}, \tag{3.12}$$

and, as a result, the dimensionless forms of Eqs. (3.4), (3.5), (3.7), (3.8), (3.10) and (3.11) can be expressed as shown in Eqs. (3.13) - (3.18). We can initially write:

$$\frac{\partial T}{\partial t} = \frac{2}{r}\frac{\partial T}{\partial r} + \frac{\partial^2 T}{\partial r^2} \qquad R < r < 1 \tag{3.13}$$

$$T_{bt} = 1 + \frac{v_{\max}^* R_{\max}^{*2} vt}{\left(T_{f1}^* - T_b^*\right)\alpha} = 1 + \eta v t \quad at \quad r = 1, \tag{3.14}$$

where $\eta = \dfrac{v^*_{\max} R^{*2}_{\max}}{\left(T^*_{f1} - T^*_b\right)\alpha}$.

If the freezing temperature is a linear function of solid fraction during the whole solidification stage, then

$$T_f = \frac{\left(T^*_{f1} - T^*_{f2}\right)}{\left(T^*_{f1} - T^*_b\right)}\left(1 - R^3\right) = \delta\left(1 - R^3\right) \quad at \quad r = R(t), \tag{3.15}$$

where $\delta = \dfrac{\left(T^*_{f1} - T^*_{f2}\right)}{\left(T^*_{f1} - T^*_b\right)}$.

If the freezing temperature is the 'complicated function' Eq. (3.3) of solid fraction in the whole solidification stage, and satisfies local linearity, then

$$T_f = \frac{\left(T^*_{f1} - T^*_k\right)}{\left(T^*_{f1} - T^*_b\right)} + \frac{\left(T^*_k - T^*_{k+1}\right)\left(1 - R^3 - f_{ks}\right)}{\left(f_{(k+1)s} - f_{ks}\right)\left(T^*_{f1} - T^*_b\right)} = \delta_k + \delta_{kf1}\left(1 - R^3\right) - \delta_{kf2} \ , \tag{3.16}$$

where

$$\delta_k = \frac{\left(T^*_{f1} - T^*_k\right)}{\left(T^*_{f1} - T^*_b\right)} \quad \delta_{kf1} = \frac{\left(T^*_k - T^*_{k+1}\right)}{\left(f_{(k+1)s} - f_{ks}\right)\left(T^*_{f1} - T^*_b\right)} \quad \delta_{kf2} = \frac{\left(T^*_k - T^*_{k+1}\right) f_{ks}}{\left(f_{(k+1)s} - f_{ks}\right)\left(T^*_{f1} - T^*_b\right)}$$

A condition for a moving liquid-solid interface is:

$$\frac{dR}{dt} = -\zeta \left.\frac{\partial T}{\partial r}\right|_R \ , \tag{3.17}$$

where $\zeta = \dfrac{c\left(T^*_{f1} - T^*_b\right)}{L}$, $\zeta' = \dfrac{c\left(T^*_f - T^*_{bt}\right)}{L}$ is the Stefan number, and the initial condition is:

$$R\big|_{t=0} = 1. \tag{3.18}$$

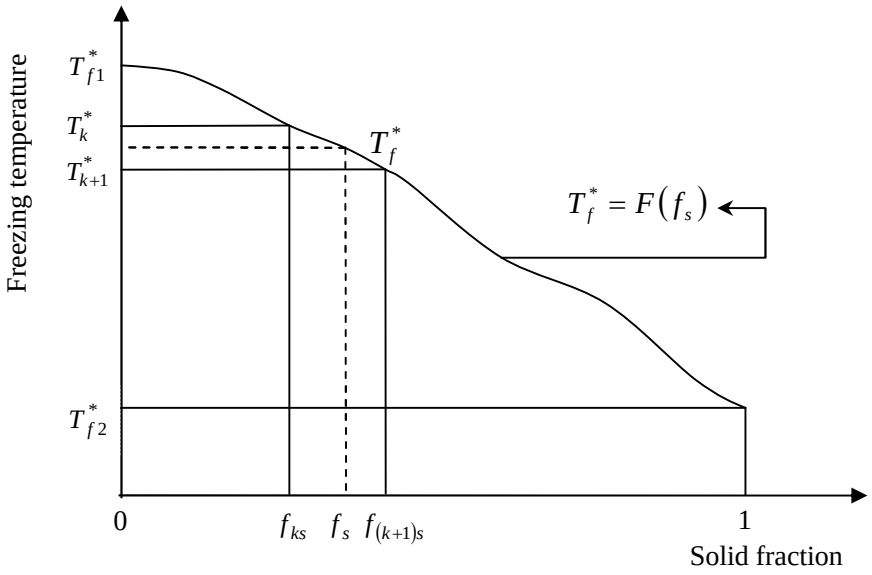

Figure 3.5: Illustration of local linear relationship between the equilibrium temperature at liquid-solid interface and the solid fraction

3.2.3 The numerical solution

A general transformation is set, so that $u(r,t) = T(r,t)r$; thus, Eqs. (3.13 - 3.17) will become the following:

$$\frac{\partial u}{\partial t} = \frac{\partial^2 u}{\partial r^2} \quad R(t) < r < 1 \tag{3.19}$$

$$at\ r = 1 \quad u(r,t) = 1 + \eta v t \tag{3.20}$$

$$at\ r = R(t)$$

$$u(r,t) = \delta\left(R - R^4\right) \tag{3.21}$$

or $$u(r,t) = \left(\delta_k + \delta_{kf1} - \delta_{kf2}\right)R - \delta_{kf1}R^4 \tag{3.22}$$

$$\frac{dR}{dt} = -\frac{\zeta}{R}\frac{\partial u}{\partial r}\Big|_R \tag{3.23}$$

The above equations involve the moving boundary problem, so the same method as Chapter 2 can be adopted. The moving boundary is reduced to a

fixed boundary by coordinate transformation, i.e. by setting the following:

$$u(r,t)=\phi(x,y)\ , \quad x=\left.(r-1)\right/[R(t)-1], \quad y=R(t)\ .$$

Eqs. (3.19) - (3.23) and (3.18) then become:

$$y\frac{\partial^2\phi}{\partial x^2}=\zeta\frac{\partial\phi}{\partial x}(1,y)\left[x\frac{\partial\phi}{\partial x}-(y-1)\frac{\partial\phi}{\partial y}\right] \tag{3.24}$$

$$at \quad x=0 \quad \phi(x,y)=1+\eta vt \tag{3.25}$$

$$at \quad x=1,$$

$$\phi(x,y)=\delta\left(y-y^4\right) \tag{3.26}$$

or $$\phi(x,y)=\left(\delta_k+\delta_{kf1}-\delta_{kf2}\right)y-\delta_{kf1}y^4 \tag{3.27}$$

$$\frac{\partial\phi}{\partial x}(1,y)=-\frac{y(y-1)}{\zeta}\frac{dy}{dt} \tag{3.28}$$

$$y\big|_{t=0}=1 \tag{3.29}$$

The solution of Eqs (3.24) - (3.29) follows the finite difference method which was developed in Chapter 2, but involving more complicated boundaries conditions which can be solved by programming.

3.2.4 Case studies using copper-based materials

In order to illustrate application of the proposed model to materials with a range of solidification temperatures, two copper-based materials have been studied. These are pure copper (Cu) and copper alloy Cu-Al (Al bronze). These are assumed to be in the form of encapsulated PCM particles. In this case study, their solidification behaviour will be studied using both the traditional model and the model developed in this thesis.

The chemical composition of Cu-Al is shown in Table 3.1, and the

thermophysical parameters of pure copper and copper alloy are presented in Table 3.2. Pure copper (Cu) has a constant freezing temperature 1357.5 K, whereas Cu-Al has a freezing temperature range of 1343 – 1297 K. The values of properties such as specific heat capacity, thermal conductivity and density are taken as those at the mean temperature over the solidification range. Table 3.3 provides the solid fraction of Cu-Al at the different freezing temperatures, obtained by HTDSC measurements.

The time-dependent solid fraction is needed within the numerical calculation to be able to apply the new liquid-solid interface model to Cu-Al alloy via. Eq. (3.27). This is obtained by locating a suitable position in Table 3.3 and finding the end points for the local linear approximations for calculating the transient temperature of the solidified front. The traditional interface condition (Eq. (2.23)) is used for the pure Cu material. A particle with $R^*_{\max}$ = 20 mm was selected for study. In the case of Cu, the initial temperature of the liquid is assumed to be the freezing temperature, whilst for Cu-Al, it is assumed to be the upper end of the freezing temperature. Two different shell boundary conditions are considered in this analysis, namely the constant boundary temperature and constant cooling rate respectively.

Table 3.1: Chemical composition of Cu-Al alloy (Wt%) [98]

Cu	Al	Fe	Ni	Mn
80.5	9.7	4.6	4.6	0.64

Table 3.2: Thermophysical properties of copper [98]

Copper	$c\left(\mathrm{kJ(kgK)^{-1}}\right)$	$L\left(\mathrm{kJ(kg)^{-1}}\right)$	$k\left(\mathrm{W(mK)^{-1}}\right)$	$\rho\left(\mathrm{kgm^{-3}}\right)$	$T_{f1}^{*}\left(\mathrm{K}\right)$	$T_{f2}^{*}\left(\mathrm{K}\right)$
Cu	0.469	208.7	330	8295	1357.5	
Cu-Al	0.569	245	42	6755	1343	1297

Table 3.3: Solid fraction of Cu-Al (Al-bronze) for cooling rate of 10 K(min)$^{-1}$ [98]

f_s	0	0.05	0.1	0.2	0.3	0.4	0.5	0.6	0.7	0.8	0.9	0.95	0.98	1.0
$T\left(^{o}C\right)$	1070	1066	1063	1058	1054	1051	1047	1044	1042	1039	1035	1033	1031	1024

3.2.4.1 Constant temperature set in shell boundary condition

In this study, the temperature of the shell boundary was supposed to be T_b^*=1295 K. The solidification time, the temperature evolution of solidified region, and the solid fraction against time were calculated for both Cu and Cu-Al, and the results are presented in Figs. 3.6-3.8. As shown in Fig. 3.6(a), the dimensionless time to complete solidification is 1.99 for Cu-Al and 1.32 for Cu. The dimensionless time to complete solidification is largely dependent on the Stefan number. The small Stefan number implies that a large amount of latent heat is being produced at the solid–liquid interface and small temperature gradient exists in the solid region; as a result the interface proceeds relatively slowly. The Stefan number of Cu is $\zeta = 0.1405$. The initial Stefan number of Cu-Al is $\zeta = 0.1115$. For Cu-Al, the temperature of the liquid-solid interface changes with the solid fraction, so the Stefan number of Cu-Al varies continuously, reaching a value of $\zeta = 0.0046$ as the solidification process completes. Cu-Al has a small Stefan number compared with Cu for the whole solidification process, and hence has a longer dimensionless time to become fully solid. The solidification time of Cu is short due to the larger thermal conductivity (Fig. 3.6 (b)).

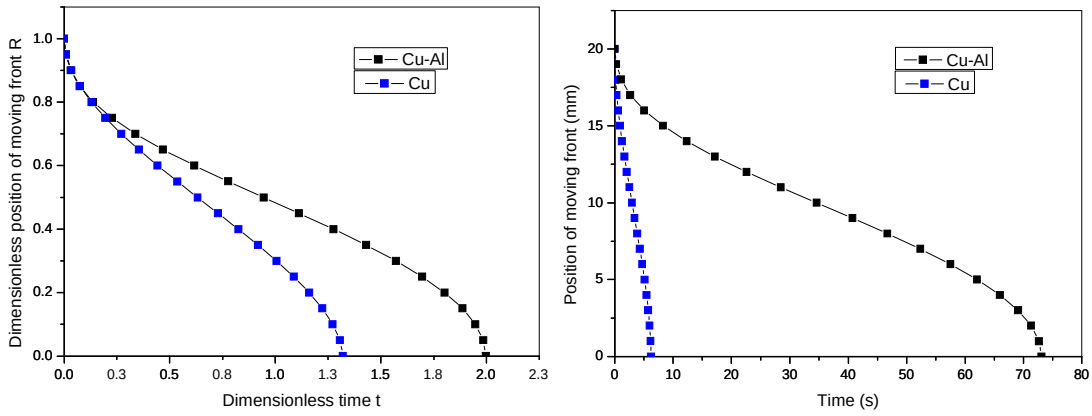

(a) (b)

Figure 3.6: Solidification front position versus time for a constant boundary temperature.

In Fig.3.7(a), the dimensionless temperature distribution in the solidified region is given at radial distances within the spherical particle for $R(t) = 0.8, 0.6, 0.4, 0.2, 0$. For the two cases, the dimensionless temperatures both gradually increase along with the decrease of $R(t)$ (contrary to the real temperature distribution owing to the definition of the dimensionless temperature). Cu has a constant temperature at the liquid-solid interface, so the temperature distribution at every stage stays within the 0-1 range. For Cu-Al, since the temperature of the liquid-solid interface changes with the solid fraction, the dimensionless temperature of the liquid-solid interface gradually increases from 0, but it cannot reach a value of 1 because the temperature of the boundary shell is lower than the lowest temperature of the liquid-solid interface. The actual temperature distributions are presented in Fig.3.7(b). Note that the actual temperatures gradually decrease along with an increase in the relative volume of the solidified region. The temperatures of pure Cu are distributed between 1295 K and 1357.5 K, and the temperature of liquid-solid interface of Cu-Al decreases from 1320.5 K (for

$R(t) = 0.8$) to 1297 K (at $R(t) = 0$).

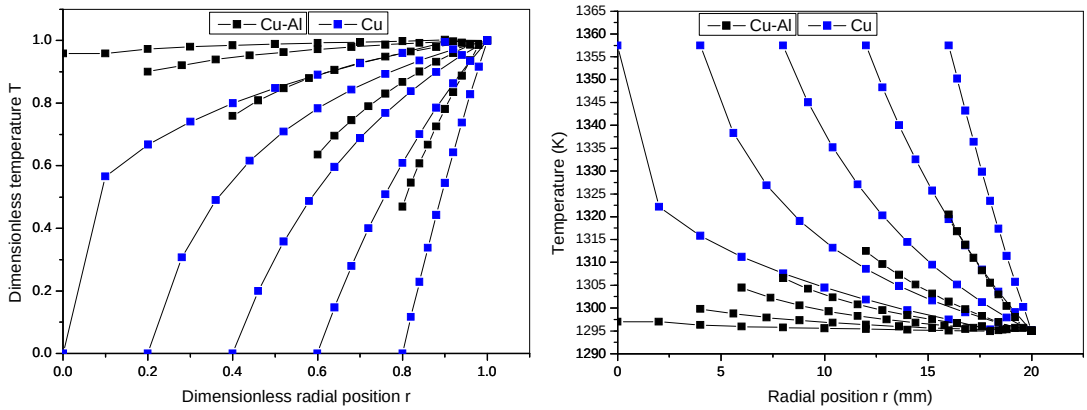

(a) (b)

Figure 3.7: Temperature evolution in solidified region under constant boundary temperature. (a) dimensionless temperature distributions at dimensionless time t= 0.13, 0.44, 0.83,1.16, 1.32 for Cu and t= 0.14, 0.62, 1.28, 1.80, 1.99 for Cu-Al, (b) temperature distributions at time t^*= 0.61s, 2.09s, 3.89s, 5.47s, 6.22s for Cu and t^*= 5.06s, 22.59s, 46.72s, 65.98s, 73.11s for Cu-Al

The evolution of solidification is presented in Fig. 3.8 for both materials. The solidification rate is higher for both of them at the initial stages of solidification, for example, the dimensionless time to complete 50% solidification is around 0.15 for Cu-Al (7.5% of the total solidification time) and 0.14 (10.6% of the total solidification time) for Cu. The subsequent solidification rate decreases significantly because of the slow heat conduction in the continuously thickening solid region.

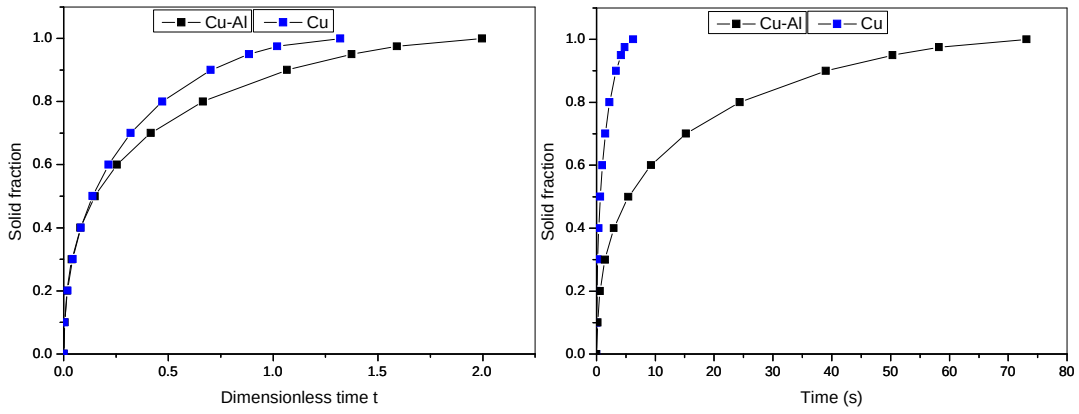

(a) (b)

Figure 3.8: Solid fraction versus time under constant boundary temperature

3.2.4.2 Results for a shell boundary condition with a constant cooling rate

The initial shell boundary temperature is assumed to be T_b^* = 1320 K, which is the middle value for the freezing temperature range of Cu-Al. The cooling rate is assumed to be $\nu^* = 100\ \mathrm{K}(\mathrm{min})^{-1}$. As seen in Fig. 3.9, the dimensionless time to complete solidification is 1.82 for Cu and 1.43 for Cu-Al (the corresponding actual time to complete solidification is 8.57 s for Cu and 52.34 s for Cu-Al), respectively. The initial Stefan number of Cu is $\zeta = 0.084$ while the initial Stefan number of Cu-Al is $\zeta = 0.053$. When the solidification is complete, the boundary temperature of Cu is $1320 - 8.57\nu^* = 1306\,(\mathrm{K})$ and $1320 - 52.34\nu^* = 1233\,(\mathrm{K})$ for Cu-Al. The Stefan number of Cu increases to $\zeta = 0.116$ and the one of Cu-Al increases to $\zeta = 0.149$. The larger increase in the Stefan number for the Cu-Al alloy results in the quicker movement of the liquid-solid interface, and hence less dimensionless time to finish the solidification. However, the actual

solidification time of Cu is much shorter than Cu-Al due to its larger thermal conductivity.

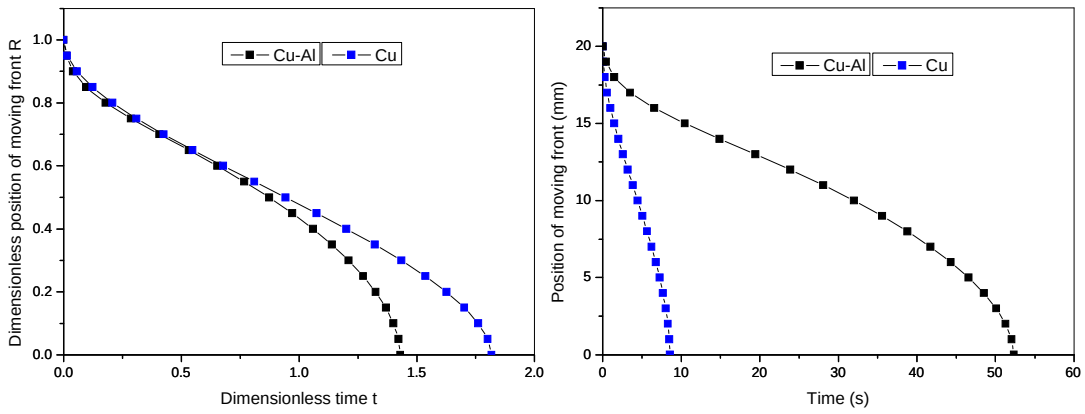

(a) (b)

Figure 3.9: Solidification front position versus time for a constant cooling rate

In Fig. 3.10 (a), it can be seen that the dimensionless temperature of the shell boundary gradually increases for both materials, due to the effect of cooling rates. For Cu-Al, the dimensionless temperature of the liquid-solid interface steadily increases with an increase in solid fraction. Since the initial temperature of the boundary shell is in the middle of the freezing range, the dimensionless temperature of the liquid-solid interface may be greater than unity according to the definition of the dimensionless temperature. For the same reason, the dimensionless temperature of the shell boundary may also be greater than unity. Predicted radial temperature distributions are presented in Fig. 3.10(b) for different stages of the solidification process. For Cu, the actual temperature of liquid-solid interface remains constant at 1357.5 K and the actual temperature of shell boundary varies from 1318.4 K (at a value of $R(t) = 0.8$) to 1306 K (at $R(t) = 0$), due to the influence of the

cooling rate. The actual temperature of the liquid-solid interface gradually decreases to 1297 K for Cu-Al, which exhibits the solidification behaviour of a binary alloy particle. The boundary shell temperature of Cu-Al varies from 1309 K ($R(t)=0.8$) to 1233 K ($R(t)=0$).

Note that, except at the very initial stages of solidification, the solidification rate of Cu-Al in dimensionless time is slightly above that of Cu (shown in Fig. 3.11), as the Stefan number of Cu-Al increases more for a longer actual solidification time. Nevertheless, the solidification rate of Cu-Al in actual (dimensional) time is much lower than Cu, due to the much smaller thermal conductivity (around one eighth of the value for Cu). The above analysis reveals that the dimensionless time to complete solidification relies mainly on the Stefan number, although the actual solidification time depends on the thermal properties of each of the materials.

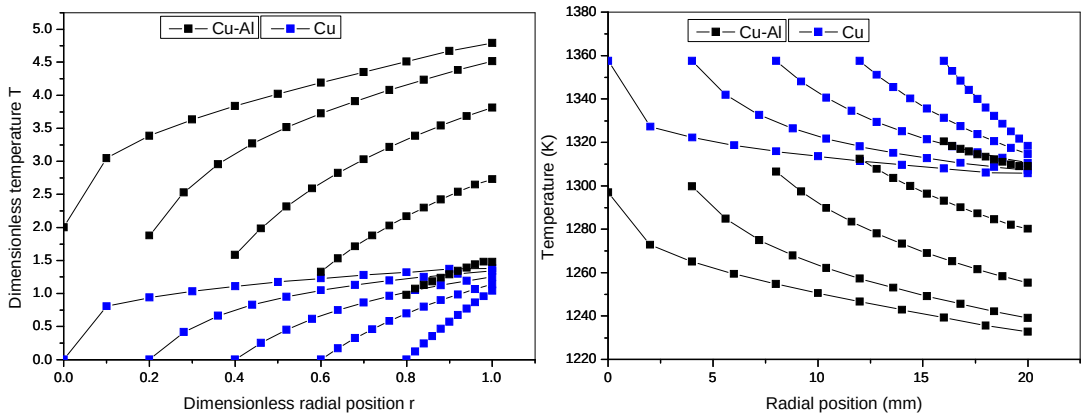

(a) (b)

Figure 3.10: Temperature evolution in solidified region under constant cooling rate condition. (a) dimensionless temperature distributions at dimensionless time t= 0.21, 0.68, 1.20, 1.63, 1.82 for Cu and t= 0.18, 0.65, 1.06, 1.33, 1.43 for Cu-Al, (b) temperature distributions at time t= 0.97s, 3.19s, 5.66s, 7.66s, 8.57s for Cu and t= 6.57s, 23.89s, 38.80s, 48.52s, 52.34s for Cu-Al.

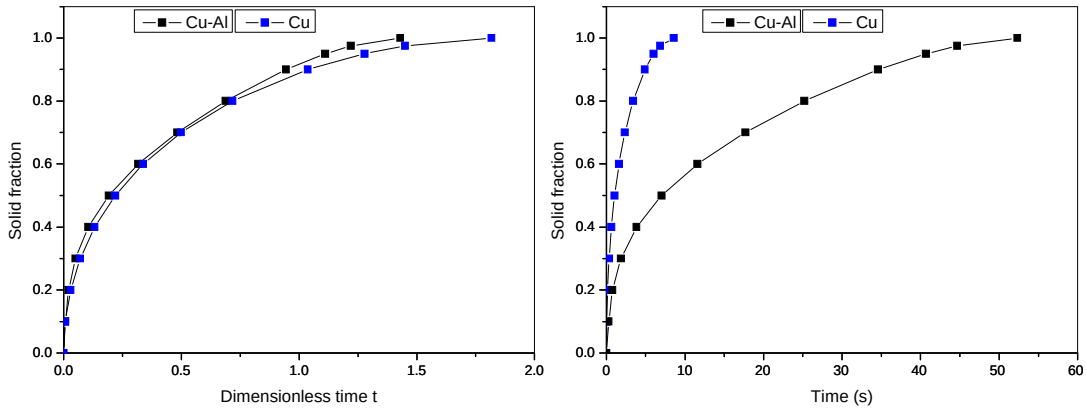

(a) (b)

Figure 3.11: Solid fraction versus time under constant cooling rate condition

3.3 Melting model of differently-sized micro/nano particles

3.3.1 Background

The above solidification model of a PCM particle is built based on single-phase region. This is because the liquid-solid interface moves slowly relative to the speed at which heat conducts in the solid phase for small Stefan numbers. In addition, the temperature within the inner liquid phase decays very quickly to the fusion temperature, so the liquid phase does not affect the solidification process and can be essentially ignored [92]. However, when the reverse melting process of a particle is considered, an interesting phenomenon is found, and has been observed in the melting experiments of nanoparticles which were reported by Kofman et al. [99]. They found that once the temperature of the particle reached a certain value, the remaining solid core melted abruptly. Furthermore, Mccue and Hill [59] were motivated to develop a full two-phase melting model including the effects of surface tension. The model leads to superheating in the solid phase and their

numerical computations suggest that the solution will cease to exist when the particle radius reaches some critical value and superheating has occurred.

In the later Chapters, we will study the melting heat transfer of novel slurries of particulate PCMs. The materials to be studied consist of microencapsulated PCM particles of different sizes. DSC measurements indicate that these particles have a melting temperature range. There is thus a need to develop models further, to account for some of the phenomena mentioned above, and to more fully explain the experimental results to be reported later in the thesis. Thus, here we will build a full two-phase melting model of differently-sized micro/nano particles based on the above analysis. This is important, because the study of particles of finite size within slurries is an example of a fundamental bridge of understanding between the molecular scale and its relationship to the bulk scale [95].

3.3.2 Size effect on the melting point of micro/nano particles

Crystalline melting, solid-solid and superfluid [100] phase transitions have been observed to shift to lower temperatures for materials confined to small pores [95]. In the limitation of crystal size it is well known that surface tension acts to decrease the melting temperature of a solid particle as the radius of the particle decreases [95-96]. This phenomenon has been observed in metal particles [101-102], finely dispersed nonporous powders [103], polymer lamelle of different thicknesses [104] and organic materials [95]. The formation of small crystals is described theoretically in a classical discussion by Gibbs and a related theory [95]. The Gibbs-Thomson equation predicts the melting point depression ΔT_m for a small crystal of radius R^* as being given by [96]:

$$\Delta T_m = T_m^* - T_{mR}^*\left(R^*\right) = 2\sigma_{sl}T_m^* / \left(R^*\rho_s L\right), \quad (3.30)$$

where σ_{sl} is the surface energy of the solid-liquid interface, T_m^* is bulk melting point, $T_{mR}^*\left(R^*\right)$ is the melting point of a crystal of radius R^*, ρ_s is solid density and L is the bulk enthalpy of fusion.

However, commercial available MPCM generally contains particles with a limited size range. For example, BASF is one of the manufacturers of micro-encapsulated paraffin. The shell of their capsules consists of PMMA and is less than 200 nm thick [22]. As shown in Fig.3.12, the particle size distribution (PSD) in a volume of BASF DS 5008 microcapsules shows distributions of particle diameters ranging from 1 to 20 μm, with the distributed peak at about 7 μm [105]. In addition, the melting and freezing temperature of DS 5008 particles were measured by DSC and exhibits a melting and freezing temperature range and a sub-cooling phenomenon, as shown in Fig. 3.13. Note also that bulk Paraffin wax itself has a phase change temperature range, generally with a peak value. As shown in Fig. 3.14, DSC curves of a paraffin wax were measured by Liu and Chung [106]. The paraffin wax has an obvious melting (freezing) temperature range and a slight sub-cooling. According to ICTAC standards, the onset of the melt peak is suggest as the melting point for metals, organics, and similar materials, but the peak value should be used for polymers [107]. Compared with Fig. 3.13, although the main core material of microcapsule DS 5008 is also kind of paraffin, the microcapsules exhibit a significant sub-cooling effect, perhaps due to the influence of variable particle sizes or impurities. Thus it is difficult

to determine the melting point of an individual particle, because the DSC result only embodies the effect of the whole powder.

Note that, if the accurate composition of the paraffin within a particular microcapsule is known, the bulk melting point can be obtained, and the melting point of differently sized micro/nano particles can be further determined from Gibbs-Thomson equation. This is also true for mixtures. For example, in works of He et al. [108-109], *n*-paraffin waxes with a phase transition temperature suitable for comfort cooling had been defined as hexadecane, tetradecane and their mixtures. Although hexadecane and tetradecane were thought to have a melting point based on the general DSC measurement rule, the mixture of them was considered as a binary diagram system, and melting temperature of the mixture should be in a range which is limited by liquidus and solidus. The binary diagram of hexadecane and tetradecane were constituted by DSC measurements. From this point, the binary phase solidification model in Section 3.2 can also be used for the organic mixture materials. However, for a group of micro/nano particles, the difficulty is how to determine the melting temperature of liquid-solid interface of a single particle. If considering the usual melting point (the peak value or onset of the melt peak) as the temperature of the liquid-solid interface, there is a problem, *i.e*. in the general melting model of a sphere, the solid does not melt while the shell boundary temperature approaches the melting temperature range but remains lower than the melting point. Accordingly, the minimum temperature of the melting temperature range is a suitable value to determine the temperature of liquid-solid interface, because the solid starts to melt, provided that the boundary temperature is bigger than this

temperature. In view of the effect of particle size, the concept of initial melting point for liquid-solid interface is introduced. Each micro/nano particle has an initial melting point. It is reasonable that the minimum melting temperature of micro/nano PCM powder is assumed to be the initial melting point of the smallest particle. The initial melting point of other particles should be based on the minimum melting temperature of micro/nano PCM powder and the size of an individual particle, and derived from the Gibbs-Thomson equation, expressed as:

$$T_{mR}^{*}\left(R_{\max}^{*}\right)=T_{m,\min}^{*}\frac{\left(1-2\sigma_{sl}/\left(R_{\max}^{*}\rho_{s}L\right)\right)}{\left(1-2\sigma_{sl}/\left(R_{\max,\min}^{*}\rho_{s}L\right)\right)}=T_{m,\min}^{*}\frac{\left(1-\lambda/R_{\max}^{*}\right)}{\left(1-\lambda/R_{\max,\min}^{*}\right)}=T_{mc}^{*}\left(1-\lambda/R_{\max}^{*}\right)$$

$$\lambda=2\sigma_{sl}/\left(\rho_{s}L\right),\ T_{mc}^{*}=\frac{T_{m,\min}^{*}}{\left(1-\lambda/R_{\max,\min}^{*}\right)} \qquad (3.31)$$

Here, $R_{\max}^{*}$ is the radius of a particle, $R_{\max,\min}^{*}$ is the radius of the smallest particle, $T_{m,\min}^{*}$ is the minimum melting temperature of micro/nano PCM powder and T_{mc}^{*} is the supposed bulk melting point.

After the initial melting points of differently-sized particles have been determined, in the next section, we will address the melting model of liquid-solid two phase for a single PCM particle.

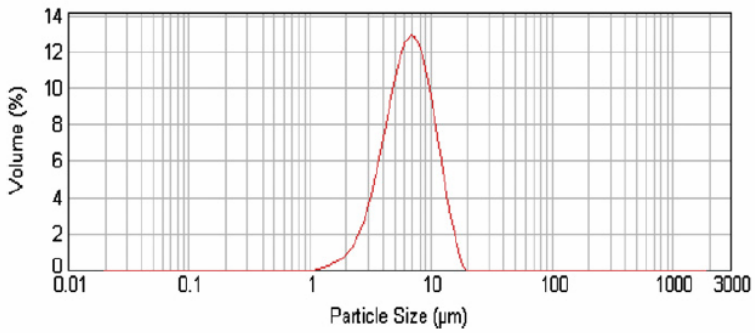

Figure 3.12: Particle size distributions of BASF DS 5008 microcapsules [105]

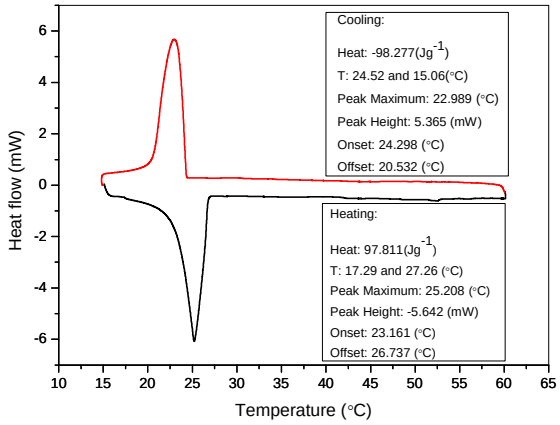

Figure 3.13: DSC heat flow curve of BASF DS 5008 microcapsules

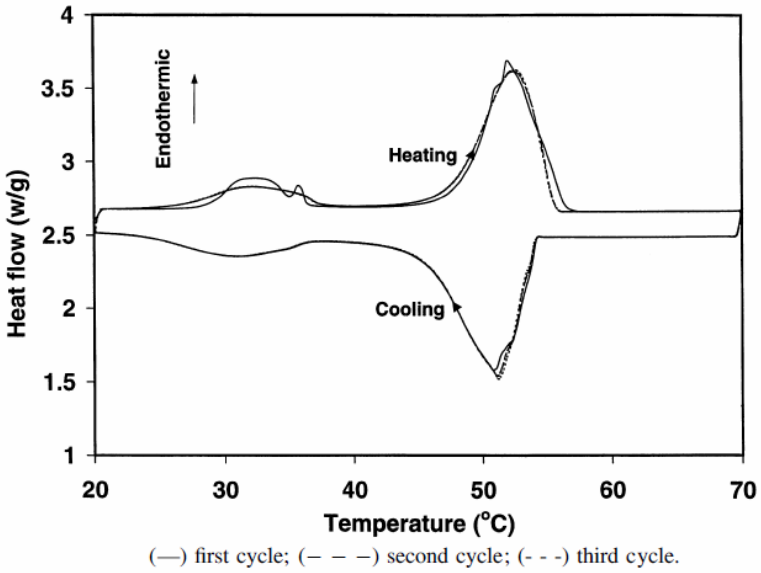

Figure 3.14: DSC curves of paraffin wax [106]

3.3.3 Governing equations of liquid-solid two-phase of a sphere (a single particle)

The heat transfer equations in the liquid and solid area of a sphere are described respectively by:

$$\frac{\partial T_l^*}{\partial t^*} = \alpha_l \left(\frac{2}{r^*} \frac{\partial T_l^*}{\partial r^*} + \frac{\partial^2 T_l^*}{\partial r^{*2}} \right) \qquad R^* < r^* < R^*_{\max} \tag{3.32}$$

$$\frac{\partial T_s^*}{\partial t^*} = \alpha_s \left(\frac{2}{r^*} \frac{\partial T_s^*}{\partial r^*} + \frac{\partial^2 T_s^*}{\partial r^{*2}} \right) \qquad 0 < r^* < R^* \tag{3.33}$$

The centre of the sphere meets the adiabatic boundary condition:

$$\frac{\partial T_s^*}{\partial r^*} = 0 \quad at \quad r^* = 0 \tag{3.34}$$

The equilibrium temperature at the liquid-solid interface is expressed according to the Gibbs-Thomson equation:

$$T_l^* = T_s^* = T_{mR}^* \left(R^* \right) = T_{mc}^* \left(1 - \lambda / R^* \right) \qquad at \quad r^* = R^*, \tag{3.35}$$

where it is assumed that the density of liquid is as the same as that of solid in the particle, so that the heat flow balance equation at the liquid-solid interface is described as:

$$\left(k_l \frac{\partial T_l^*}{\partial r^*} - k_s \frac{\partial T_s^*}{\partial r^*} \right) \Bigg|_{R^*} = -\rho L \frac{dR^*}{dt^*} \ , \tag{3.36}$$

and where the initial condition is:

$$R^* \big|_{t=0} = R_{\max}^* \qquad T_s^* \big|_{t=0} = T_i^* \ . \tag{3.37}$$

Note the shell boundary temperature T_{bt}^* changes with time and the initial temperature is set as T_b^*, so that:

$$T_{bt}^* \big|_{t=0} = T_b^* \qquad at \qquad r^* = R_{\max}^* \tag{3.38}$$

3.3.4 Methods for liquid-solid two-phase solution

The relevant dimensionless variables are defined as:

$$T_l = \frac{T_l^* - T_{mR}^* \left(R_{\max}^* \right)}{T_b^* - T_{mR}^* \left(R_{\max}^* \right)} \quad T_s = \frac{T_s^* - T_{mR}^* \left(R_{\max}^* \right)}{T_b^* - T_{mR}^* \left(R_{\max}^* \right)} \quad r = \frac{r^*}{R_{\max}^*} \quad R = \frac{R^*}{R_{\max}^*} \quad t = \frac{\alpha_l t^*}{R_{\max}^{*2}}, \tag{3.39}$$

and the dimensionless forms of Eqs. (3.32-3.38) are then constructed as follows:

$$\frac{\partial T_l}{\partial t} = \frac{2}{r}\frac{\partial T_l}{\partial r} + \frac{\partial^2 T_l}{\partial r^2} \qquad R(t) < r < 1 \tag{3.40}$$

$$\frac{\partial T_s}{\partial t} = \alpha_r\left(\frac{2}{r}\frac{\partial T_s}{\partial r} + \frac{\partial^2 T_s}{\partial r^2}\right) \quad 0 < r < R(t) \tag{3.41}$$

$$\frac{\partial T_s}{\partial r} = 0 \quad at \quad r = 0 \tag{3.42}$$

$$T_l = T_s = T_{mR}(R) = \theta\left(1 - \frac{1}{R}\right) \quad at \quad r = R(t) \tag{3.43}$$

$$\left(\frac{\partial T_l}{\partial r} - k_r \frac{\partial T_s}{\partial r}\right)\Big|_R = -\frac{1}{\zeta''}\frac{dR}{dt} \tag{3.44}$$

$$R\big|_{t=0} = 1 \quad T_s\big|_{t=0} = \upsilon \tag{3.45}$$

$$T_{bt} = \psi \text{ , } T_{bt}\big|_{t=0} = 1 \quad at \quad r = 1 \tag{3.46}$$

Here, some of the dimensionless parameters are defined by:

$$\alpha_r = \frac{\alpha_s}{\alpha_l}; \quad \theta = \frac{T_{mc}^* \lambda}{R_{\max}^*\left(T_b^* - T_{mR}^*\left(R_{\max}^*\right)\right)}; \quad \zeta'' = \frac{c_l\left(T_b^* - T_{mR}^*\left(R_{\max}^*\right)\right)}{L}; \quad k_r = \frac{k_s}{k_l};$$

$$\upsilon = \frac{T_i^* - T_{mR}^*\left(R_{\max}^*\right)}{T_b^* - T_{mR}^*\left(R_{\max}^*\right)}; \; \psi = \frac{T_{bt}^* - T_{mR}^*\left(R_{\max}^*\right)}{T_b^* - T_{mR}^*\left(R_{\max}^*\right)}; \; T_{mR}^*\left(R_{\max}^*\right) = T_{mc}^*\left(1 - \lambda / R_{\max}^*\right).$$

By the transformation $u_l(r,t) = T_l(r,t)r$ and $u_s(r,t) = T_s(r,t)r$, Eqs. (3.40) - (3.46) can be further simplified and changed into:

$$\frac{\partial u_l}{\partial t} = \frac{\partial^2 u_l}{\partial r^2} \quad R(t) < r < 1 \tag{3.47}$$

$$\frac{\partial u_s}{\partial t} = \alpha_r \frac{\partial^2 u_s}{\partial r^2} \quad 0 < r < R(t) \tag{3.48}$$

$$u_s = 0 \quad at \quad r = 0 \tag{3.49}$$

$$u_l = u_s = u_{mR}(R) = \theta(R-1) \quad at \quad r = R(t) \tag{3.50}$$

$$\frac{dR}{dt} = -\frac{\zeta''}{R}\left[\left(\frac{\partial u_l}{\partial r} - k_r \frac{\partial u_s}{\partial r}\right)\Big|_R - \frac{(1-k_r)u_{mR}(R)}{R}\right] \tag{3.51}$$

$$R\big|_{t=0} = 1 \quad u_s\big|_{t=0} = \upsilon r \tag{3.52}$$

$$u_{bt} = \psi \quad u_{bt}\big|_{t=0} = 1 \quad at \quad r = 1 \tag{3.53}$$

For a liquid-solid two-phase region, the middle liquid-solid interface is a moving boundary. In order to obtain the fixed computational domain, a coordinate transformation is used in liquid and solid, respectively, as follows. Let $u_l(r,t) = \phi_l(x_l, y)$ and $u_s(r,t) = \phi_s(x_s, y)$; also note that other variables are defined as:

$x_l = (r-1)\big/[R(t)-1]$, $\quad y = R(t)$ and $x_s = \dfrac{r}{R(t)}$.

For example, due to the fact that:

$$\frac{\partial u_s}{\partial t} = \frac{\partial \phi_s}{\partial x_s}\frac{\partial x_s}{\partial t} + \frac{\partial \phi_s}{\partial y}\frac{\partial y}{\partial t} = -\frac{\partial \phi_s}{\partial x_s}\frac{x_s R'(t)}{R(t)} + \frac{\partial \phi_s}{\partial y}R'(t)$$

$$\frac{\partial u_s}{\partial r} = \frac{\partial \phi_s}{\partial x_s}\frac{\partial x_s}{\partial r} + \frac{\partial \phi_s}{\partial y}\frac{\partial y}{\partial r} = \frac{\partial \phi_s}{\partial x_s}\frac{1}{R(t)}$$

$$\frac{\partial^2 u_s}{\partial r^2} = \frac{\partial}{\partial x_s}\left(\frac{\partial u_s}{\partial r}\right)\frac{\partial x_s}{\partial r} + \frac{\partial}{\partial y}\left(\frac{\partial u_s}{\partial r}\right)\frac{\partial y}{\partial r} = \frac{\partial^2 \phi_s}{\partial {x_s}^2}\frac{1}{R(t)^2}$$

Eq. (3.48) becomes:

$$\frac{\partial^2 \phi_s}{\partial {x_s}^2} = \frac{yy'}{\alpha_r}\left[\frac{\partial \phi_s}{\partial y}y - \frac{\partial \phi_s}{\partial x_s}x_s\right] \qquad 0 < x_s < 1 \tag{3.54}$$

In the same way, Eq. (3.47) changes into:

$$\frac{\partial^2 \phi_l}{\partial {x_l}^2} = (y-1)y'\left[\frac{\partial \phi_l}{\partial y}(y-1) - \frac{\partial \phi_l}{\partial x_l}x_l\right], \qquad 0 < x_l < 1 \tag{3.55}$$

and Eqs. (3.49) - (3.53) become:

$$\phi_s = 0 \quad at \quad x_s = 0 \tag{3.56}$$

$$\phi_l = \phi_s = \phi_{mR}(y) = \theta(y-1) \quad at \quad x_l = x_s = 1 \tag{3.57}$$

$$y' = -\frac{\zeta''}{y}\left[\frac{1}{(y-1)}\frac{\partial \phi_l}{\partial x_l}(1,y) - \frac{k_r}{y}\frac{\partial \phi_s}{\partial x_s}(1,y) - \frac{\theta(1-k_r)(y-1)}{y}\right] \tag{3.58}$$

$$y\big|_{t=0} = 1 \quad \phi_s\big|_{t=0} = \upsilon x_s \tag{3.59}$$

$$\phi_{bt} = \psi \quad \phi_{bt}\big|_{t=0} = 1 \quad at \quad x_l = 0 \tag{3.60}$$

The finite difference method can be used to solve this full two-phase Stefan problem using a time step Δt. In the liquid region, h_l is space grid size for the variable x_l and $i = 0, 1, 2, \cdots, M_l$ is set for grid points of x_l. $i = 0$ corresponds to the position of liquid-solid interface, and $i = M_l$ is towards the position of outer boundary of the sphere. $\phi_{l0}^n, \phi_{l1}^n \; and \; \phi_{l2}^n$ are neighbouring points of the melted region front at time $n\Delta t$. In the solid region, h_s is the space grid size for the variable x_s and $j = 0, 1, 2, \cdots, M_s$ is set for grid points of x_s. $j = 0$ corresponds to the position of solid-liquid interface, and $j = M_s$ is towards the centre of the sphere. $\phi_{s0}^n, \phi_{s1}^n \; and \; \phi_{s2}^n$ are neighbouring points of the solid region, which is close to solid-liquid interface at time $n\Delta t$. The forward Euler scheme for the time derivative is employed to make Eq. (3.58) discrete. Suppose $\hbar_l$ and $\hbar_s$ represent the second-order difference for $\frac{\partial \phi_l}{\partial x_l}(1,y)$ and $\frac{\partial \phi_s}{\partial x_s}(1,y)$, then $\hbar_l = \frac{3\phi_{l0}^n - 4\phi_{l1}^n + \phi_{l2}^n}{2h_l}$ and $\hbar_s = \frac{3\phi_{s0}^n - 4\phi_{s1}^n + \phi_{s2}^n}{2h_s}$.

Eq. (3.58) in discretized form is expressed as:

$$y^{n+1} = y^n - \frac{\zeta''\Delta t}{y^n}\left[\frac{1}{(y^n-1)}\hbar_l - \frac{k_r}{y^n}\hbar_s - \frac{\theta(1-k_r)(y^n-1)}{y^n}\right] \tag{3.61}$$

The following discretized form for Eq. (3.55) of the liquid region is produced by the Implicit Euler scheme for the time derivative and the central difference scheme for the space derivative.

$$\frac{\phi_{l(i+1)}^{n+1} - 2\phi_{li}^{n+1} + \phi_{l(i-1)}^{n+1}}{h_l^{\,2}} = -(y^{n+1}-1)\kappa\left[\left(\frac{\phi_{li}^{n+1} - \phi_{li}^{n}}{y^{n+1} - y^n}\right)(y^{n+1}-1) - x_{li}^{n+1}\frac{\phi_{l(i-1)}^{n+1} - \phi_{l(i+1)}^{n+1}}{2h_l}\right], \tag{3.62}$$

where $\kappa = \dfrac{\zeta''}{y^n}\left[\dfrac{1}{(y^n-1)}\hbar_l - \dfrac{k_r}{y^n}\hbar_s - \dfrac{\theta(1-k_r)(y^n-1)}{y^n}\right]$

Equation (3.62) can be simplified as:

$$a_{li}\phi_{l(i-1)}^{n+1} + b_{li}\phi_{li}^{n+1} + c_{li}\phi_{l(i+1)}^{n+1} = \phi_{li}^{n}, \tag{3.63}$$

where

$$a_{li} = \frac{cof_{l1} - cof_{l3}}{cof_{l2}}, \quad b_{li} = 1 - \frac{2cof_{l1}}{cof_{l2}}, \quad c_{li} = \frac{(cof_{l1} + cof_{l3})}{cof_{l2}}$$

$$cof_{l1} = \frac{1}{h_l^2(y^{n+1}-1)\kappa}, \; cof_{l2} = \frac{y^{n+1}-1}{y^{n+1}-y^n}, \; cof_{l3} = \frac{x_{li}^{n+1}}{2h_l}$$

The equation (3.63) can be written into a matrix form:

$$\begin{bmatrix} b_{l1} & c_{l1} & 0 & \cdots & \cdots & 0 \\ a_{l2} & b_{l2} & c_{l2} & 0 & \cdots & 0 \\ \cdots & \cdots & \cdots & \cdots & \cdots & 0 \\ 0 & \cdots & 0 & a_{/(M_l-2)} & b_{l(M_l-2)} & c_{l(M_l-2)} \\ 0 & 0 & \cdots & 0 & a_{l(M_l-1)} & b_{l(M_l-1)} \end{bmatrix} \begin{bmatrix} \phi_{l1}^{n+1} \\ \phi_{l2}^{n+1} \\ \cdots \\ \phi_{l(M_l-2)}^{n+1} \\ \phi_{l(M_l-1)}^{n+1} \end{bmatrix} = \begin{bmatrix} \phi_{l1}^{n} - a_{l1}\phi_{l0}^{n+1} \\ \phi_{l2}^{n} \\ \cdots \\ \phi_{l(M_l-2)}^{n} \\ \phi_{l(M_l-1)}^{n} - c_{l(M_l-1)}\phi_{lM_l}^{n+1} \end{bmatrix} \tag{3.64}$$

The discretized form for Eq. (3.54) of solid region is described as:

$$\frac{\phi_{s(j+1)}^{n+1}-2\phi_{sj}^{n+1}+\phi_{s(j-1)}^{n+1}}{h_s{}^2}=-\frac{y^{n+1}\kappa}{\alpha_r}\left[\left(\frac{\phi_{sj}^{n+1}-\phi_{sj}^{n}}{y^{n+1}-y^{n}}\right)y^{n+1}-x_{sj}^{n+1}\frac{\phi_{s(j-1)}^{n+1}-\phi_{s(j+1)}^{n+1}}{2h_s}\right] \tag{3.65}$$

Which can then be simplified as before as:

$$a_{sj}\phi_{s(j-1)}^{n+1}+b_{sj}\phi_{sj}^{n+1}+c_{sj}\phi_{s(j+1)}^{n+1}=\phi_{sj}^{n}, \tag{3.66}$$

where

$$a_{sj}=\frac{cof_{s1}-cof_{s3}}{cof_{s2}},\ b_{sj}=1-\frac{2cof_{s1}}{cof_{s2}},\ \ c_{sj}=\frac{\left(cof_{s1}+cof_{s3}\right)}{cof_{s2}}$$

$$cof_{s1}=\frac{\alpha_r}{h_s^2y^{n+1}\kappa},\ cof_{s2}=\frac{y^{n+1}}{y^{n+1}-y^{n}},\ \ cof_{s3}=\frac{x_{sj}^{n+1}}{2h_s}$$

Eq. (3.66) can also be written into a matrix form, as before:

$$\begin{bmatrix} b_{s1} & c_{s1} & 0 & \cdots & \cdots & 0 \\ a_{s2} & b_{s2} & c_{s2} & 0 & \cdots & 0 \\ \cdots & \cdots & \cdots & \cdots & \cdots & 0 \\ 0 & \cdots & 0 & a_{s(M_s-2)} & b_{s(M_s-2)} & c_{s(M_s-2)} \\ 0 & 0 & \cdots & 0 & a_{s(M_s-1)} & b_{s(M_s-1)} \end{bmatrix}\begin{bmatrix} \phi_{s1}^{n+1} \\ \phi_{s2}^{n+1} \\ \cdots \\ \phi_{s(M_s-2)}^{n+1} \\ \phi_{s(M_s-1)}^{n+1} \end{bmatrix}=\begin{bmatrix} \phi_{s1}^{n}-a_{s1}\phi_{s0}^{n+1} \\ \phi_{s2}^{n} \\ \cdots \\ \phi_{s(M_s-2)}^{n} \\ \phi_{s(M_s-1)}^{n}-c_{s(M_s-1)}\phi_{sM_s}^{n+1} \end{bmatrix} \tag{3.67}$$

Based on the above algorithm, a C++ program was developed to solve this two-phase melting problem of micro/nano PCM particles. The parameter values $\alpha_r=1$, $k_r=1$, $\theta=0.1$, $\upsilon=-1$, Stefan number $\zeta''=1$ and $\zeta''=0.1$ are chosen for the test analysis. The shell boundary temperature is assumed as being at a constant temperature T_b^*, i.e. $T_{bt}=1$. 20 grid points are used in the liquid phase and solid phase, respectively, and a time step of $\Delta t=0.00002$ is select. The relationship between the dimensionless moving melting front and the dimensionless time is shown in Fig. 3.15. The dimensionless temperature profiles are calculated at radial distances within the spherical particle for $R(t)$

= 0.1 – 0.9, in steps of 0.1, as shown in Fig.3.16. The results from the Implicit Euler scheme of Eq. (3.62) and Eq. (3.65) are compared with those of Mccue and Hill [59], who used central finite differences to approximate the spatial derivatives and employed forward finite differences for the temporal derivatives. 120 spatial grid points in the solid phase and 80 in the liquid were adopted, and the time step $\Delta t = O\left(10^{-8}\right)$ was chosen. At Stefan number $\zeta'' = 1$, the time they calculated for $R(t)$ = 0.8, 0.6, 0.4, 0.1 was *t* = 0.045, 0.124, 0.194, 0.245, respectively; At $\zeta'' = 0.1$, the time for $R(t)$ = 0.8, 0.6, 0.4, 0.2, 0.1 was *t*= 0.197, 0.612, 1.086, 1.452, 1.547, respectively. The results from the current model, which are exhibited in Fig. 3.15 and Fig. 3.16, are very close to their results, and obviously the Implicit Euler scheme has a rapid convergent speed.

The melting time in the case of a big Stefan number $\zeta'' = 1$ is shorter than the small Stefan number $\zeta'' = 0.1$, due to the effect of latent heat. Superheating occurs completely in the solid phase at $R = 0.3$ position for $\zeta'' = 1$ due to the adiabatic conditions within the core and the moving interface at a faster speed. Hence, a critical radius R_c can be derived for a two-phase melting problem of micro/nano particles at some given conditions, and at this position, the melting has completed and this suggests that the mathematical solution will cease to exit.

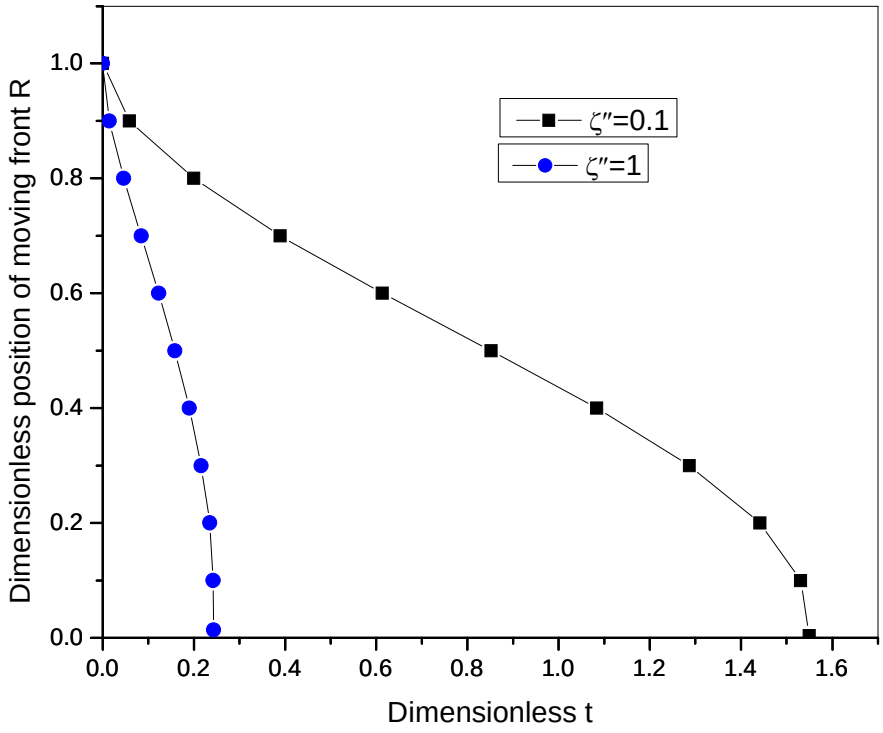

Figure 3.15: Dimensionless melting front versus time at ζ'' =0.1 and ζ'' =1

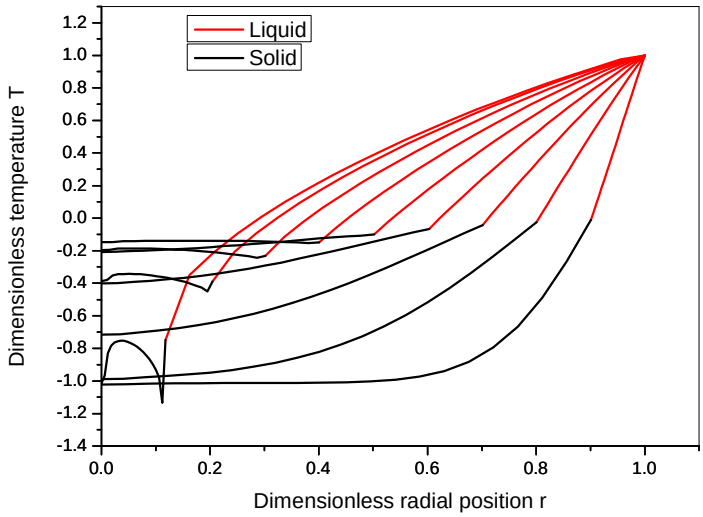

(a)

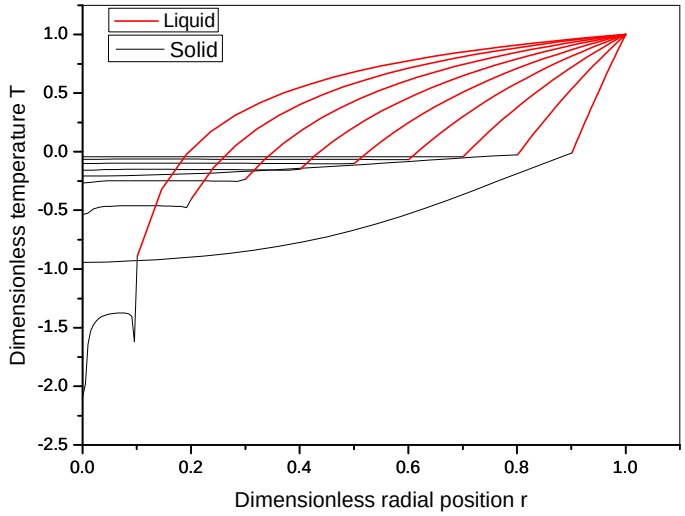

(b)

Figure 3.16: Dimensionless temperature evolution in liquid-solid two phase region at (a) ζ″ =1 for time t= 0.014, 0.046, 0.085, 0.123, 0.159, 0.190, 0.216, 0.235, 0.243; (b) ζ″ =0.1 for time t=0.059, 0.200, 0.390, 0.614, 0.852, 1.083, 1.287, 1.442, 1.531

3.4 Conclusions

In order to explore the effect of binary phase composition on the solidification of an encapsulated metallic composites particle, a model has been proposed and applied to the case of a moving liquid–solid interface. For some alloy materials with a complicated relationship between the freezing temperature and solid fraction, a numerical interpolation and local linear rule is used. Compared with the solidification of pure metal solved by the traditional model, the new liquid–solid interface model can clearly explain the solidification behaviour of the alloy under different cooling conditions. The model is also suitable for other mixtures of PCM particles, as long as the relationship between the solid fraction and the freezing temperature is

established.

For differently-sized micro/nano PCM particles, a new liquid-solid interface model for an individual particle is developed, using an initial melting point and the Gibbs-Thomson equation. A full two-phase melting model of a particle is also built and solved by the finite difference solution. The real time temperature of liquid-solid interface can decrease with the change of curvature radius of liquid-solid interface and its effect directly impacts on the progress of the melting process.

The modelling approach outlined in this Chapter will be used in Chapter 6 to study the melting behaviour of DPNT06-0182 microcapsules, whilst exhibiting heat transfer under experimental conditions within a pipe.

Chapter 4

Construction of a test rig for forced convective heat transfer of MPCS

Summary

A test rig has been developed to explore the melting heat transfer behaviour of a microcapsule phase change slurry (MPCS) as it flows through a circular tube for a given constant heat flux. The system was designed to investigate the situation of a heating and cooling cycle for slurries. The experimental system was first validated by using water as a test medium. Here, the pressure drop was measured using a highly-accurate pressure transducer, and compared with the predictions of Colebrook-White and Blasius equations. In addition, system errors introduced due to the effects of local wall temperatures were analyzed by using an empirical Petukhov correlation. This process gave confidence that the test rig was working as planned, and was thus suitable for later experiments on MPCS.

4.1 Background

As discussed in Chapter 1, conclusions regarding the thermal characteristics of MPCS could be considered to be somewhat incomplete and controversial. This is because the systems described previously did not provide complete evidence as to whether the phase change of MPCM particles was complete during the experiment, and also did not provide some estimate of the physical state of the PCM at the inlet (e.g. whether it was

solid or not). In our experimental system, the measurements should truly reflect the effect of latent heat of MPCM particles. Generally, most PCMs have a melting and freezing temperature range, and the supercooling phenomenon may also be observed. Thus, the experimental system for the study of MPCS should be designed in such a way that (a) the phase change of the encapsulated MPCM will be fully completed within the test section, and (b) the influence of supercooling phenomena is excluded.

4.2 System design of the test rig and key components

With the above in mind, the experimental system that was used in this research was designed to accurately measure heat transfer parameters of an MPCS, flowing through a circular tube, for a given heat flux. In order to completely measure the effect of phase change within MPCS flow in a nearly steady-state, the system was designed to have both heating and cooling circulation functions. The cooling sub-system had the ability to control the temperature of the inlet, and was thus able to remove the effect of subcooling.

The system design is illustrated in Fig. 4.1, with a photograph of the completed test rig being shown in Fig. 4.2. The slurry was stored in a reservoir tank, and driven around the test rig using a STW 225/1-H/K pump. The MPCS was thus caused to pass through the test section, and thereafter return to the tank. During this closed loop flow cycle, the flow rate of the slurry was adjusted to the required value by adjusting the frequency of the pump. During the experiment, the flow velocity at a point just before the test section (see Fig. 4.1) was measured using a Cynergy3 UF25B ultrasonic flow meter, shown in Fig. 4.3 (a), which was provided by RS Components Ltd.

The measurement range of the flow meter was between 0.2 and 25 l/min. A second digital flow meter, again supplied by RS Components, was also installed, and used for calibration and real-time display, as shown in Fig.4.3 (b). This digital flow meter used a free-running Pelton wheel turbine within a specially shaped chamber. The rotation of the rotor was detected with a Hall Effect sensor, and the output frequency of these pulses was directly proportional to the flow rate. The flow rate could be measured within the range 50 ml – 10 l/min. The two flow meters were installed for more stable and accurate measurements, because the ultrasonic flow meter cannot be used to measure very slow flow rates and the digital flow meter has a bigger error in measurement of very fast flow rates. The combination allowed a wide range of flow rates to be measured.

The test section was designed to measure heat transfer parameters of fluids, and was constructed using a half-hard Copper tube, heated using rope heaters. Within the restrictions of the available space for the test rig, and the fact that a full phase change of MPCS needed to be observed, the length of the tube was selected as 2.4 m. The inside diameter of the tube was 10 mm and the outside diameter was 12 mm. The tube had eight OMEGALUX FGR-100 Rope Heaters coiled around its outer surface, as shown in Fig.4.4. Each rope had a power rating of 500 W, so that the maximum heating power available was 4 kW for the tube within the test section. The heat flux of the resistance rope heaters could be adjusted by changing the charging voltage of the AC transformer, and this was measured and displayed by a power meter. Thermal insulation materials (glass-fibre wool) were added to reduce heat losses.

In the experimental design, 13 thermocouples were uniformly soldered onto the outside wall of the testing tube, to measure the temperatures of the wall; 5 thermocouples were also inserted into the centre line of the tube in order to measure temperatures within the fluid itself.

The brazed plate heat exchanger CB60-30H from Alfa Laval Ltd, shown in Fig.4.5, worked in unison with the TAE evo 015 chiller from ICS Ltd (Fig.4.6) to cool the fluid flowing out from the test section. Alfa Laval Ltd provided the technical specifications of the CB60-30H heat exchanger, in situations where it was operated together with the TAE evo 015 chiller. Based on the thermo-physical parameters of a particular DPNT06-0182 slurry, operating under the conditions shown in Table 4.1, the heat exchanger/chiller combination was capable of extracting 7.3 kW thermal duty. The cooling fluid supply temperature was 15 °C and the cooling fluid return temperature was 20 °C. This meant that the temperature of the hot-side inlet of the heat exchanger will decrease from 30 °C to 20 °C at the hot-side outlet. Therefore the inlet temperature of the test section under the constant heat flux (lower than 4 kW) could be guaranteed to be below the lowest temperature of the freezing temperature range of the PCM particles within the MPCS that was used. This in turn meant that the impact of the subcooling phenomenon was removed from our experimental system. Moreover, the temperature of the fluid within the test section could be controlled by adjusting the heat flux and flow rates, so that the heat transfer performance of the MPCS could be measured under three different situations within an experiment that approached steady state conditions, namely (a) an entire phase change, (b) a part phase change and (c) no phase change. This illustrates that the experimental test rig provided a

range of measurement possibilities for a heating and cooling cycle for MPCS under flow conditions, and hence demonstrated that the design was very appropriate for our purposes.

In addition to the above, a differential PMP 5023 Pressure Transducer from GE Measurement & Control Solutions (shown in Fig.4.7) was employed to measure the pressure drop across the test section. The pressure range of the wet differential measurement was 1 bar. More importantly, the pressure transducer was designed to have a full thermal calibration, and a compensated temperature range of -40 °C to +125 °C was available. Note that the signals from the thermocouples, the ultrasonic flow meter and the pressure transducer were all recorded automatically using a 3595IC IMP data logger during the tests.

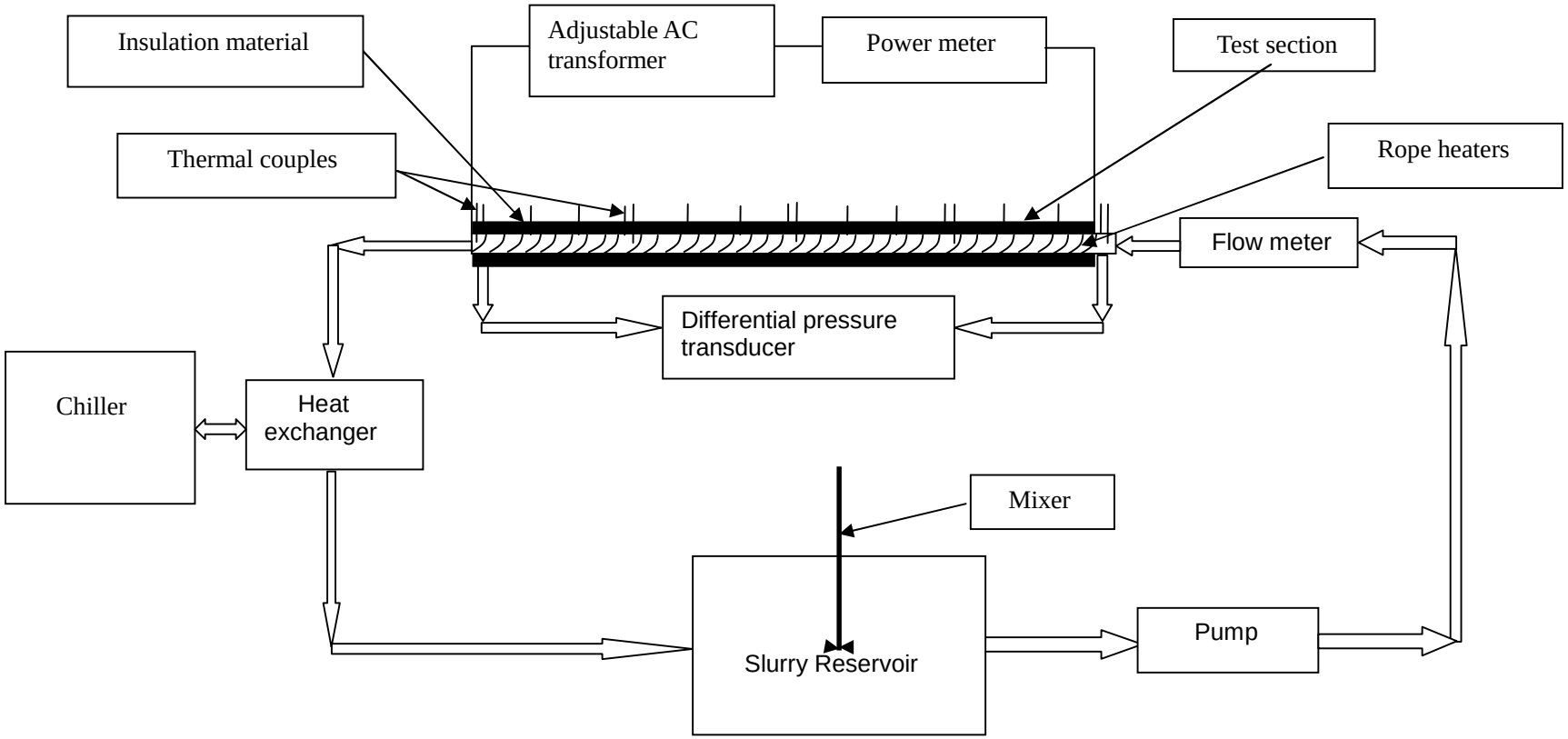

Figure 4.1: Schematic illustration of the experimental rig used for the study of MPCS

Figure 4.2: A photograph of the experimental test rig

(a) (b)

Figure 4.3: Flow meter sensors used within the test rig, using (a) the ultrasonic method, and (b) the frequency of pulses method

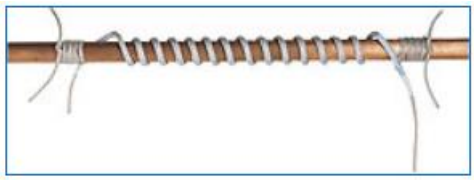

Figure 4.4: An illustration of the rope heaters used with the test section of the flow rig.

Figure 4.5: The CB60-30H Heat exchanger

Figure 4.6: The ICS TAE evo 015 Chiller

Table 4.1: Technical specifications of the CB60-30H heat exchanger

		Hot Side S1S2	**Cold side S3S4**
Fluid		Slurry	Water
Density	kg/m^3	981.5	998.2
Specific heat capacity	kJ/(kg K)	9.36	4.19
Thermal conductivity	W/(m K)	0.547	0.598
Flow behaviour		0.901263	
Consistency index	Pas^n	0.0441	
Viscosity inlet	cP	21.5	1.14
Viscosity outlet	cP	31.0	1.01
Mass flow rate	kg/h	280.8	1253
Inlet temperature	°C	30.0	15.0
Outlet temperature	°C	20.0	20.0
Pressure drop	kPa	3.85	6.09
Heat Exchanged	kW	7.300	
L.M.T.D.	K	7.2	
O.H.T.C clean conditions	$W/(m^2 K)$	801.1	
O.H.T.C service	$W/(m^2 K)$	622.3	
Heat transfer area	m^2	1.62	
Duty margin	%	28.0	
Relative directions of fluids		Countercurrent	
Number of passes		1	1

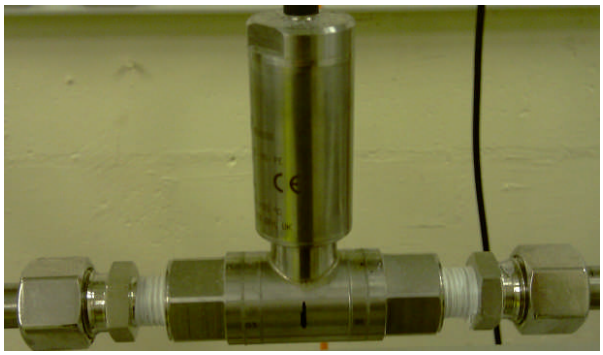

Figure 4.7: The differential PMP 5023 Pressure Transducer from GE

4.3 Experimental system validation

The validation of the experimental system was accomplished by testing the apparatus using water as the fluid being pumped around the system. The results were then compared with known empirical theoretical values, noting that an optimal prediction effort should be a judicious combination of computation and experiment [110]. The pressure drop, the wall temperatures and the temperatures of water in set positions of the test section were measured under different flow rates for a given heat flux, and a few important additional parameters were also calculated. The reliability of the experimental system could thus be demonstrated by calibration with the known experimental parameters of water.

Consider the case where the hydrodynamic entrance length of a tube is L_E, the inside diameter of the tube is D, the mean velocity of fluid is u_m and the kinematic viscosity is υ. Under these conditions, the Reynolds number Re_D is defined as

$$\mathrm{Re}_D = \frac{u_m D}{\upsilon} \tag{4.1}$$

The Reynolds number is used as a criterion for laminar and turbulent flow. The flow is usually observed to be turbulent for $\mathrm{Re}_D > 2300$. On the other hand, transitional flow within the range $2300 \le \mathrm{Re}_D < 10^4$ may be observed [135]. The test section might be considered as a hydrodynamically fully developed region if some specific conditions are met. For example, for laminar flow, Blasius' condition is given by:

$$\frac{L_E/D}{\mathrm{Re}_D} = 0.01; \tag{4.2}$$

the Sparrow integral solution is:

$$\frac{L_E/D}{\mathrm{Re}_D} = 0.026, \tag{4.3}$$

and the Schlichting's result is given by

$$\frac{L_E/D}{\mathrm{Re}_D} \cong 0.04. \tag{4.4}$$

Note that the results are all of the same order of magnitude. For turbulent flow, the full development criterion is:

$$\frac{L_E}{D} \cong 10, \tag{4.5}$$

which is particularly applicable to fluids with Prandtl numbers of order 1 [112]. Note that in our experimental rig, the entrance length of tube from pump to the test section is nearly 2.25 m, which means the test section is located in the hydrodynamically fully-developed region either for laminar flow or turbulent flow.

4.3.1 Pressure drop validation

For a fully-developed fluid, the pressure drop can be described using the Darcy-Weisbach equation [113], which can be written as:

$$\Delta P = f_D \frac{L}{D}\left(\frac{1}{2}\rho u_m{}^2\right), \tag{4.6}$$

where ΔP is pressure loss, f_D is the Darcy friction factor, L is length of the test tube, and ρ is the density of fluid. For laminar flow in a tube,

$$f_D = 64/\mathrm{Re}_D\,, \tag{4.7}$$

whereas for turbulent flow in a tube, if Darcy friction factor is determined from Blasius equation [112], then the value is given by

$$f_D \cong 4 \times 0.0791\,\mathrm{Re}_D^{-1/4}\,. \tag{4.8}$$

For developed fluids at Reynolds numbers greater than 4000, the Darcy friction factor can be defined by the Colebrook-White equation [114, 115]:

$$\frac{1}{\sqrt{f_D}} = -2\log_{10}\left(\frac{\varepsilon}{3.7D_h} + \frac{2.51}{\mathrm{Re}_D\sqrt{f_D}}\right)\,, \tag{4.9}$$

where ε is roughness height, D_h is hydraulic diameter, and for fluid-filled circular conduits, $D_h = D$. The Colebrook equation is an implicit equation that combines experimental results of studies of turbulent flow in smooth and rough pipes to determine the Darcy friction factor. The test tube in the experimental test-rig is made of half-hard Copper, and the value of ε for this material can be determined from the Moody Chart [113] as ε = 0.0015 mm.

Since the PMP 5023 Pressure Transducer is provided with a full thermal calibration, the measurement of pressure drop can attain a high accuracy

even in the presence of changes in temperature. According to calculations of the bulk mean temperatures of MPCS under different heating powers, and for the flow rates which the test system could provide, only the heat flux was approaching or bigger than 3.5 kW (even if under the lowest flow rates), the PCMs were expected to exhibit their entire phase change. Hence, 5 different flow rates at a heating power of 3.5 kW were selected for system validation.

The thermal properties of water under certain temperatures are shown in Table 4.2. The mean values of the temperature range of fluid were used in the calculation of equations (4.8), (4.9) and (4.6), and so linear interpolation was used to obtain the thermophysical parameters of mean values based on the fluid temperature range in Table 4.2. For example, for fluids within the experimental test section, the bulk mean temperature of the inlet is 14.5 °C and the bulk mean temperature of outlet is 18.8 °C. Linear interpolation was used to obtain thermophysical parameters of water at a mean temperature of 16.65 °C, and these were used to calculate the pressure drop. In addition, a series of measured data were collected from the data logger for a fixed flow rate. The mean values of these measured data were used for the pressure analysis, in order to reduce the effects of random errors.

The corresponding theoretical calculated results from equations (4.8), (4.9) and (4.6) are shown in Table 4.3, together with the measured values. Note that the temperature-dependent parameters were used for the calculations. As seen in Table 4.3, the measured values are basically in concurrence with the theoretical predicted values from either the Blasius

equation or the Colebrook-White equation. The errors are different for different flow rates, and the biggest error appears in the slowest flow rate. However the error is lower than 20%. Considering that the measured values depend on the temperature compensated algorithm of the pressure transducer, and the empirical equations are from different solutions and usually obtained based on the assumption that the properties of fluid are constant under certain temperature range, so errors between them are unavoidable.

Table 4. 2: Thermal properties of water [116]

T (°C)	ρ (kgm^{-3})	υ ($m^2s^{-1} \times 10^{-6}$)	Pr
10	999.8	1.307	9.47
20	998.3	1.004	7.01
30	995.7	0.801	5.43
40	992.3	0.658	4.34
50	988.0	0.553	3.56

Table 4.3: Pressure drop of water for heat flux 3500 W and different flow rates

Volume flow rate ($l(min)^{-1}$)	11.5	9.47	7.33	5.09	2.83
mean velocity (ms^{-1})	2.44	2.01	1.56	1.08	0.60
Fluid temperature range (°C)	14.5-18.8	14.5-19.7	14.5-21.2	14.5-24.2	14.6-32.1
Kinematic viscosity ($m^2s^{-1} \times 10^{-6}$)	1.104	1.090	1.068	1.022	0.9363
Density (kgm^{-3})	998.9	998.8	998.7	998.4	997.5
Re_D	22128	18434	14562	10566	6425
Darcy friction factor from Colebrook white equation	0.0274	0.0284	0.0298	0.0320	0.0361
Darcy friction factor from Blasius equation	0.0260	0.0272	0.0288	0.0312	0.0353
Calculated ΔP based Colebrook white friction factor (Pa)	19616	13737	8641	4469	1562
Calculated ΔP based Blasius friction factor (Pa)	18562	13137	8353	4362	1531
Measured ΔP (Pa)	17359	12573	8065	4359	1878
Pressure error between Colebrook result and measured value	13%	9.26%	6.67%	2.52%	-16.8%
Pressure error between Blasius result and measured value	6.93%	4.49%	3.57%	0.069%	-18.5%

4.3.2 Correction for wall temperatures

The local convective heat transfer coefficient h, between a fluid flow and the inner tube wall is defined as [84]:

$$h = \frac{q_w}{T_{wi} - T_b} \quad \text{and} \quad q_w = \frac{Q}{A_i}, \tag{4.10}$$

where T_b is the local bulk mean temperature; T_{wi} is the inner wall temperature; q_w is the local heat flux at the inner surface of wall; Q is the total heat supplied by the heater and measured by a watt meter and A_i is the tube inner surface area. The inner wall temperature T_{wi} can be calculated from the steady-state conduction equation of cylinders with length very large compared to diameter [111]:

$$T_{wi} = T_{wo} - \frac{QIn\left(R_o / R_i\right)}{2\pi k_w L}, \tag{4.11}$$

where T_{wo} is the outer wall temperatures, which were measured by thermal couples (1.0 mm diameter x 150 mm long stainless steel sheath provided by TC company). The thermal couples were soldered on the wall; R_o and R_i are the outer and inner tube radius, respectively; k_w is thermal conductivity of wall material and here the pure Copper thermal conductivity $k_w = 400$ W(mK)$^{-1}$ was adopted [98].

In the case of water, the change of water specific heat capacity $c_{p,w}$ with temperature is very small within the range 14.5 – 50 °C, and thus it is reasonably taken to be constant along the length of the measurement area. Thus, $c_{p,w}$ = 4.18 kJ(kgK)$^{-1}$ is adopted here [117]. From the point of view of the stream as an elongated control volume, the bulk temperature

represents an energy average, so the total energy Q_x added from the inlet to x position can be expressed by the conservation of energy equation [111] as:

$$Q_x = \dot{m} c_{p,w} \left(T_{bx} - T_{in}\right); \quad Q_x = Q \frac{x}{L} \ , \tag{4.12}$$

where $\dot{m}$ is mass rate of flow; T_{in} is the temperature of inlet. From Eq. (4.12), the bulk mean temperature of water can be calculated. The Nusselt number Nu_D is expressed as:

$$Nu_D = \frac{hD}{k} \ , \tag{4.13}$$

where k is the thermal conductivity of the fluid. An empirical relation of the Nusselt number was proposed by Sieder and Tate [118] for laminar heat transfer in tubes:

$$Nu_D = 1.86 \left(\mathrm{Re}_D \, \mathrm{Pr}\right)^{1/3} \left(\frac{D}{L}\right)^{1/3} \left(\frac{\mu}{\mu_w}\right)^{0.14} \ , \tag{4.14}$$

where μ is the dynamic viscosity of the fluid, and Pr is Prandtl number defined as:

$$\mathrm{Pr} = \frac{\upsilon}{\alpha} = \frac{\mu / \rho}{k / \rho c_p} = \frac{c_p \mu}{k} \, . \tag{4.15}$$

Note that all the above fluid properties were evaluated at the mean bulk temperature of the fluid, except μ_w , which was evaluated at the wall temperature.

For forced convection in turbulent flow in tubes, the Petukhov correlation [135, 136] can be used to calculate the Nusselt numbers for constant heat flux, i.e.,

$$Nu_D = \frac{(f_D/8)\mathrm{Re}_D\,\mathrm{Pr}}{1.07 + 12.7(f_D/8)^{1/2}\left(\mathrm{Pr}^{2/3} - 1\right)}\ , \qquad (4.16)$$

Eq. (4.16) is regarded by many authors as being most accurate as well as the most used [135]. For example, Gnielinski in his publications used it as basis for their Nu-correlation [137] [138]. The definition range of Eq. (4.16) is $4 \cdot 10^3 \le \mathrm{Re}_D \le 5 \cdot 10^5$ and $0.7 \le \mathrm{Pr} \le 60$ [135].

The measured temperatures of water were obtained from the 5 thermocouples inserted along the central axis of the tube. The bulk mean temperatures of water at the 12 equally-spaced locations were calculated from Eq. (4.12). The temperatures of the inside wall were converted in Eq. (4.11) from the measured outside wall temperatures, which were in turn obtained from the 13 thermal couples soldered onto the wall. Because the forced convective water in our test is likely to have been turbulent (as shown in Table 4.3, except with the lowest mean rate with $\mathrm{Re}_D \approx 6450$ where it can be considered as a transition region, others have Re_D more than 10^4 and so are turbulent), the theoretical wall temperatures were calculated from Eqs. (4.16), (4.13) and (4.10), and the calculated parameters were based on the average temperature of the bulk mean temperature and the inside wall temperature (Here the inside wall temperature adopted the points on the least-square fitting line of measured inside wall temperatures in order to reduce the magnitude of errors). As an example, the calculated parameters at mean velocity $u_m = 0.60$ ms^{-1} are shown in Tables 4.4. The heat transfer parameters at this value of mean velocity are presented in Table 4.5.

Throughout the whole test system, measured errors were unavoidable for wall temperatures, because the tube was heated by rope heater coils and

slight spacings in the coil was needed for placement of the thermal couples via soldering. This leads to uneven heat flux on the tube. Delgado *et al.* [73] used the same heating method as us, and they summarized the three reasons for establishment of a correction mode for the wall temperatures, as follows:

- Interruption of the heat flux caused by the presence of a thermocouple is necessary;
- Possible influence of the heat flux on the thermocouple (possible increase in temperature);
- Heat losses from the thermocouple to the ambient surroundings.

It should be noted, however, that Delgado *et al.* [73] did not install thermocouples to measure the various temperatures of the fluid, because the bulk mean temperatures of the fluid may obtained by calculation. In order to observe the wanted features of the fluid in our test rig and provide a comparision to the calculated bulk mean temperatures of non-single-phase fluid, 5 thermocouples were inserted evenly in the tube along its length to measure the temperature of the fluid at the centre, and an additional five thermocouples were soldered onto the outside wall at the same locations, so as to measure the corresponding temperatures of the outside wall. Therefore, the presence of thermocouples will change the heat flux and may result in a lower wall tempeatures at the 4 positions which are close to the measured points of fluid (excluding the no heating point of inlet*).* Therefore, the Petukhov correlation (Eq. 4.16) can be used to calculate the Nusselt numbers and local heat transer coefficients, which in turn can be used to determine the ideal local wall temperatures. The measured errors of wall

temperatures were analyzed as follows:

As seen in Fig.4.8, considering the two situations of the lowest flow rate and the highest flow rate, the measured wall temperatures was fitted by least-equare method and compared with the predicted wall temperatures by the Petukhov correlation. Apparently the main errors are bias errors which resulted from the non-uniform heat flux due to installation of thermal couples. The distribution of error bars may differ for different flow rates. For example, the error of the eighth plotted point presented a small negative error under the lowest flow rate, but for the highest flow rate, it exhibited a big positive error.

The water temperature values along the test length for five different flow rates are presented in Fig. 4.9, including the central line values, bulk mean temperatures, inside wall temperatures and calculated wall temperatures. The calculated bulk mean temperatures are consistent with the measured temperatures of the fluid under the five different flow rates. The measured wall temperatures increase along the test section, with local variations that were attributed to the existence of errors. However, the errors between the measured values and calculated values are within a reasonable range. For example, the maximum error of wall temperatures in Celsius scale for mean velocity u_m=0.60 ms^{-1} shown in Table 4.5 is 11.6%. A correction method will be used to correct the wall temperatures of MPCS in Chapter 5 to follow, in order to eliminate the influence of measurement system errors.

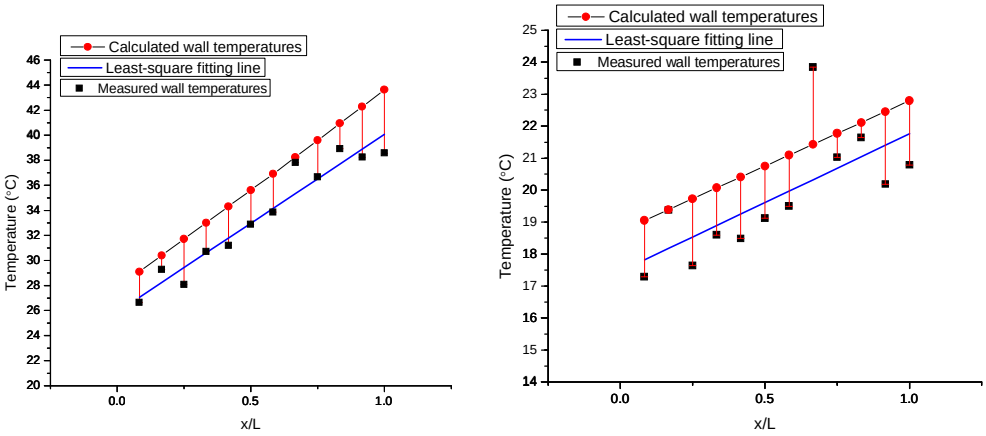

Figure 4.8: Errors of wall temperatures

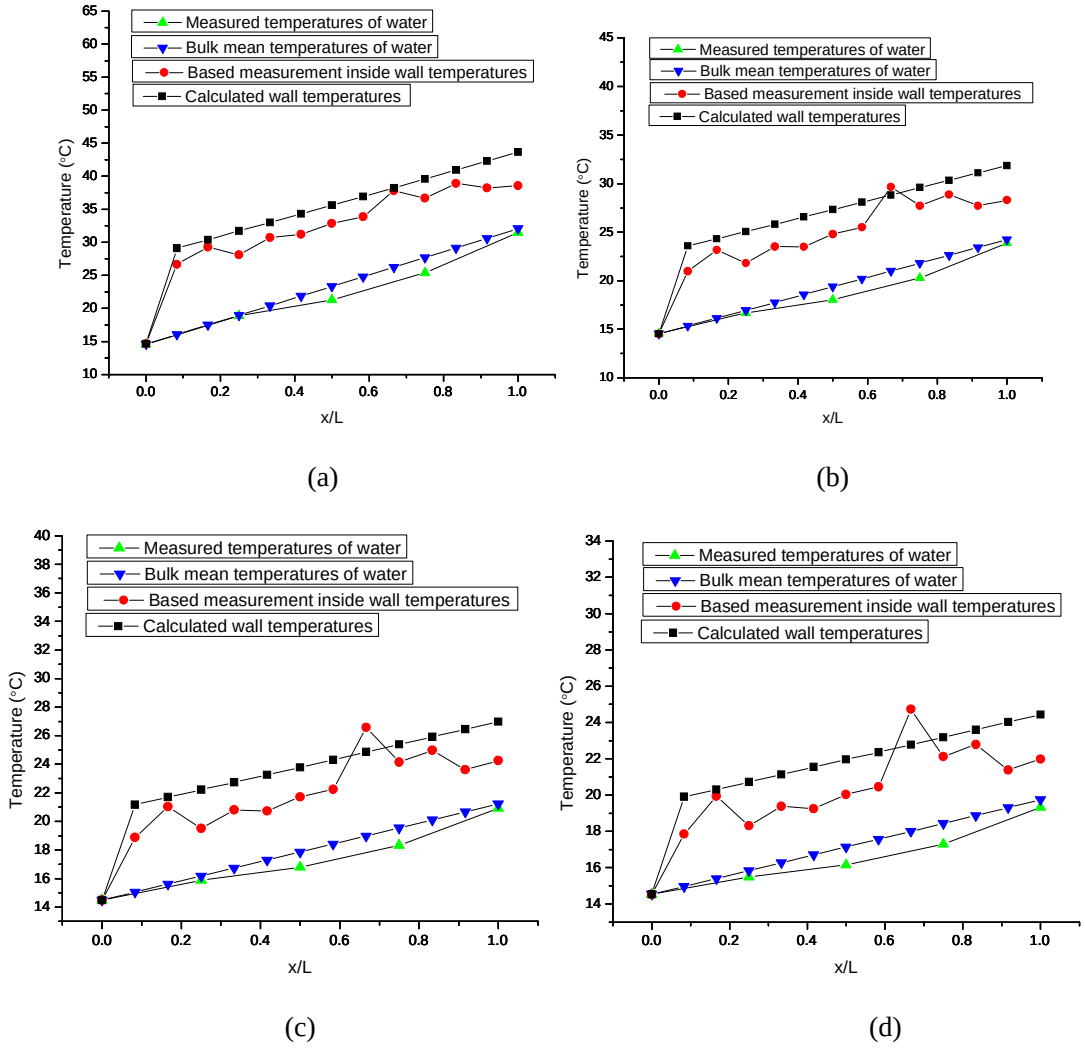

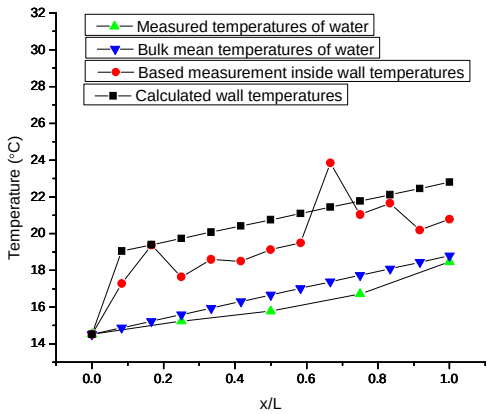

(e)

Figure 4.9: Temperature values for various locations, for values of mean velocity (u_m) of (a) 0.60 ms^{-1}, (b) 1.08 ms^{-1}, (c) 1.56 ms^{-1}, (d) 2.01 ms^{-1} and (e) 2.44 ms^{-1}

Table 4.4: The calculated parameters based on average temperature of bulk mean temperature and inside wall temperature at a mean velocity of $u_m = 0.60\ ms^{-1}$

Local position x/L	0.08	0.17	0.25	0.33	0.42	0.50	0.58	0.67	0.75	0.83	0.92	1.00
Average temperature (°C)	21.4	23.4	23.5	25.6	26.5	28.1	29.3	32.0	32.2	34.0	34.4	35.3
Kinematic viscosity (m^2s^{-1} x 10^{-6})	0.972	0.946	0.919	0.892	0.865	0.839	0.812	0.790	0.771	0.752	0.733	0.714
Re_D	6187	6362	6547	6743	6952	7174	7410	7617	7804	8000	8206	8424
P_r	6.76	6.56	6.35	6.14	5.93	5.72	5.51	5.34	5.20	5.06	4.91	4.77

Table 4. 5: Local heat transfer parameters and errors analysis at a mean velocity of u_m = 0.60 ms^{-1}

Local position x/L	0.08	0.17	0.25	0.33	0.42	0.50	0.58	0.67	0.75	0.83	0.92	1.00
Calculated Nu_d	58.11	58.77	59.45	60.16	60.89	61.65	62.43	63.10	63.70	64.31	64.94	65.58
Calculated h ($Wm^{-2}K^{-1}$)	3486	3526	3567	3610	3653	3699	3746	3786	3822	3859	3896	3935
Predicted wall temperature (^0C)	29.10	30.40	31.71	33.01	34. 31	35.62	36.92	38.25	39.59	40.94	42.29	43.63
Based measured inside wall temperature (^0C)	26.66	29.29	28.08	30.72	31.20	32.87	33.85	37.82	36.67	38.92	38.24	38.58
Errors between predicted and measured wall temperatures in Celsius scale	8.4%	3.7%	11.4%	6.9%	9.1%	7.7%	8.3%	1.1%	7.4%	4.9%	9.6%	11.6%

4.3 Conclusions

A test rig has been developed to investigate the heat transfer characteristics of MPCS, as it flows through a tube under a constant heat flux. High accuracy sensors were used to measure key parameters throughout the whole system. The cooling sub-system, which consisted of a powerful chiller and a matching heat exchanger, provided a flexible method for adjustment of the inlet temperature of the test section, so that the entire phase change effect could be observed within the experiment.

The system accuracy was validated by using water as a test fluid. The measured pressure drops were compatible with the empirically-predicted values, although the resultant errors were relatively greater at the slowest flow rates, as might be expected. The errors of local wall temperatures were analyzed and estimated by the empirical and practical Petukhov correlation.

Chapter 5

Experimental investigation into the melting heat transfer characteristics of microcapsule phase change slurries

Summary

Microcapsule phase change slurries (using paraffin-based microcapsules of a PCM known as DPNT06-0182) were prepared with different mass fractions, based on microcapsule powder obtained from Ciba Specialty Chemicals, UK. The basic thermo-physical parameters of DPNT06-0182 slurries such as specific heat capacity, thermal conductivity and dynamic viscosity were determined from the measured values of DPNT06-0182 particles and slurries. Subsequently, the heat transfer characteristics of DPNT06-0182 slurries were investigated using the test rig described earlier in Chapter 4. In particular, a few important parameters of DPNT06-0182 slurries, such as local heat transfer coefficients and pressure drop, were examined carefully, as these involve the effect of phase-change latent heat.

5.1 Thermophysical properties of DPNT06-0182 slurries

The MPCS material was prepared by dispersing MPCM powder into a carrier fluid. The MPCM used here consisted of white DPNT06-0182 microcapsules, each capsule having 87.5% by weight of paraffin wax contained within of a cross-linked acrylic polymer as the outer shell (12.5%

by weight). The nominal particle size distribution was 10 - 100 μm [105]. Slurries were made with particle weight concentrations of 5% and 10% respectively. The basic thermophysical parameters of the DPNT06-0182 MPCM particles were measured as described below, and some properties of the resultant slurries then derived from empirical equations based on the measured values of the MPCM particles.

5.1.1 Specific heat capacity

The specific heat capacity $c_{p,s}$ of a suspension can be calculated using an energy equation [121] as follows:

$$c_{p,s} = (1 - c_m)c_{p,l} + c_m c_{p,PCM} \ . \qquad (5.1)$$

Here, c_m is the mass concentration; subscript l refers to the suspending fluid (which is water in this case, so that $c_{p,l}$ is considered as a constant), and $c_{p,PCM}$ is the specific heat capacity of PCM particles, which is a function of temperature due to the effect of phase change latent heat. The numerical value of $c_{p,PCM}$ can be obtained from a differential scanning calorimetry (DSC) test. The DPNT06-0182 particles were thus measured during the heating and cooling process by a SETARAM Instrumentation-D/SENSYS-2A differential scanning calorimeter. The test was carried out in air, at a constant heating and cooling rate of 0.2 °C/min. As seen in Fig. 5.1, the melting latent heat of DPNT06-0182 particles was 102.04 Jg^{-1}, and the melting temperature range was 24.99-38.2 °C. Note that there was a big under-cooling phenomenon present in DPNT06-0186 microcapsules, and hence the freezing temperature range was over a lower range of temperatures of 18.74 - 33.97 °C. It shows

that there is only one peak appearing in the DSC heating and two distinct peaks in the cooling. In a similar microencapsulated PCM system [139], the authors stated that during the crystallization of the paraffin mixture, the peak α is attributed to the heterogeneously nucleated liquid to rotator transition, and the peak β is attributed to the homogeneously nucleated liquid to crystal transition. Yamagishi et al. [84] indicated that the supercooling crystallization was caused by the decrease in the number of nuclei in each microcapsule due to the reduced diameter [105].

The specific heat capacity of DPNT06-0182 particles can also be derived from this DSC test, and hence the specific heat capacities of 5% and 10% concentration MPCS could be calculated from Eq. (5.1). The results are presented in Fig.5.2. During the melting phase, the DPNT06-0182 particles have a higher specific heat capacity range due to absorption of phase change latent heat. However, in the case of DPNT06-0182 slurries, the specific heat capacity decreases as a result of the low specific heat capacity of the carrier fluid, noting that the specific heat capacity of water stays constant over the temperature range of melting. Except for the melting range, the specific heat capacity of DPNT06-0182 slurries increases compared with DPNT06-0182 particles, since the specific heat capacity of water is higher than that of DPNT06-0182 particles while the PCM within each particle is either totally solid or totally liquid.

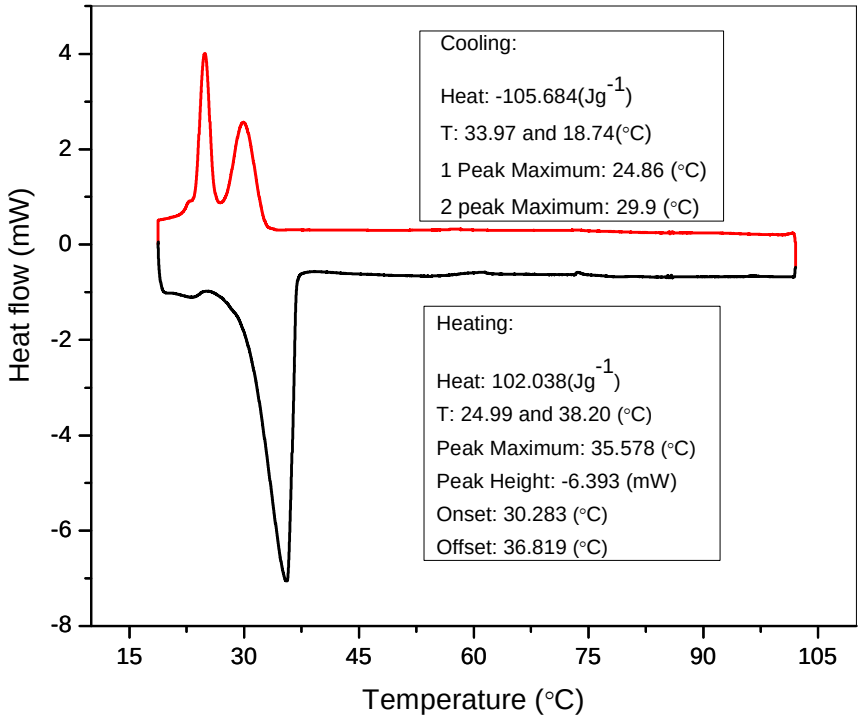

Figure 5.1: Heat flow curve of DPNT06-0182 microcapsules obtained from DSC measurements

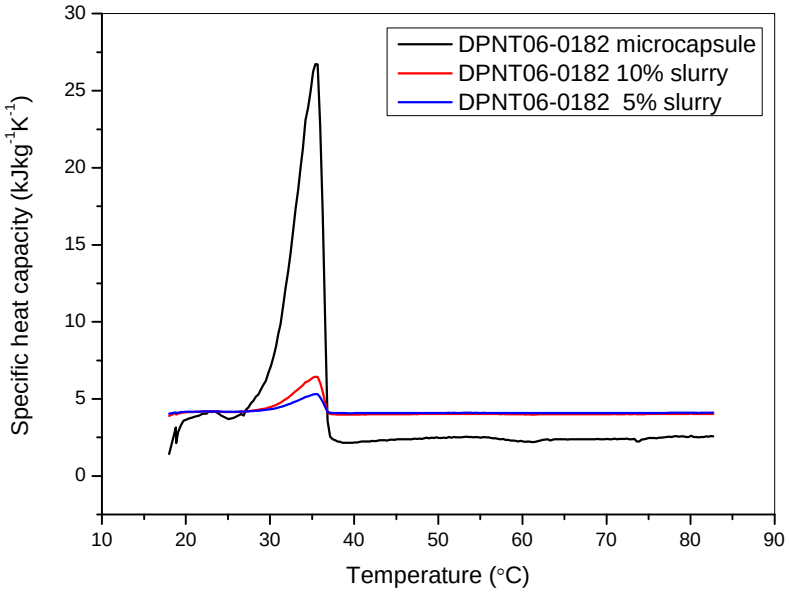

Figure 5.2: Specific heat capacity of DPNT06-0182 microcapsule and its slurries

5.1.2 Thermal conductivity and density of DPNT06-0182 slurry

According to Maxwell's work on the dielectric properties of composite materials, the following expression for the effective thermal conductivity of a liquid matrix which contains a dispersion of particles [74,122] is:

$$k_e = k_f\left[\frac{k_p + (n-1)k_f - (n-1)V_p(k_f - k_b)}{k_p + (n-1)k_f + V_p(k_f - k_b)}\right], \quad n = 3\ . \tag{5.2}$$

Here, k_e is the effective conductivity which is predicted for the composite; k_f is the conductivity of the liquid; k_b is the conductivity of particles; V_p is the particle volume fraction, and n is the empirical shape factor ($n = 3$ for a sphere).

The thermal conductivity of DPNT06-0182 particles was measured using a ThermTest^{TM} Hot Disk Instrument, model number TPS 2500S, and the value of k_b was found to be 0.249 $Wm^{-1}K^{-1}$ at 20 °C. The thermal conductivity of water (k_f) was 0.6 $Wm^{-1}K^{-1}$ at the same temperature [134], so the effective thermal conductivity k_e of different concentrations of DPNT06-0182 slurries could be calculated using Eq. (5.2). The measured densities and the effective thermal conductivities of DPNT06-0182 slurries are as shown in Table 5.1.

Table 5.1: Densities and thermal conductivities of DPNT06-0182 slurries at 20℃

DPNT06-0182	V_p	$\rho\ (\mathrm{kgm^{-3}})$	$k_e\ (\mathrm{W(mK)^{-1}})$
5% M_p slurry	5.09%	980	0.578
10% M_p slurry	10.3%	971	0.556

5.1.3 Dynamic viscosity of DPNT06-0182 slurries

The rheological properties of DPNT06-0182 slurries were measured using a Kinexus rheometer from Malvern Instruments Ltd. This measured the dynamic viscosities vs. shear rates of DPNT06-0182 slurries at a given concentration but at different temperatures. For a 10% DPNT06-0182 slurry, the viscosities over the temperature range 15 - 40 °C were measured at 5°C intervals, and the results are show in Fig.5.3. For a given temperature, the viscosity presents a complicated non-Newtonian fluid feature. At low shear rate values, the fluid is shear thinning, but when the shear rate attains the value of ~50 s^{-1}, the viscosity gradually increases as the shear rate increases and presents a shear thickening feature. Note that the viscosity tends to decrease with an increase in temperature, and this is more evident at shear rate values above a value of ~50 s^{-1}.

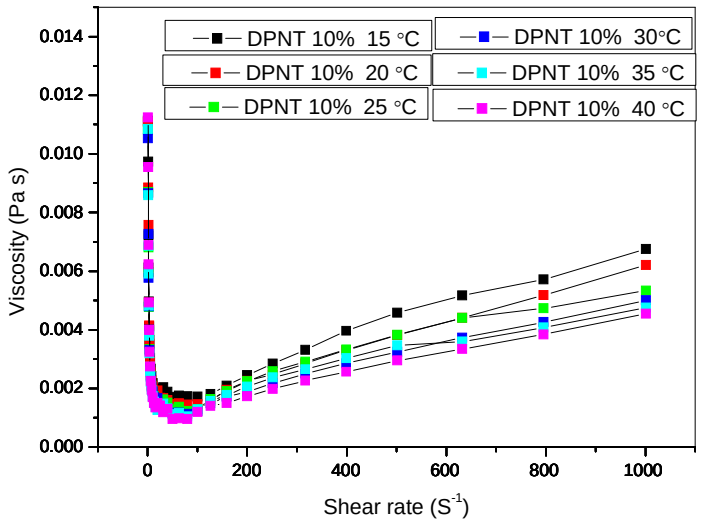

Figure 5.3: The viscosities of DPNT06-0182 10% slurry vs. shear rates

5.2 Heat transfer analysis of DPNT06-0182 slurries

The local bulk mean temperature of MPCS is a very important parameter for allowing the local heat transfer coefficient to be determined. However, the calculation of it is different from a single-phase fluid due to the existence of a melting phase change.

As demonstrated in Fig.5.2, the specific heat capacity value of DPNT06-0182 slurries changes with temperature; thus, it is convenient to describe the effect of phase change latent heat by an effective specific heat capacity. The effective specific heat capacity is defined as [89]:

$$c_{p,eff} = \frac{\int_{T_{in}}^{T_{bx}} c_{p,s} dT}{\int_{T_{in}}^{T_{bx}} dT} \tag{5.3}$$

The local bulk mean temperature of MPCM slurries can be directly calculated using Eq. (5.4), which has the same form as that for a single-phase fluid (Eq. (4.12)):

$$T_{bx} = T_{in} + \frac{Q_x}{\dot{m} c_{p,eff}} \tag{5.4}$$

A new equation can now be derived from Eqs. (5.3) and (5.4):

$$\int_{T_{in}}^{T_{bx}} c_{p,s} dT = \frac{Q_x}{\dot{m}} \tag{5.5}$$

The bulk mean temperature T_{bx} can then be solved from Eq. (5.5) by integration of the specific heat capacity of DPNT06-0182 slurry with temperature under the condition of the given heat flux and mass rate of flow.

In experiments, the heating flux was 3500 W. The flow rate was adjusted by changing the frequency of the pump, as a certain frequency corresponds to a certain power of the pump. For the same energy efficiency, *i.e*. for the

same power of the pump, it was observed in experiments that the flow rate of MPCS was slightly lower than that of water. Therefore, two cases are considered in the analysis that follows. Firstly, the heat transfer behavior is compared for DPNT slurries and water under the same frequency of the pump. It should be noted, however, that in previous studies of MPCS by other authors [84, 85], the measurement of local heat transfer coefficients of MPCS compared to water were performed at the same flow rates. Thus, the heat transfer behavior of DPNT slurries and water will also be compared for the same flow rate, although this means that the consumed power of the pump may be different in each case. This study was needed to allow the present measurements to be compared to those of MPCS behavior that have already been published, noting that some of the results published already can be somewhat incomplete and contradictory.

5.3 Results for a constant pump frequency

As stated above, the freezing temperature range of the DPNT microcapsules was found to be 18.74 - 33.97 °C. Thus, if the inlet temperature of fluid T_{in} , was below 18.74 °C, the PCMs within the microcapsules would be in a fully solid state. In order to investigate the melting heat transfer, as well as entire phase change behavior of MPCS, the inlet temperatures of 6 groups were all controlled below 18.74 °C by action of the chiller and the heat exchanger. The different flow rates were controlled by the frequency of the pump, so that different fluid temperatures within the heated test section could be obtained. Accordingly, different states could be produced experimentally: a full phase change (the PCMs of microcapsules

have all changed into liquid), a partial phase change (the PCMs have only partly changed into liquid) and no phase change (the PCMs remain solid).

5.3.1 Heat transfer coefficients

The measured data were collected by the IMP data logger at one-second intervals and were written into a file automatically. Six sets of data were obtained under six different pump frequencies (12 Hz, 15 Hz, 25 Hz, 35 Hz, 45 Hz and 55 Hz). In order to reduce the occasional errors, the average values of a series of measured data were recorded at each frequency in turn, and used for later analysis. The test materials were 10% DPNT06-0182 slurry, 5% DPNT06-082 slurry and water respectively. The flow rates were seen to be slightly different for the three fluids for the same pump frequency. In each group, the mean velocity of water is the highest and that of 10% DPNT06-082 slurry is the lowest, as shown in Table 5.2. Each data set consisted of:

- Fluid temperatures at 5 positions measured by thermocouples;
- 13 inside wall temperatures (derived in Eq. (4.11) from the measured outside wall temperatures);
- 13 calculated bulk mean temperatures;
- 12 corrected wall temperatures;
- 12 local heat transfer coefficients calculated by the measured wall temperatures, together with 12 corrected local heat transfer coefficients;
- The pressure drop across the length of the heated test section.

- Errors between measured and corrected wall temperatures for 10% DPNT06-0182 slurry.

Here, a correction method was proposed for calculation of wall temperatures of MPCS for two reasons. Firstly, there is not a proper non-Newtonian empirical correlation to predict the local wall temperations of non-single-phase fluid, and if a MPCS is processed as an approximate Newtonian fluid, the errors between the measured and predicted values are very large. Also for this reason the current empirical correlations cannot be applied. Secondly, the errors of wall temperatures are unavoidable as described in Chapter 4.

From Eq.(4.10), we can get:

$$T_{wi} = \frac{q_w}{h} + T_b \tag{5.6}$$

The errors of local wall temperatures ΔT_{wi} can be described:

$$\Delta T_{wi} = \frac{\partial T_{wi}}{\partial q_w}\Delta q_w + \frac{\partial T_{wi}}{\partial h}\Delta h \tag{5.7}$$

We assume that Δq_w has a functional relationship with the position of the test section under the same frequency of pump or the same flow rate. Δq_w of 12 measured points can be determined from the measured data of water by using empirical correlations. For a MPCS, an initial guess of the local heat transfer coefficient h_o is substituted in Eq. (5.7) to calculate ΔT_{wi}, so the corrected local wall temperatures may be obtained and the corrected heat transfer coefficient h_c can be calculated. If the corrected h_c is not equal to the original h_o, the corrected h_c is set as the new h_o and substituted in Eq.

(5.7) to continue the calculation iteratively, until the corrected h_c is equal to the last h_o . This method can be used to compare local heat transfer coefficients of a MPCS with water under the correction mode.

The results for temperatures, heat transfer coefficients and errors of wall temperatures are shown in Figs. 5.4 - 5.9 for the six different pump frequencies.

Table 5.2: Mean velocity u_m in ms^{-1} as a function of pump frequency

Pump frequency	12 Hz	15 Hz	25 Hz	35 Hz	45 Hz	55 Hz
10% DPNT slurry:	0.41	0.56	1.00	1.48	1.95	2.37
5% DPNT slurry:	0.44	0.57	1.04	1.52	1.99	2.41
Water	0.48	0.61	1.07	1.55	2.00	2.45

The results for the pump frequency of 12 Hz are shown in Fig. 5.4. Here, the overall flow rate is the lowest as seen in Table 2, and hence the fluid attains the highest temperatures. For 10% DPNT06-082 slurry, 5 measured temperatures of fluid at the centre line range from 18.55 – 39.84 °C, whereas the bulk mean temperatures range from 18.62 – 42.61 °C. Because the freezing temperature range of DPNT is 18.74 – 33.97 °C, the particulate PCMs at the inlet to the test section are in the solid state. Since the melting temperature range of DPNT06-082 slurry is 24.99 – 38.2 °C, it can be preliminarily concluded that the full phase change of PCMs in microcapsules from solid to liquid has been completed within the heating test section. As stated before, phase change latent heat is absorbed during travel through this test section. The fluid temperature of 10% DPNT06-082 slurry is a bit

higher than at 5%, which is in turn a little higher than water, as shown in Fig. 5.4(a). This is because the specific heat capacity of water is higher than DPNT06-082 slurries at locations outside the melting phase change stage. Even if PCMs within the microcapsules need to absorb latent heat within this phase change stage (which results in an increase of the specific heat capacity), the result is not enough to make the temperature of DPNT06-082 slurries lower than that of water. In addition, the mean velocity of 10% DPNT06-082 slurry is the lowest and viscosity is the highest, so the local wall temperatures of 10% DPNT06-082 slurry are also the highest compared the 5% DPNT06-082 slurry and water. Nevertheless, for itself, the trend of wall temperatures increasing decreases during the melting stage of PCMs.

From Eq. (4.10), the heat transfer coefficients were calculated for the three fluids. The direct results show that the local heat transfer coefficients of 10% DPNT06-082 slurry are the lowest and are the highest for water, as shown in Fig. 5.4(c). The correction method was used to correct the wall temperatures of slurries and also calculate the corrected heat transfer coefficients. As seen in Fig. 5.4(e), the errors of wall temperatures at the last two points for 10% DPNT06-0182 slurry were relatively bigger, which subsequently caused the measured heat transfer coefficients of these two points be large. The local corrected wall temperatures tended to be higher than the measured temperatures, so that the corresponding heat transfer coefficients were lower than the direct results from measurements. However, the results also show that the heat transfer coefficient of 10% DPNT06-0182 slurry is the lowest of the three materials, and that of water is the highest, as shown in Fig. 5.4(d). This indicates that during the fully-melting phase change stage, a large

temperature difference between the inlet and outlet exists in the presence of a low flow rate. At the same time, the local wall temperatures present when MPCS is used are higher than those obtained with water, and hence the heat transfer coefficient of 10% DPNT06-0182 slurry is the lowest of the three materials. However, during this stage, the highest amount of latent heat is stored by the 10% DPNT06-0182 slurry, because the PCMs within microcapsules melt and absorb the available phase change latent heat.

At the pump frequency of 15 Hz, for 10% DPNT slurry, the bulk mean temperature of the outlet was 36.09 °C, as shown in Fig. 5.5. The majority of the PCM of microcapsules were thus melted, and exhibited the similar results to those recorded at 12 Hz, although the time at which the phase change appeared was different for the two different flow rates. This also resulted in slight differences in the heat transfer coefficient data.

At pump frequencies of 25 Hz and 35 Hz, for 10% DPNT slurry, the bulk mean temperature of outlet was 29.39 °C and 25.92 °C respectively. In these two cases, the results for which are shown in Figs. 5.6 and 5.7, only a partial phase change of the PCM is present. In the front part of the test section, the heat transfer coefficients of DPNT06-0182 slurries are lower than water, but further along the test section the heat transfer coefficients of 10% DPNT06-0182 slurry are higher than those of water (as are those of 5% DPNT06-0182 slurry). This indicates that the wall temperatures of MPCS increase more slowly than water in the latter part of the test section due to these phase change effects.

At pump frequencies of 45 Hz and 55 Hz, shown in Figs. 5.8 and 5.9 respectively, the flow rates were higher, so that for 10% DPNT slurry, the bulk

mean temperature at the outlet were 24.15 °C and 23.15 °C respectively. Since the melting temperature range of PCMs is 24.99 - 38.20 °C, this means that during the whole heating test section, the PCMs in microcapsules stayed in the solid state, and no phase change occurred. The specific heat capacity of DPNT06-0182 slurries are lower than water, so that the bulk mean temperatures and the measured fluid temperatures of DPNT06-0182 slurries were higher than for water; the measured and corrected wall temperatures of DPNT06-0182 slurries were also higher than for water, but the difference was smaller than that between the fluid temperatures of the slurries and water. The results show that under these high flow rates, either the measured or the corrected heat transfer coefficients of 10% DPNT06-0182 slurry are the highest, except at the first heating measured point. Note that the heat transfer coefficients of some measured points of 5% DPNT06-0182 slurry were higher than water, although some are lower at 45 Hz. Also, the heat transfer coefficients of most measured points of 5% DPNT06-0182 slurry were higher than those of water at a pump frequency of 55 Hz. Therefore, the suspension slurry can increase the local heat transfer coefficients in the situation of higher flow rates and no phase change happened while it compares with water.

5.3.2 Pressure drop

The measured pressure drops are also presented in Fig. (5.10). With an increase in flow rate, the pressure drops of both slurries and water increased. For the lowest flow rate (12 Hz pump frequency), there were big differences in flow rates between the three types of fluid. Therefore, the pressure drop of

10% DPNT06-0182 slurry was the lowest and water the highest, because of the lower flow rate of the 10% DPNT06-0182 slurry. At a pump frequency of 15 Hz, the pressure drops of MPCS increased, making the difference between them decrease. At higher flow rates, the pressure drops seen for the slurries increased much more than for water, so that again 10% DPNT06-0182 slurry had the highest values, those of 5% DPNT06-0182 slurry were lower, and water had the lowest values of all .

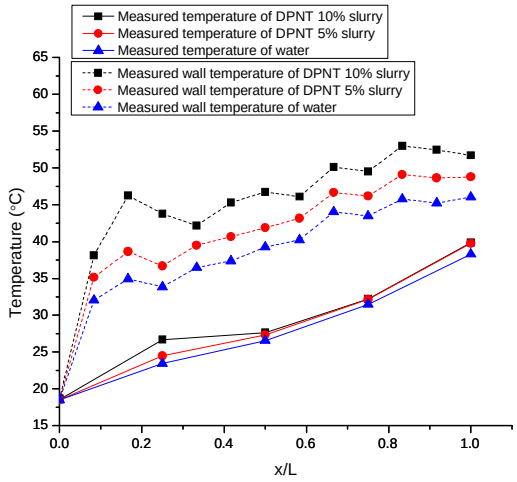

(a)

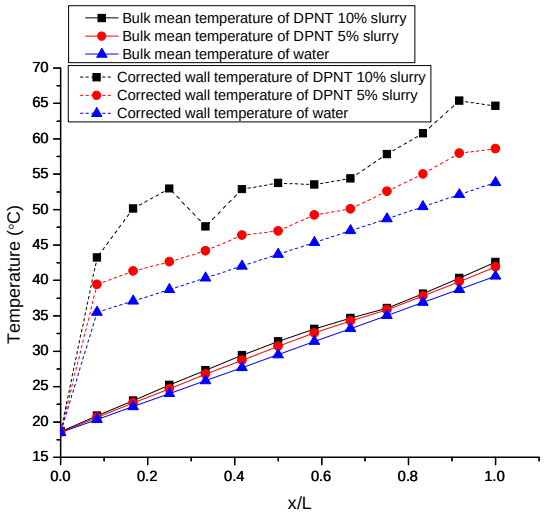

(b)

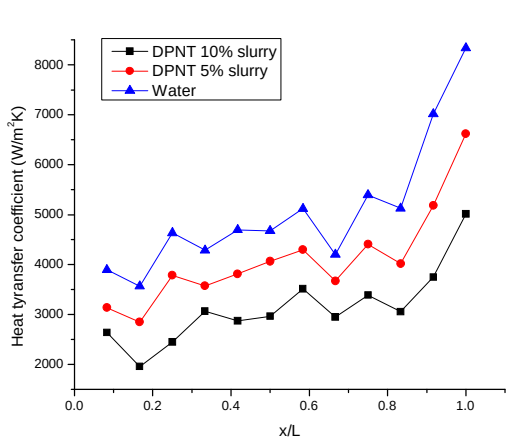

(c)

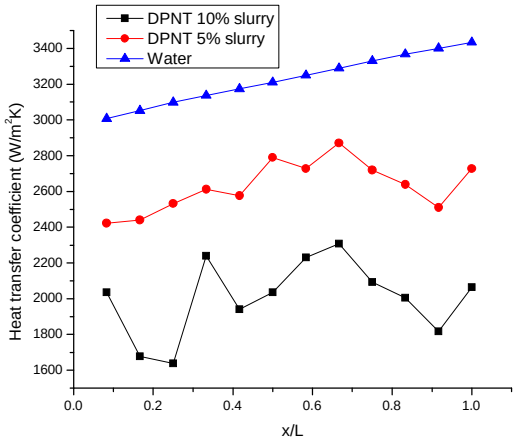

(d)

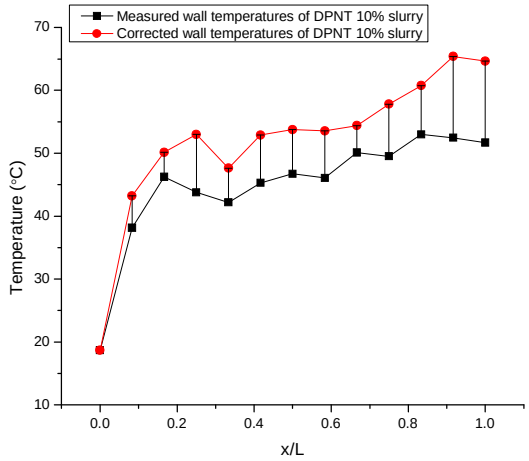

(e)

Figure 5.4: Results for a pump frequency of 12 Hz. Shown are (a) measured fluid temperatures and wall temperatures, (b) bulk mean temperatures and corrected wall temperatures, (c) measured local heat transfer coefficients, (d) corrected local heat transfer coefficients, (e) errors between measured and corrected wall temperatures.

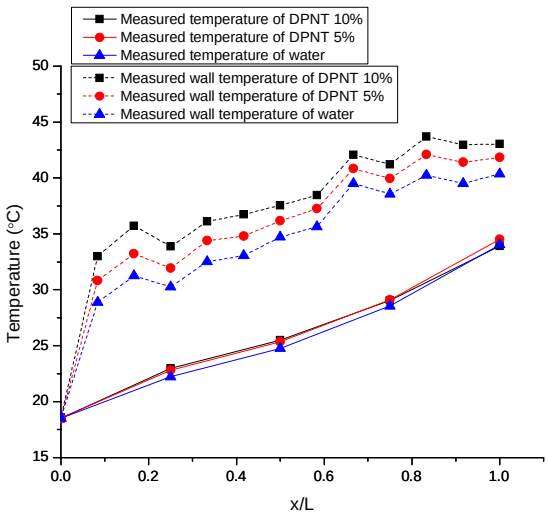

(a)

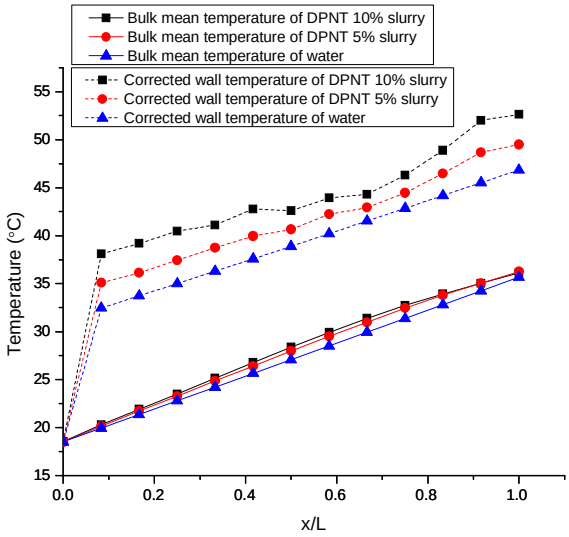

(b)

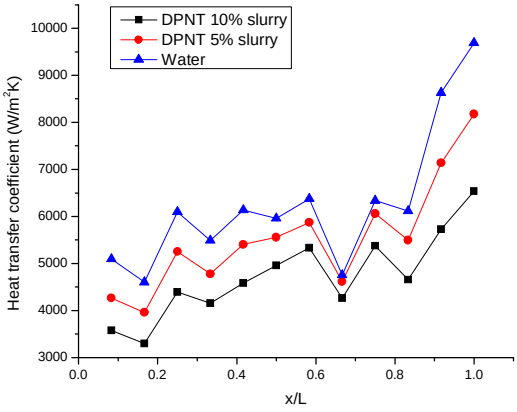

(c)

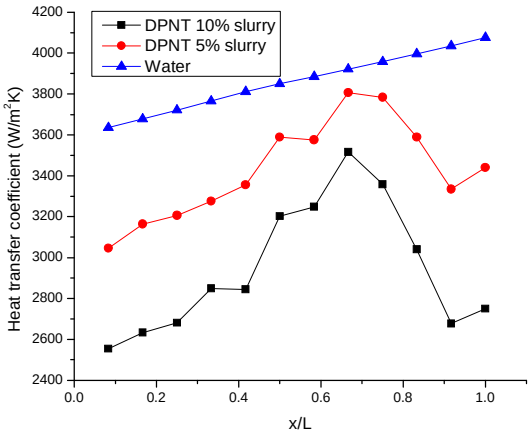

(d)

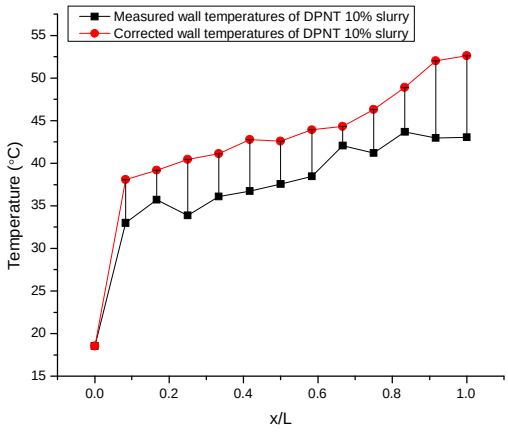

(e)

Figure 5.5: As Fig. 5.4, but for a pump frequency of 15 Hz.

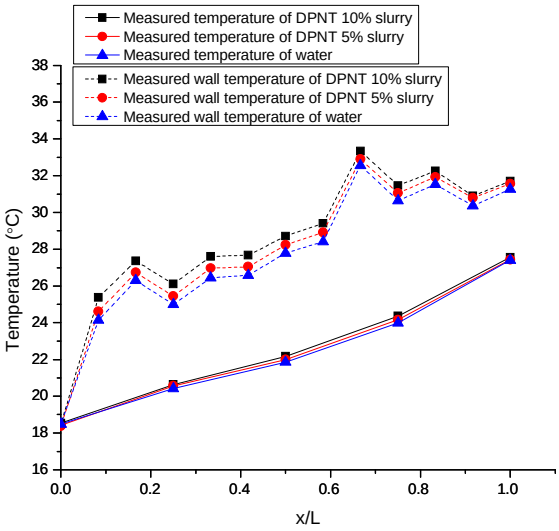
Measured temperature of DPNT 10% slurry
Measured temperature of DPNT 5% slurry
Measured temperature of water
Measured wall temperature of DPNT 10% slurry
Measured wall temperature of DPNT 5% slurry
Measured wall temperature of water
Temperature (°C)
x/L

(a)

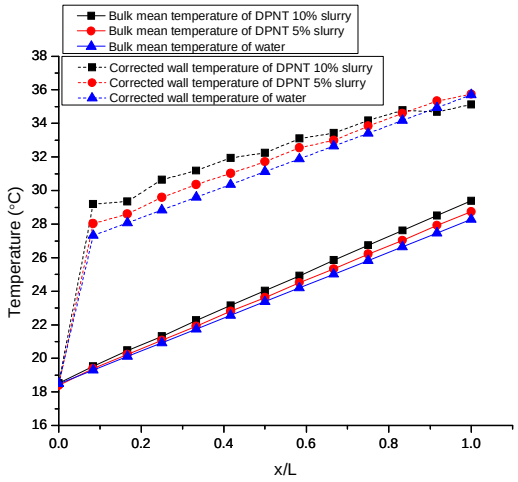
Bulk mean temperature of DPNT 10% slurry
Bulk mean temperature of DPNT 5% slurry
Bulk mean temperature of water
Corrected wall temperature of DPNT 10% slurry
Corrected wall temperature of DPNT 5% slurry
Corrected wall temperature of water
Temperature (°C)
x/L

(b)

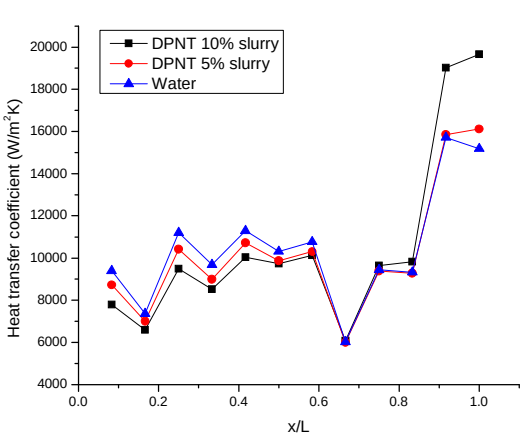
DPNT 10% slurry
DPNT 5% slurry
Water
Heat transfer coefficient (W/m²K)
x/L

(c)

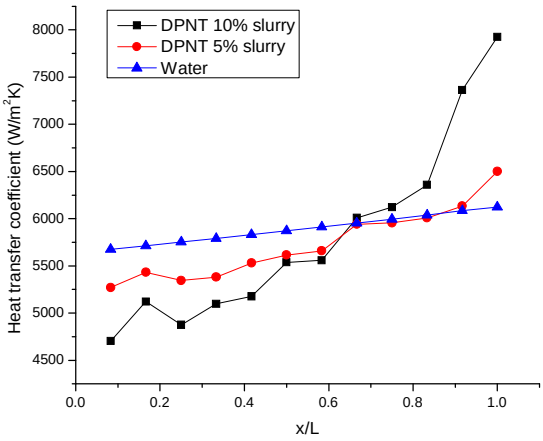
DPNT 10% slurry
DPNT 5% slurry
Water
Heat transfer coefficient (W/m²K)
x/L

(d)

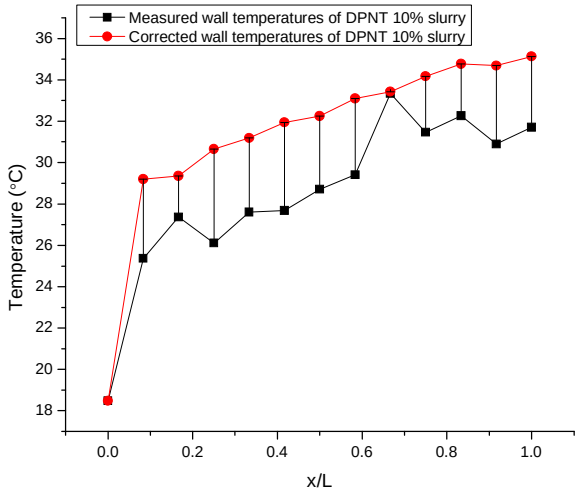

(e)

Figure 5.6: As Fig. 5.4, but for a pump frequency of 25 Hz.

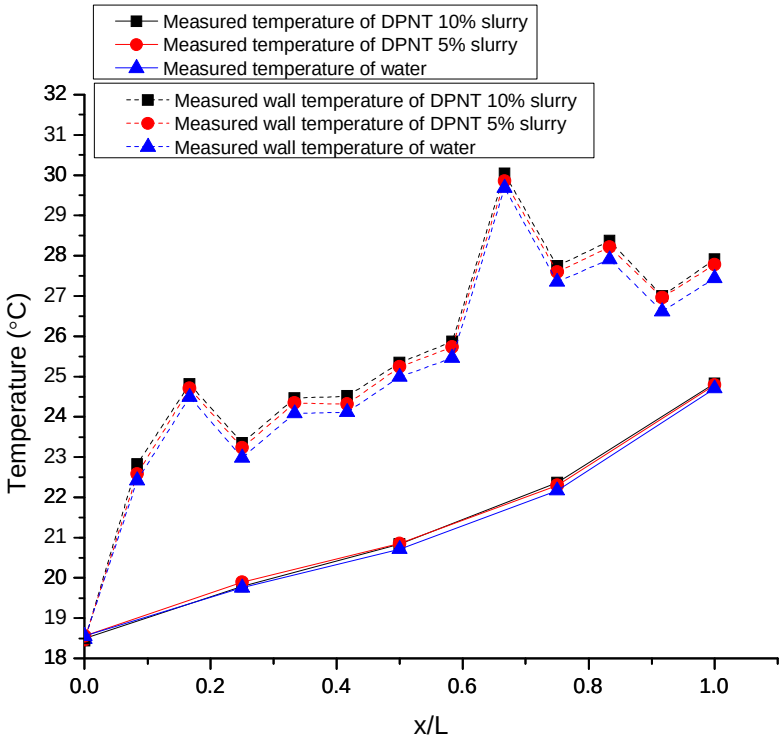

(a)

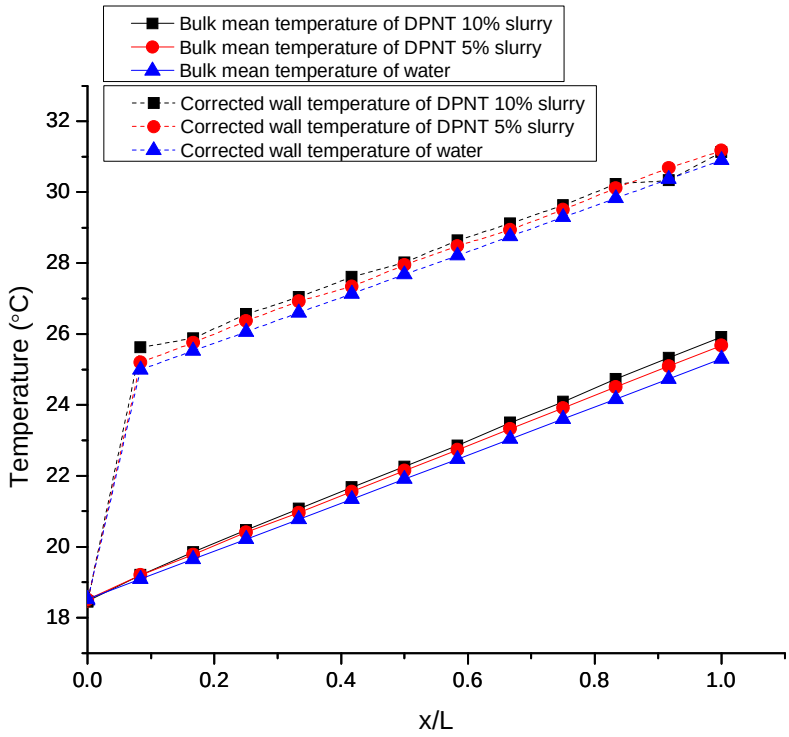
Bulk mean temperature of DPNT 10% slurry
Bulk mean temperature of DPNT 5% slurry
Bulk mean temperature of water
Corrected wall temperature of DPNT 10% slurry
Corrected wall temperature of DPNT 5% slurry
Corrected wall temperature of water
Temperature (°C)
x/L

(b)

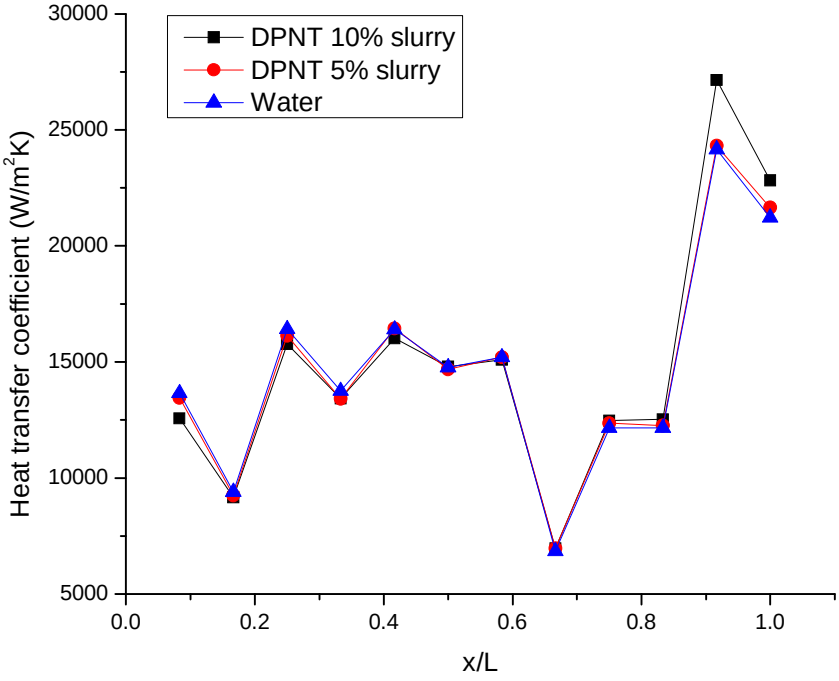
DPNT 10% slurry
DPNT 5% slurry
Water
Heat transfer coefficient (W/m²K)
x/L

(c)

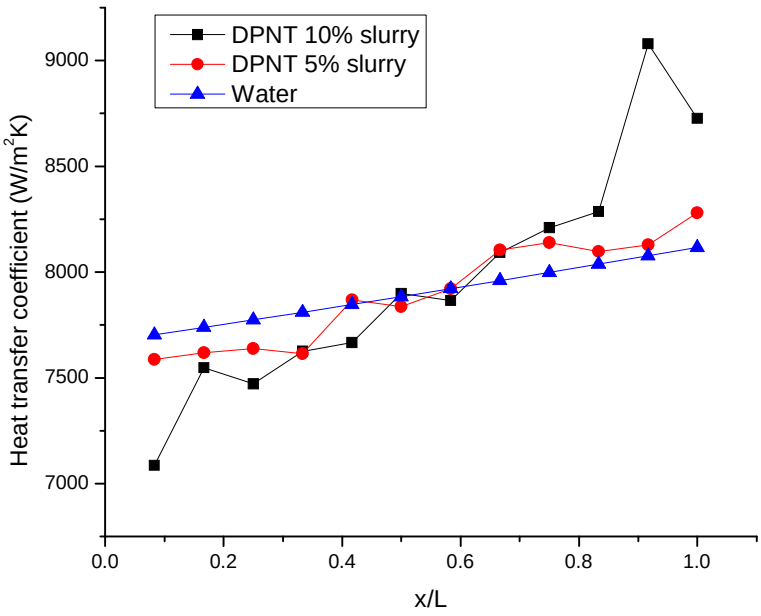

(d)

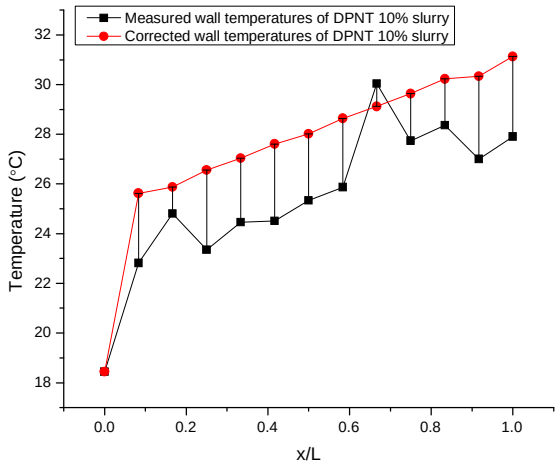

(e)

Figure 5.7: As Fig. 5.4, but for a pump frequency of 35 Hz.

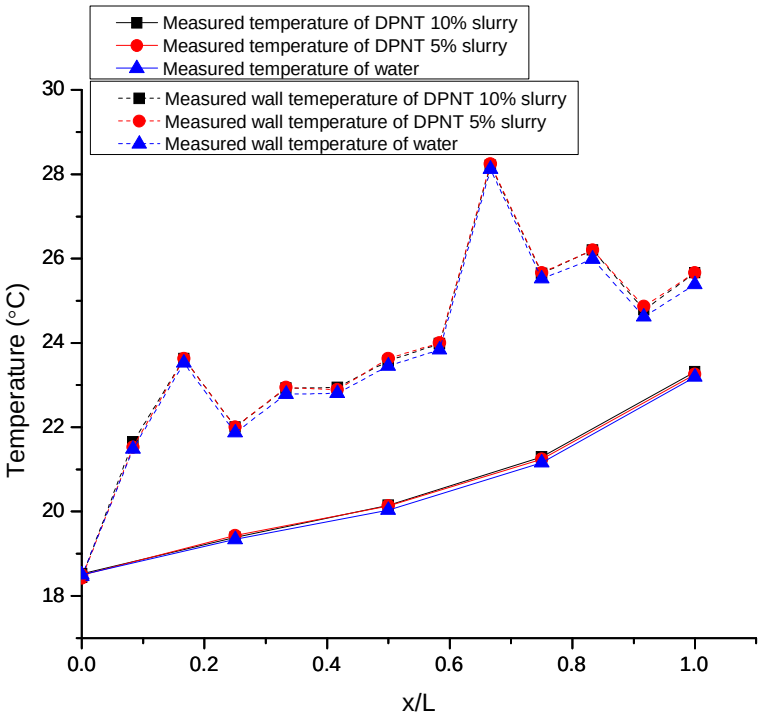
Measured temperature of DPNT 10% slurry
Measured temperature of DPNT 5% slurry
Measured temperature of water
Measured wall temeperature of DPNT 10% slurry
Measured wall temperature of DPNT 5% slurry
Measured wall temperature of water
Temperature (°C)
x/L
30
28
26
24
22
20
18
0.0
0.2
0.4
0.6
0.8
1.0

(a)

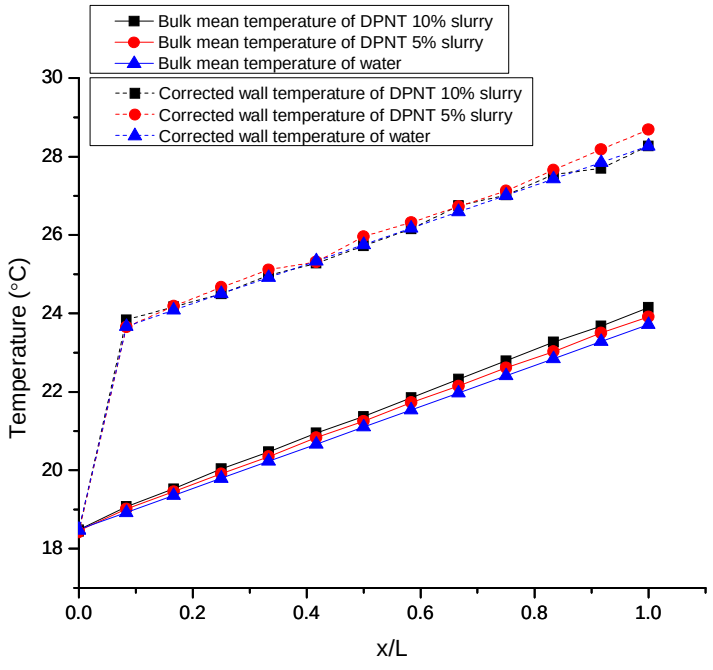
Bulk mean temperature of DPNT 10% slurry
Bulk mean temperature of DPNT 5% slurry
Bulk mean temperature of water
Corrected wall temperature of DPNT 10% slurry
Corrected wall temperature of DPNT 5% slurry
Corrected wall temperature of water
Temperature (°C)
x/L
30
28
26
24
22
20
18
0.0
0.2
0.4
0.6
0.8
1.0

(b)

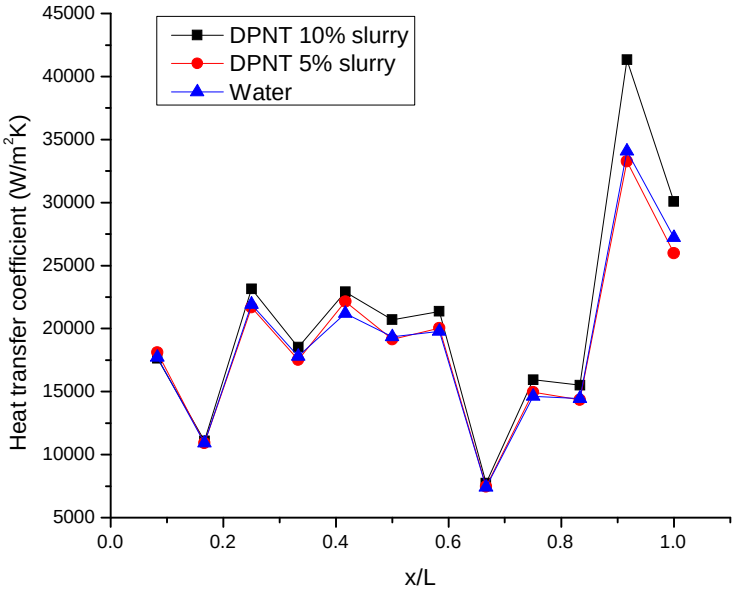
DPNT 10% slurry
DPNT 5% slurry
Water
Heat transfer coefficient (W/m²K)
x/L
45000
40000
35000
30000
25000
20000
15000
10000
5000
0.0
0.2
0.4
0.6
0.8
1.0

(c)

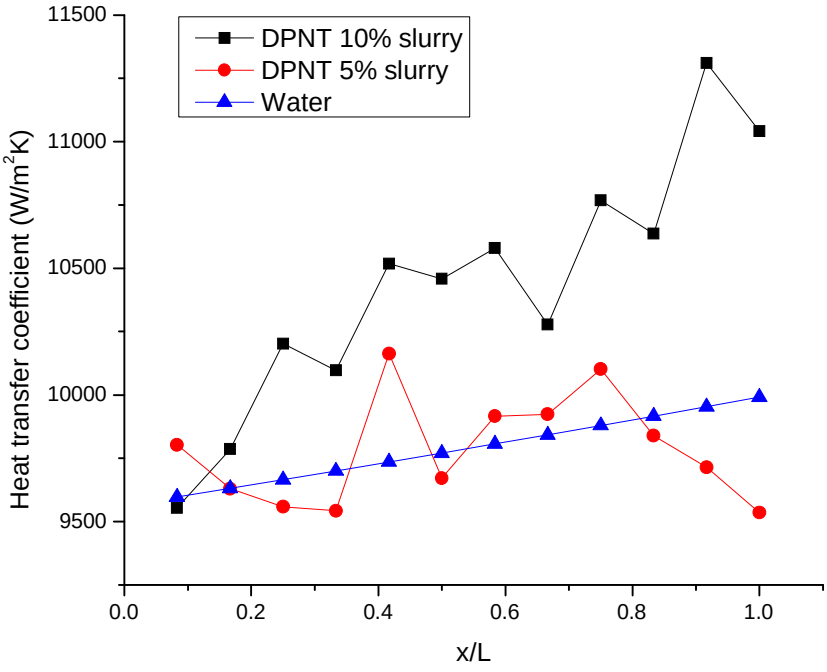
DPNT 10% slurry
DPNT 5% slurry
Water
Heat transfer coefficient (W/m²K)
x/L
11500
11000
10500
10000
9500
0.0
0.2
0.4
0.6
0.8
1.0

(d)

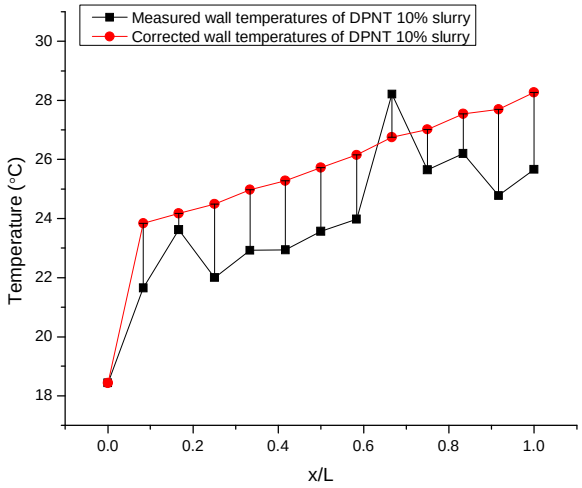

(e)

Figure 5.8: As Fig. 5.4, but for a pump frequency of 45 Hz.

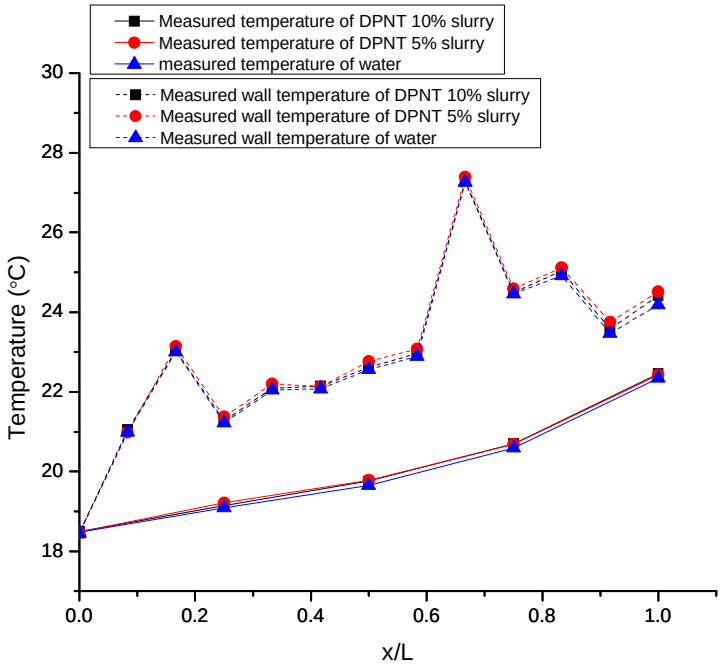

(a)

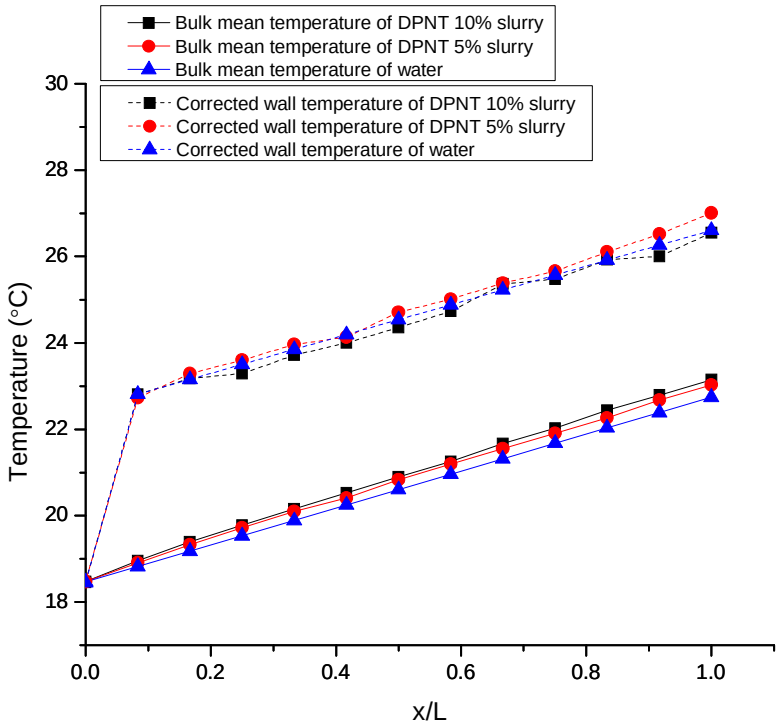
Bulk mean temperature of DPNT 10% slurry
Bulk mean temperature of DPNT 5% slurry
Bulk mean temperature of water
Corrected wall temperature of DPNT 10% slurry
Corrected wall temperature of DPNT 5% slurry
Corrected wall temperature of water
Temperature (°C)
x/L

(b)

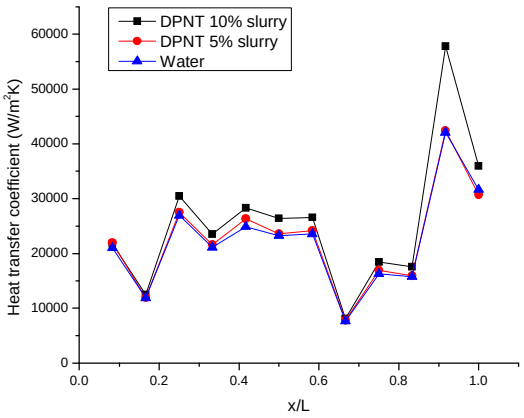
DPNT 10% slurry
DPNT 5% slurry
Water
Heat transfer coefficient (W/m²K)
x/L

(c)

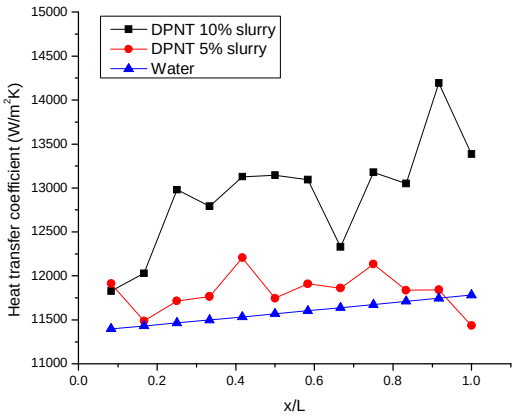
DPNT 10% slurry
DPNT 5% slurry
Water
Heat transfer coefficient (W/m²K)
x/L

(d)

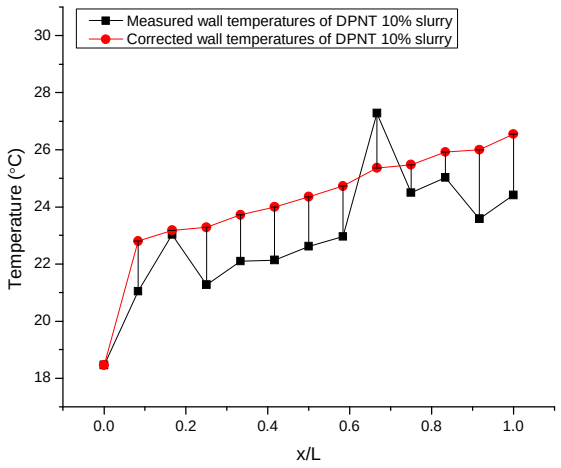

(e)

Figure 5.9: As Fig. 5.4, but for a pump frequency of 55 Hz.

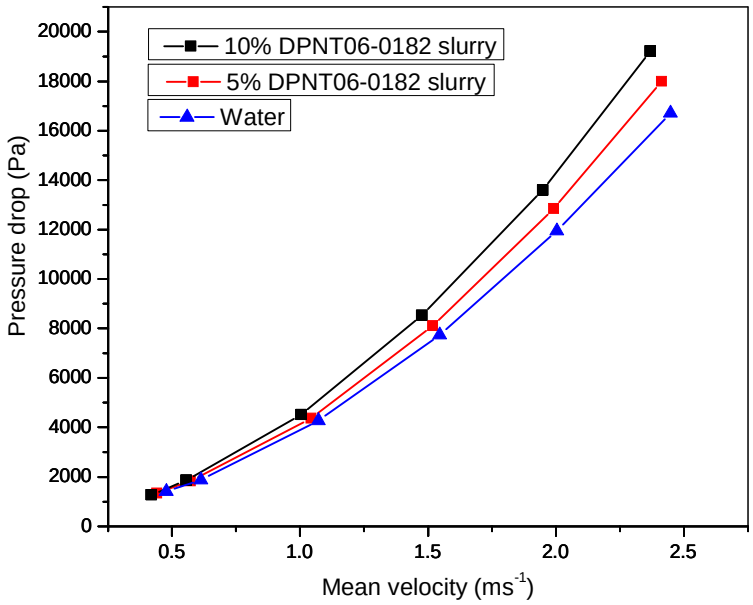

Figure 5.10: The relationship between pressure drop and mean velocity for DPNT06-0182 slurries and water

5.4 Results for a constant flow rate

Experiments were also performed for DPNT06-0182 slurries and water under another condition, *i.e*. for the constant flow rate. This was performed at

three different mean velocity values (u_m) of 0.44 ms^{-1}, 1.51 ms^{-1} and 2.41 ms^{-1}. For these studies, a Gnielinski correlation [123] [85] was used to calculate theoretical local Nusselt numbers, local heat transfer coefficients and corrected wall temperatures. This correlation is described by Eq. (5.8):

$$Nu_D = \frac{(f_D/8)(\mathrm{Re}_D - 10^3)\mathrm{Pr}}{1 + 12.7(f_D/8)^{1/2}\left(\mathrm{Pr}^{2/3} - 1\right)} \tag{5.8}$$

It is applied in the range $0.5 < \mathrm{Pr} < 2000$ and $3000 < \mathrm{Re}_D < 5 \cdot 10^6$.

The properties of the Gnielinski equation are dependent upon the local bulk mean temperatures, so it excludes the influence of the measured wall temperatures. The test and calculated results for three different flow rates are demonstrated in Figs. 5.11 -5.13. At a the slowest flow rate, *i.e*. a mean velocity $u_m \approx$ 0.44 ms^{-1}, the phase change within the microcapsules was complete for the slurries during the test section. There is a little difference between the bulk mean temperature of slurries and water, and temperatures of 10% DPNT slurry at the last few points were lower than water due to the increase of specific heat capacity while phase change was occurring. The measured and corrected wall temperatures of 10% DPNT06 0182 slurry are the highest of the three fluids; those of 5% DPNT06 0182 slurry were slightly lower and those of water the lowest. Thus, the local heat transfer coefficients of water (either measured or corrected) were the highest, and those of 10% DPNT06-0182 slurry the lowest. For pressure drop, the measured value for 10% DPNT06-0182 slurry was the lowest and water the highest.

When the mean velocity was changed to $u_m \approx$ 1.51 ms^{-1}, a small amount of phase change of PCMs in microcapsules was observed. The results indicate

that, apart from some isolated values, the heat transfer coefficients of water were the highest. The pressure drop of 5% DPNT06-0182 slurry was the lowest and 10% DPNT06-0182 slurry the highest.

At the highest mean velocity u_m of 2.41 ms^{-1}, no phase change occurred within the PCM microcapsules. Both measured and corrected results indicate that both the heat transfer coefficients and the pressure drop were at the highest values for the 10% DPNT06-0182 slurry.

In summary, from the point of view of flow rates that influence the phase change, the conclusions for the cases of full phase change and no phase change are basically the same as the conditions present in Section 5.3, which described experiments performed for different frequencies of the pump.

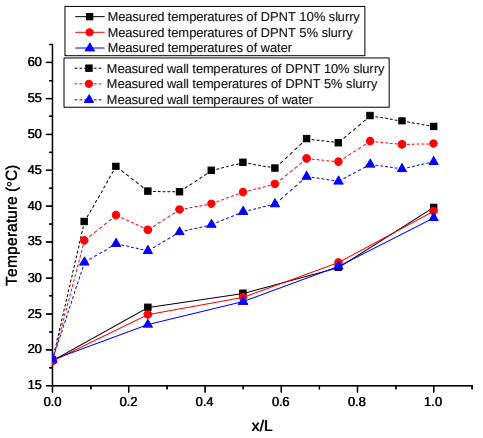

(a)

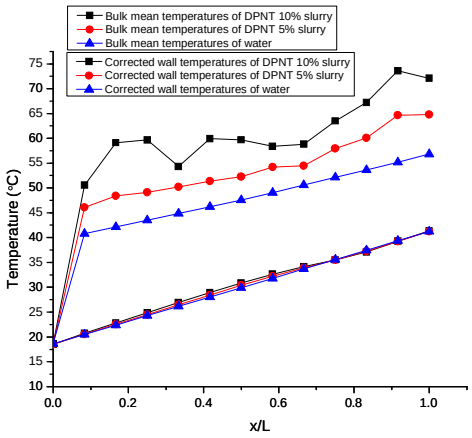

(b)

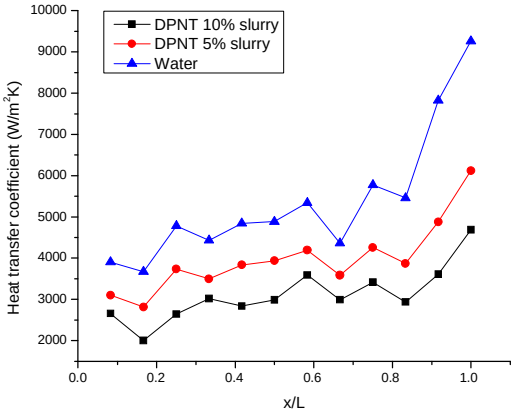

(c)

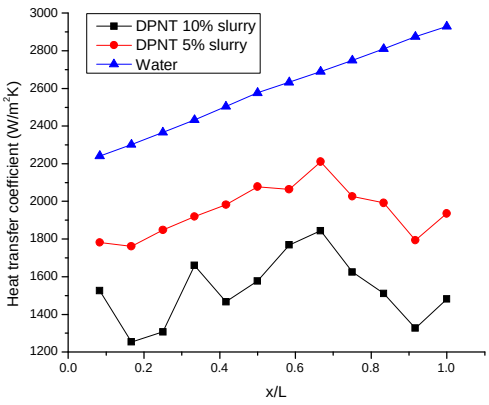

(d)

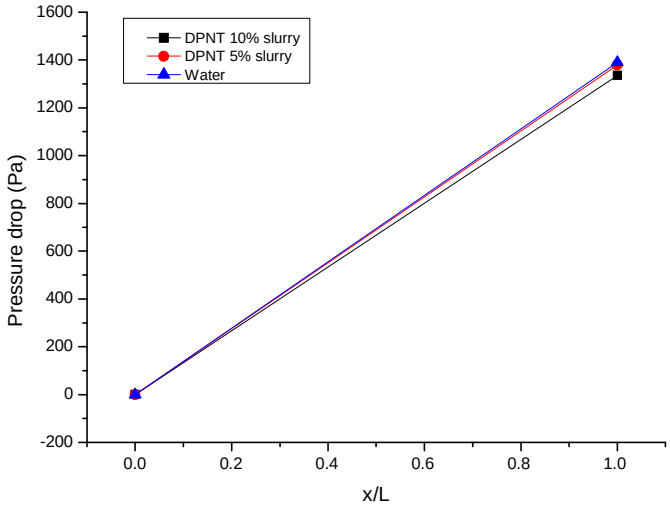

(e)

Figure 5.11: Results for $u_m \approx 0.44$ ms^{-1}. Shown are (a) Measured fluid temperatures and wall temperatures, (b) bulk mean temperatures and corrected wall temperatures, (c) measured local heat transfer coefficients, (d) corrected local heat transfer coefficients and (e) pressure drops.

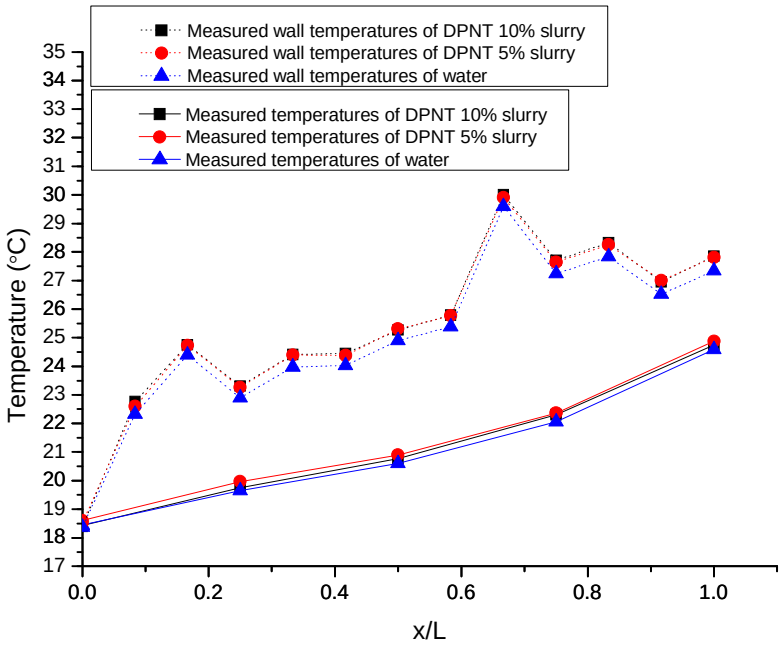

(a)

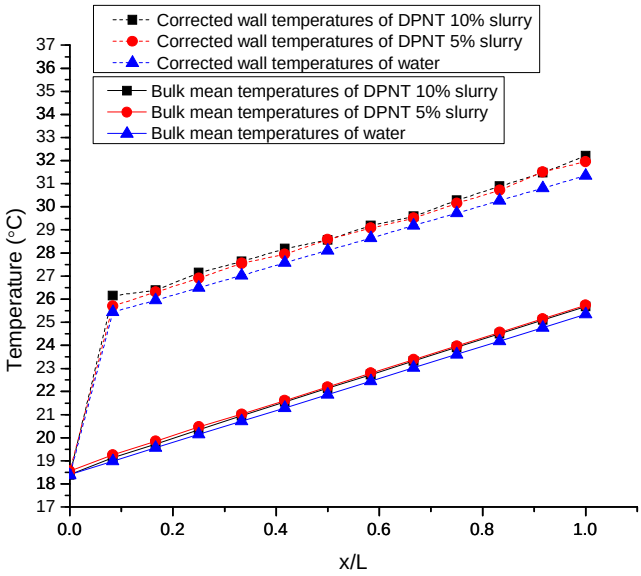

(b)

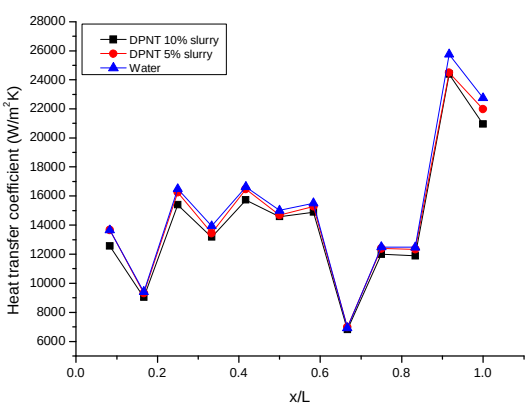

(c)

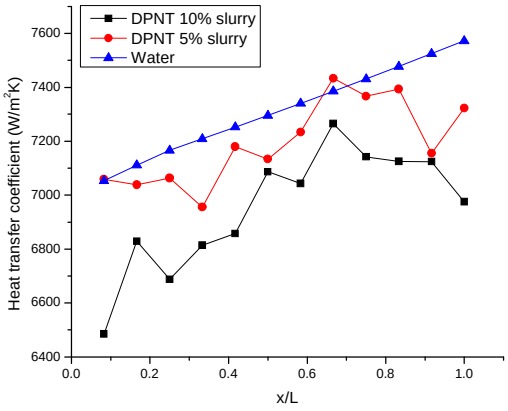

(d)

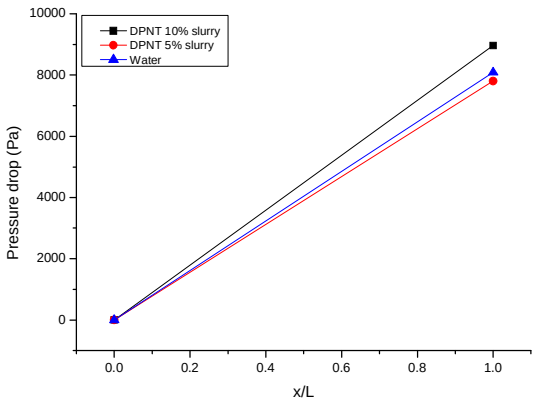

(e)

Figure 5.12: As Fig. 5.11, but for a mean velocity $u_m \approx 1.51\ ms^{-1}$.

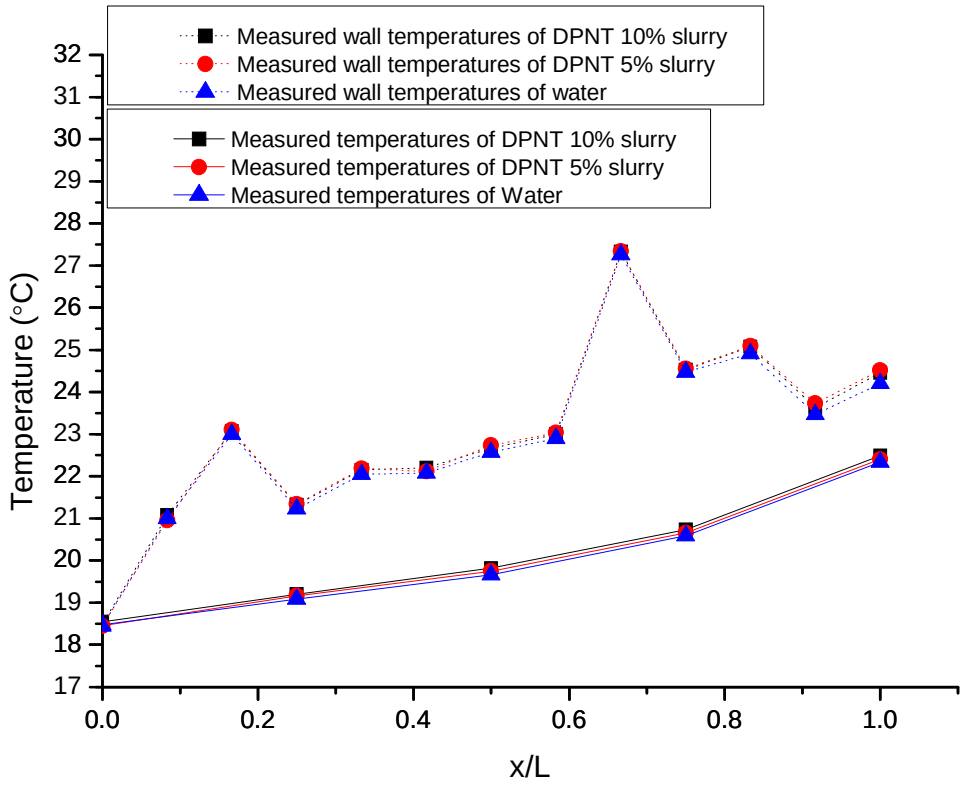
Measured wall temperatures of DPNT 10% slurry
Measured wall temperatures of DPNT 5% slurry
Measured wall temperatures of water
Measured temperatures of DPNT 10% slurry
Measured temperatures of DPNT 5% slurry
Measured temperatures of Water
Temperature (°C)
x/L

(a)

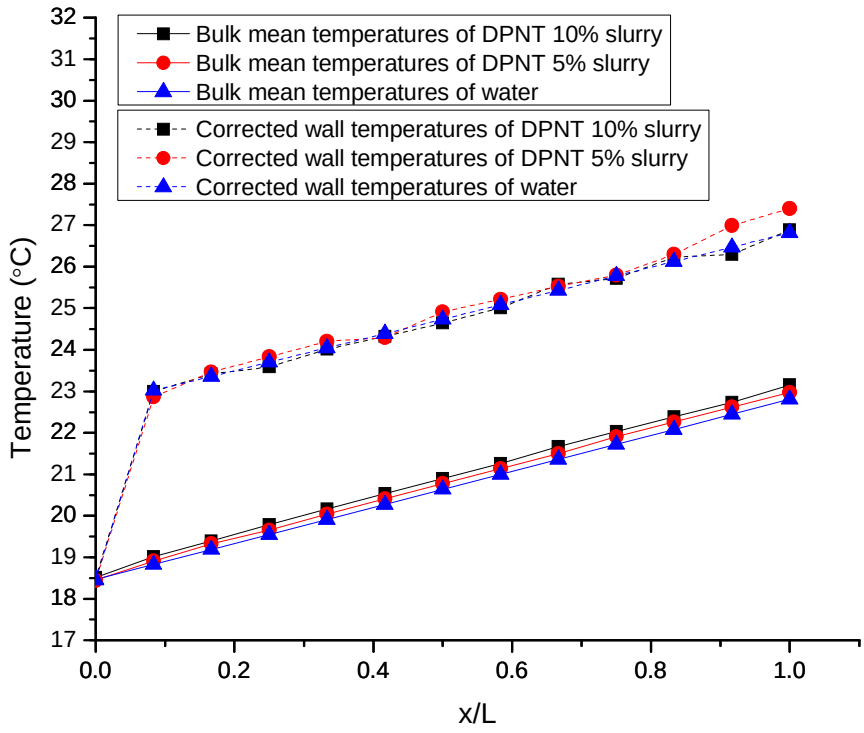
Bulk mean temperatures of DPNT 10% slurry
Bulk mean temperatures of DPNT 5% slurry
Bulk mean temperatures of water
Corrected wall temperatures of DPNT 10% slurry
Corrected wall temperatures of DPNT 5% slurry
Corrected wall temperatures of water
Temperature (°C)
x/L

(b)

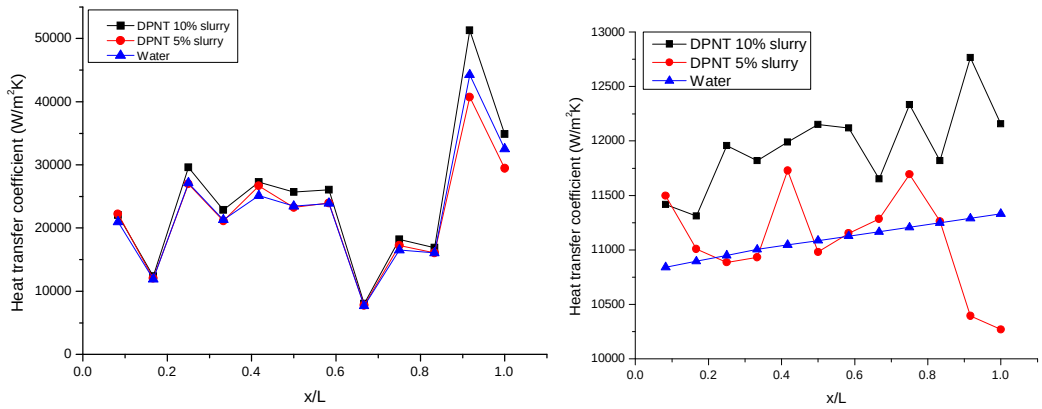

(c) (d)

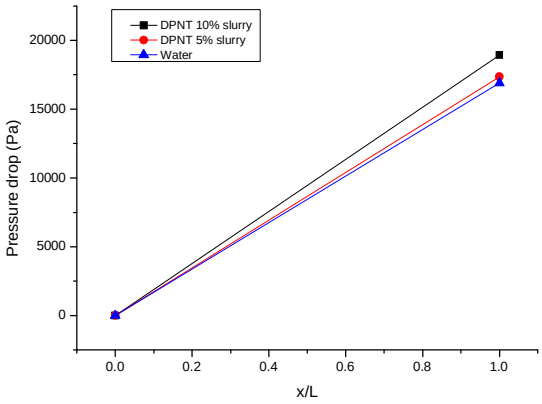

(e)

Figure 5.13: As Fig. 5.11, but for a mean velocity $u_m \approx 2.41$ *ms*$^{-1}$.

5.5 Conclusions

The experimental results have been shown that the flow rate is a key factor in determining the heat transfer coefficients under conditions of constant heating power. A full phase change needs a lower flow rate, which will also result in high wall temperatures. Comparisons of MPCS with a high mass fraction to both water and a slurry with a lower mass fraction indicates that the heat transfer coefficient of a high mass fraction MPCS is the lowest, but that its pressure drop is also the lowest, and importantly the most heat energy is stored during the heating test section.

The situation is different for high flow rate conditions. Since no phase

change occurs, the bulk mean temperatures of MPCS are higher than that of water under the same heating flux, due to the lower specific heat capacities of MPCS. Also, the corresponding wall temperatures of MPCS increase less than water in relative terms, so that the local heat transfer coefficients of MPCS with a high mass fraction are bigger than both MPCS with a low mass fraction and water. However, the pressure drop of MPCS with a higher mass fraction is the largest. Note that it is possible to control the flow rate so as to cause partial phase changes within the MPCS.

The Petukhov and Gnielinski correlations have both been used to correct the errors of measured wall temperatures. The corrected heat transfer coefficients agree with the conclusions of the above analytical experimental results. Nevertheless, there is a limitation, in that the correction method relies on errors analysis and theories of Newtonian fluids. If the relationship between shear stress (or shear rate) and viscosity is introduced into the heat transfer analysis, the non-Newtonian characteristics of MPCS need to be considered. This will be discussed in Chapter 6.

Chapter 6

A theoretical analysis of the behavior of DPNT06-0182 particles and slurries in a pipe under constant heat flux

Summary

The melting behaviour of differently-sized micro-particles in a heat transfer pipe flow is analysed by using the two-phase melting model of a sphere developed earlier in Chapter 3. The boundary conditions of a single particle are constructed based on the heat flux, flow rate and position of the particle in fluid. The melting time and temperature evolution of liquid-solid two phase within differently-sized particles are calculated. The results are seen to agree with the group melting behaviour of MPCM in a heat transfer pipe flow, as observed via the local bulk mean temperature. In addition, the non-Newtonian fluid characteristics of a 10% DPNT06-0182 slurry are analysed in detail, including factors such as the shear rate of the wall, the generalized Reynolds number, and velocity profiles under different flow rates.

6.1 Background and reasons for this study

In Chapter 5, the judgment as to whether or not a phase change was complete within the test section was based on whether the local bulk mean temperature attained the highest melting temperature. This was because the bulk mean temperature depends on the effective specific heat capacity,

which itself reflects both sensible heat and latent heat of fusion throughout the test section. When the local bulk mean temperature is greater than the highest melting temperature of the MPCM used, the specific heat capacity value used in the conservation of energy equation for calculation of the next local bulk mean temperature will no longer represent the effect of latent heat, and will basically stay constant. This means that, from the point of energy conservation, the situation in which the melting phase change is complete is when the local bulk mean temperature equals the highest melting temperature. The melting temperature range of DPNT06-0182 particles is 24.99 – 38.2 °C. Chapter 5 described the results of 10% DPNT06-0182 slurry from three flow rates: u_m = 0.42 ms^{-1}, u_m = 0.56 ms^{-1} and u_m = 1.00 ms^{-1} involving phase change. The corresponding time for MPCM particles to pass through the test section was 5.73 s, 4.32 s and 2.39 s respectively if we assume that the particles pass through the test section at the mean rate. Over this range, maybe complete and partial phase changes for 10% DPNT06-0182 particles occurred. For a value of u_m = 0.42 ms^{-1}, the melting of PCM of particles starts from the position given by x/L ≈ 0.25, and all PCM of particles change into liquid at x/L ≈ 0.83, according to the evidence obtained from local bulk mean temperatures; the time to complete the entire phase change is 3.34 s at this mean rate. For $u_m = 0.56$ ms^{-1}, the phase change starts from x/L ≈ 0.33, but at locations up to the outlet of the test section, the local bulk mean temperature is 36.1 °C. This indicates that the majority of the PCM in the particles has melted, and only a small fraction remains in the solid state - the phase change time here is 2.88 s at the mean rate $u_m = 0.56$ ms^{-1}. For $u_m = 1.00$ ms^{-1}, the phase change starts from x/L ≈

0.58, and from there until the outlet of the test section the local bulk mean temperature is 29.4 °C. This means that only a small quantity of PCM within the particles melts, and the phase change time is 0.99s at the mean rate $u_m = 1.00$ ms^{-1}. The above analysis is based on the whole effect of all particles and the conservation of energy.

Furthermore, the location where the bulk mean temperature of slurry equals the smallest melting temperature of MPCM (measured by DSC) can be defined as the position at which melting starts; another location, where the bulk mean temperature equals the highest melting temperature, can similarly be defined as the melting end position. When particles reach the melting start position, a small proportion of PCM within particles which are close to the wall will start to melt; more and more PCM within other particles will then also start to melt as they flow to the new locations where the bulk mean temperature increases. Eventually, the PCM within all particles changes into liquid at the melting end position. This is shown schematically in Fig.6.1.

The above analysis of the melting range within the test section also reflects the observed group behavior. Note that, as described in Chapters 2 and 3, the phase change time varies with particle size, even under the same boundary conditions. However, as we use the melting model of a sphere to describe the melting characteristics of a single particle in a heat transfer pipe fow, it is necessary to build a relationship between the boundary conditions of a particle, the heat flux, the flow rate and the position within the test section. This is the purpose of this Chapter.

At a particular axial location within the test section, the temperature of the

fluid will differ along the radial direction. The temperature of the fluid closest to the wall will be higher than that of the central fluid. However, it is difficult to judge the accurate radial position of a single particle at a certain time due to randomness of the molecular Brownian movement of particles in a laminar fluid or eddy diffusivity of a turbulent fluid. For this reason, some assumptions are proposed to allow the analysis to proceed:

- Any size of particle within the slurry has the same opportunity to start melting from the melting start position;
- The axial position of a particle changes with flow of the slurry, but the radial position remains constant under conditions of forced convection;
- The shell boundary temperature of particles increases with an increase of the bulk mean temperature.
- The solid PCM within a particle has a uniform temperature while the shell boundary temperature just arrives at the smallest melting temperature.

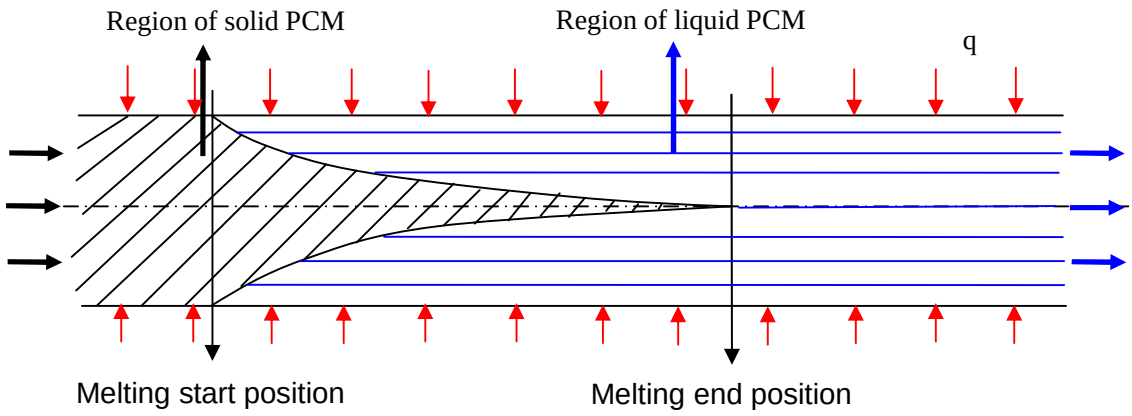

Figure 6.1: Phase change of PCM in a heated pipe

In this Chapter, the two-phase melting model of a single particle (which

was described earlier in Chapter 3) will be used to evaluate the melting behaviour of differently-sized particles, as they pass through a pipe, under the influence of a uniform heat flux. The Chapter will also investigate the fluid characteristics of the slurry containing these particles.

6.2 The melting behaviour of DPNT06-0182 particles in a heat transfer fluid

The starting point in the analysis is to identify the initial melting temperature of a liquid-solid interface for a single particle. The core PCM within DPNT06-0182 microcapsules is made of Paraffin wax, which consists of a mixture of chains of alkanes (C_nH_{2n+2}). Generally, both the melting point and latent heat of fusion increase with chain length. Some selected paraffins are shown in Table 6.1 along with their melting point and latent heat of fusion [3]. As seen in Fig.5.1, the peak melting point of DPNT06-0182 particles is 35.58 °C, and the closest match in the melting point corresponds to n = 20, i.e. *n*-eicosane [124]. Lan et al. [125] indicated that microcapsules of *n*-eicosane melt at a temperature close to that of *n*-eicosane in their study, which investigated synthesizing microcapsules of *n*-eicosane using an interfacial polymerization method. Alkan et al. [126] also provided the melting point of microcapsule of *n*-eicosane is 35.2 °C when they dealt with preparation, characterization, thermal properties and thermal reliability of *n*-eicosane microcapsules. The latent heat of fusion of *n*-eicosane is 246 Jg^{-1}; however, the DSC measured result indicated that the melting latent heat of DPNT06-0182 particles is 102.04 Jg^{-1}. The reason lies in the fact that DPNT06-0182 particles also have 12.5% per weight of cross-linked acrylic

polymer shell, which changes the measured latent heat value.

Accordingly, while considering the melting of PCM within DPNT06-0182 particles, the thermal properties of *n*-eicosane can be used for the relevant calculations. It should be noted, however, that the measured properties of *n*-eicosane differ in various publications, presumably due to measurement errors. Here the thermophysical parameters of *n*-eicosane are those listed in Ref. [127] and which are shown in Table 6.2.

As discussed in Chapter 3, there is a size effect on the melting point of particles in nano- or micro-structures. Using the Gibbs-Thomson equation, we can predict the changes in melting point depression with various values of radius of curvature for a small crystal of material. The particle size distribution (PSD) in a volume of DPNT06-0182 particles shows distributions of particle diameters ranging between 0.7 and 700 μm, although most particle sizes are within the 10 – 100 μm range, as shown in Fig. 6.2 [105]. In order to exhibit the melting behavior of differently-sized particles, particles with diameters of 50, 100, 500, and 700 μm respectively have been chosen for the analysis that follows.

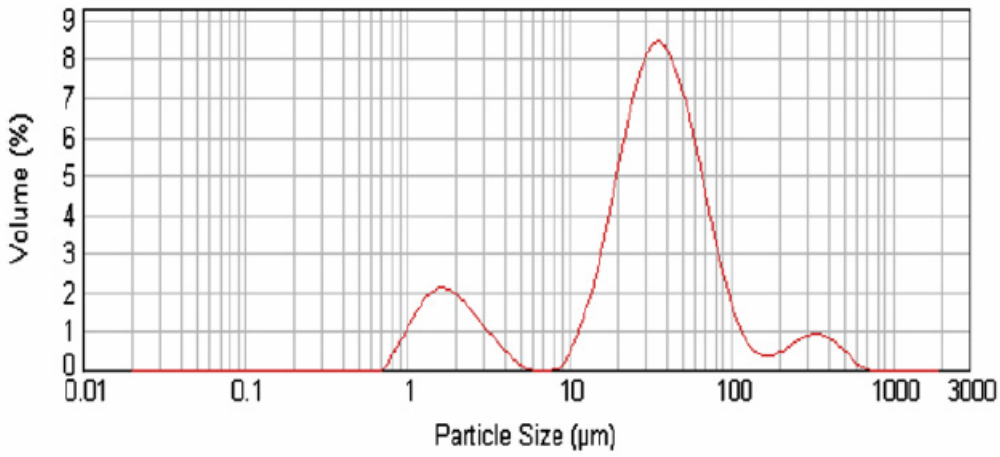

Figure 6.2: Particle size distributions of DPNT06-0182 particles [105]

Table 6.1: Melting point and latent heat of fusion: paraffins (taken from [3])

No. of carbon atoms	Melting point (°C)	Latent heat of fusion (kJ/kg)
14	5.5	228
15	10	205
16	16.7	237.1
17	21.7	213
18	28.0	244
19	32.0	222
20	36.7	246
21	40.2	200
22	44.0	249
23	47.5	232
24	50.6	255
25	49.4	238
26	56.3	256
27	58.8	236
28	61.6	253
29	63.4	240
30	65.4	251
31	68.0	242
32	69.5	170
33	73.9	268
34	75.9	269

Table 6.2: Thermophysical parameters of paraffin wax n-eicosane (C20) [127]

PCM	$k\left(\mathrm{W(mK)^{-1}}\right)$	$\rho\left(\mathrm{kgm^{-3}}\right)$	$c\left(\mathrm{kJ(kgK)^{-1}}\right)$	$L\left(\mathrm{kJ(kg)^{-1}}\right)$
n-eicosane	0.15 (solid)	778 (solid)	2.01 (solid)	241
	0.15 (liquid)	856 (liquid)	2.04 (liquid)	

The solid-liquid interfacial free energies of *n*-eicosane are obtained from the results of Yi and Rutledge [128], who studied homogeneous nucleation of *n*-eicosane crystals from the supercooled melt. Thus, a value for the solid-liquid surface energy of *n*-eicosane is $\sigma_{sl} = 0.01\ \mathrm{Jm^{-2}}$, and is used in Eq. (3.31)

for calculation of the initial melting temperatures of the particles. The density used in the calculations is the average density of both liquid phase and solid phase. The minimum melting temperature of 24.99 °C is as $T^*_{m,\min}$ in Eq. (3.31) to determine the initial melting temperature for the four particles. The results indicate the initial melting temperatures of the four particles are almost equal to this value, which implies that the micro-size radius of curvature has no influence on the depression of the melting temperature of bulk *n*-eicosane.

The melting model in Chapter 3.3 is applied, and 20 grid points are used in the liquid phase and solid phase, respectively. The time step Δt = 0.00002 is selected. The initial temperature of the solid was assumed to be 24.98 °C, which is a bit lower than the initial melting temperature of particles. The shell boundary temperature was assumed to be that of the bulk mean temperature of DPNT06-0182 slurries, which changes with melting time of the particle and determined by Eq. (5.5) at 3.5 kW of heat flux and u_m = 0.4192 ms^{-1}.

The melting front and temperature distributions of liquid-solid two-phase at different melting time were calculated for the four differently-sized DPNT06-0182 particles, with the results as shown in Figs.6.3-6.6. As seen in Fig.6.3, the melting times of each particle, given by the intersection with the x-axis, increase as expected; the respective values for $R^*_{\max}$ vary from 0.219 s for the 25 μm particle to 3.8 s for the 350 μm particle, as shown in Table 6.3.

Table 6.3: Melting time as a function of particle size

Particle size ($R^*_{\max}$)	25 μm	50 μm	250 μm	350 μm
Melting time (s)	0.22	0.47	2.61	3.80

These results indicate that the PCM of the smallest three particles melt during the phase-change stage (over the bulk mean temperature range from 24.99 °C to 38.2 °C) in DPNT06-0182 slurries. For the 350 μm particle, the melting time of 3.8 s is longer than the total melting time of 3.34 s at the mean flow rate. Note that the bulk mean temperature represents the mean temperature at a local axial position; if considering a higher initial temperature as the shell boundary temperature, e.g. 30 °C, the melting time would be shorter and this will be analyzed later.

The temperature distributions of liquid-solid two-phase for $R^*_{\max} = 250\mu m$ given at radial distances within the spherical particle for R^* = 225μm, 220μm, 195μm, …, 50μm, 25μm and 0.155μm are shown in Fig.6.4. The temperature distributions within the liquid phase (Fig. 6.4(a)) present a regular pattern, i.e. with the increase of shell boundary temperature and extension of the melting region, the temperature at each radial position gradually increases. The temperature at the liquid-solid interface changes from 24.99°C to 24.79°C, which implies that, while the melting radius decreases to 0.155 μm, the temperature of the liquid-solid interface does not have an obvious decrease according to the Gibbs-Thomson equation. The shell boundary temperature increases to 35.3 °C while the melting is complete. The temperature distribution within the solid phase (Fig. 6.4(b)) shows only very small changes during each melting stage, and the maximum predicted temperature difference is only 0.0017 °C. This shows that the effect of heat transfer through the solid region can be ignored.

Results are shown for two other particle sizes in Fig. 6.5. For the 25 μm particle, Fig.6.5 (a), the temperature of the liquid-solid interface decreases

from 25°C to 20.84°C at a radial location of 0.0073 μm. This shows that the very small radius of curvature of the liquid-solid interface ensures that the melting temperature of *n*-eicosane obviously decreases according to the Gibbs-Thomson equation. The shell boundary temperature increases to 26.1°C while the melting is complete. In Fig. 6.5(b), the temperature distributions within the liquid phase for the 350 μm particle follow a similar pattern to those of the 250 μm particle, since the minimum radial position of grid point is 0.084 μm. The shell boundary temperature increases to 40.2 °C while the melting is complete.

Once the particles have passed the melting start position shown in Fig.6.1, the particles closer to the wall radially will have higher temperatures, so the corresponding shell boundary temperature may be bigger than the bulk mean temperature of this position. Accordingly, the modelling has also investigated the case of an initial temperature of shell boundary condition being at a higher value of 30 °C. This has been done for differently-sized DPNT06-0182 particles, respectively, and the results are shown in Fig. 6.6. Here, as might be expected, the melting time for the several selective particles is shorter than for the initial boundary temperature of 25 °C used in Fig. 6.3. This is especially so for the 350 μm particle, where the melting time of 2.87 s is within the melting time of 3.34 s expected from the bulk mean temperature value. This indicates that the 350 μm particle may completely melt between the melting start position and the melting end position shown in Fig. 6.1. However, due to the rapidly-moving liquid/solid interface, the shell boundary temperature increases more quickly during the melting stage. For example, for a 50 μm particle, melting was complete as the boundary

temperature had increased from 30 °C to 30.21 °C; however, for a 350 μm particle, the boundary temperature increases from 30 °C to 41.15 °C while the melting is complete, as shown in Fig. 6.7.

In summary, the above has shown that the two-phase melting model for micro/nano particles, described earlier in Chapter 3, can be used to explain the melting behaviour of a single particle within a heat transfer suspension fluid.

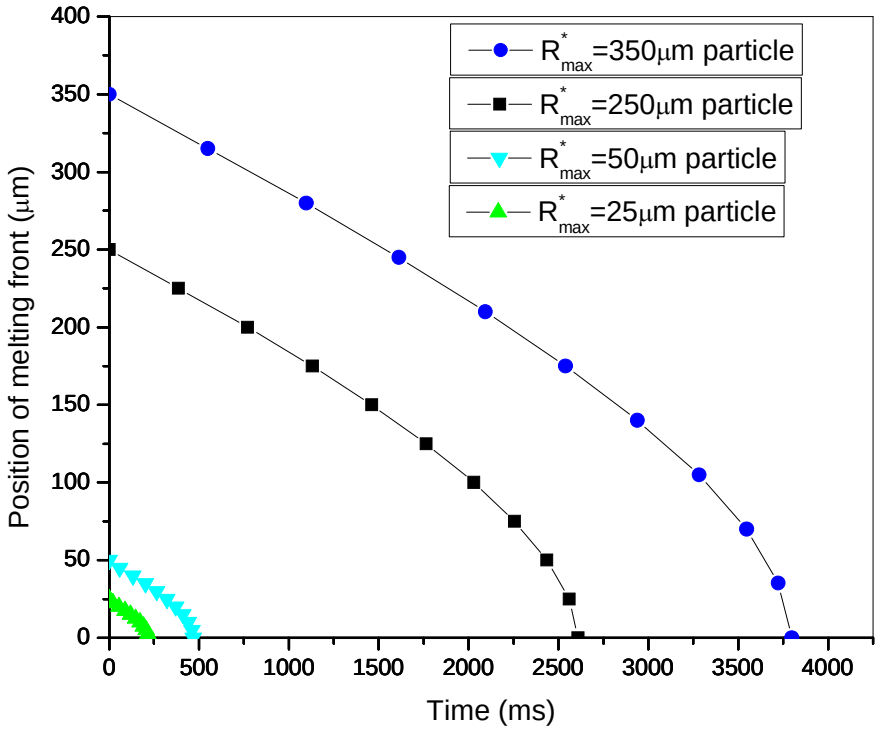

Figure 6.3: Melting front positions of differently sized particles with initial boundary temperature $T^*_{bt}\big|_{t=0}$ *= 25 ℃*

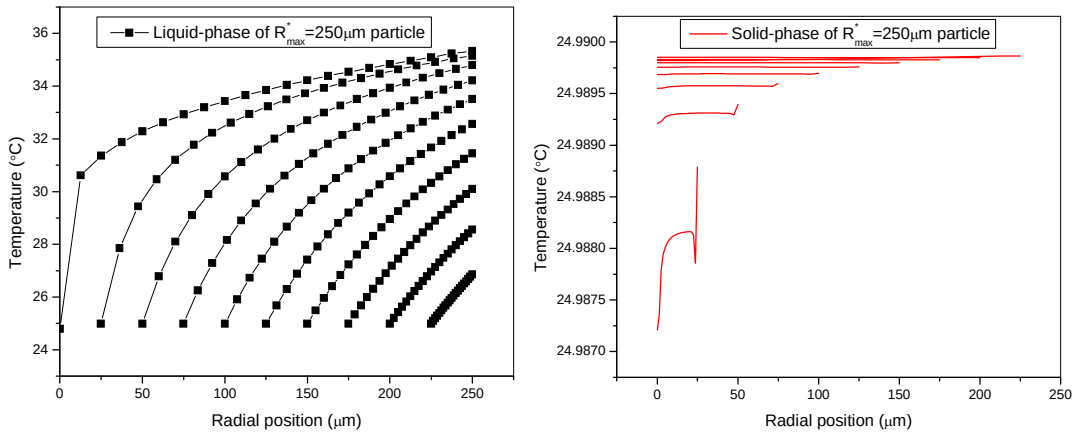

(a) (b)

Figure 6.4: Temperature distributions in both (a) the liquid phase and (b) the solid phase, as a function of radial position for $R^*_{\max}$ *= 250 μm and* $T^*_{bt}\big|_{t=0}$ *= 25 ℃. This is shown at selected time values between* t *= 0.38 and 2.61 s.*

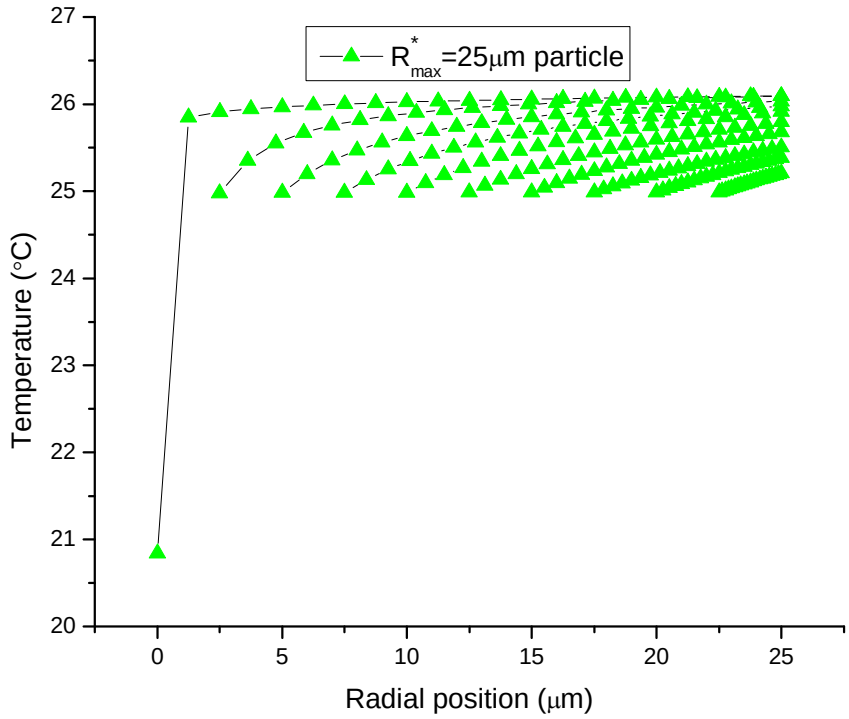

(a)

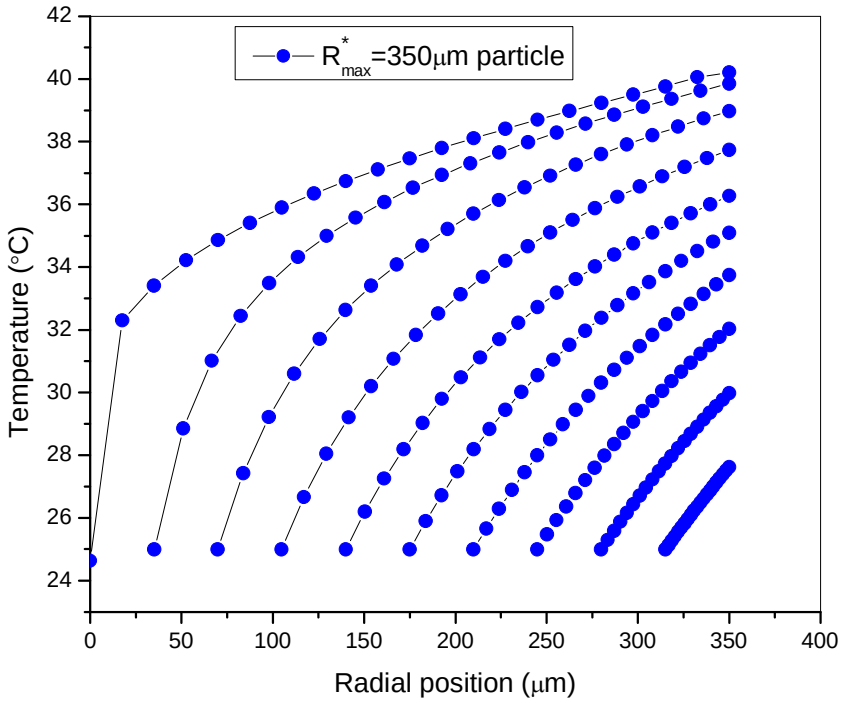

(b)

Figure 6.5: Temperature distributions in the liquid phase region with $T_{bt}^{*}\big|_{t=0}$ = *25 ℃, for (a) a 25 μm particle, and (b) a 350 μm particle.*

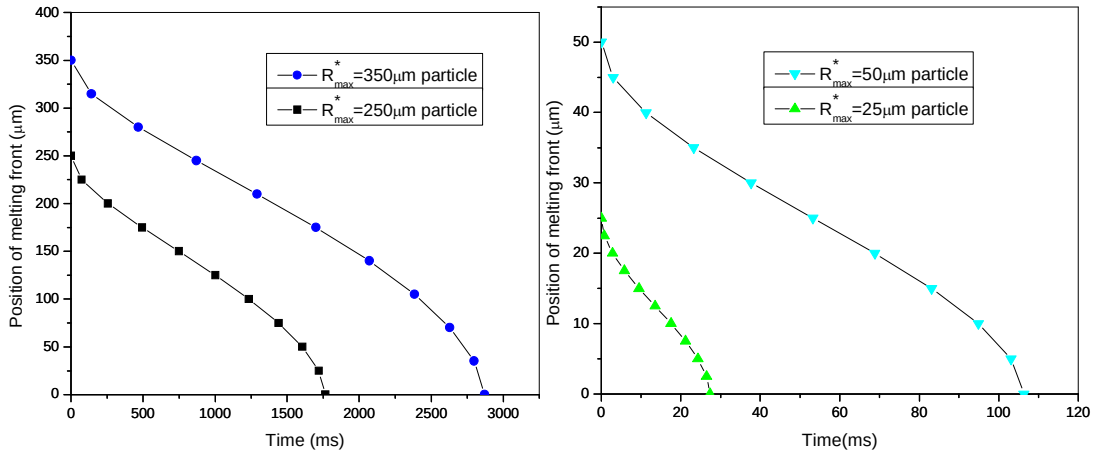

(a) (b)

Figure 6.6: Melting front positions of differently sized particles with initial boundary temperature $T_{bt}^{*}\big|_{t=0}$ = *30 ℃, for (a) big particles, and (b) small particles.*

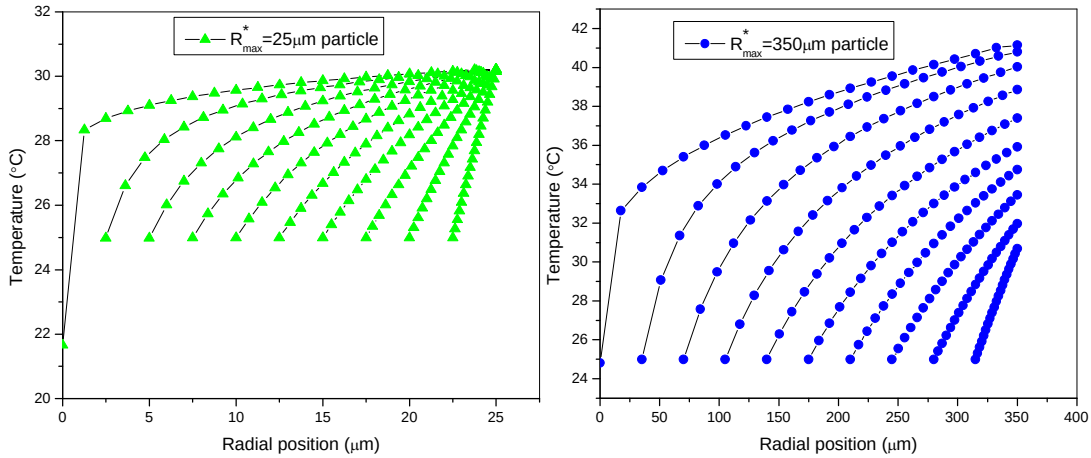

(a) (b)

Figure 6.7: Temperature distributions in liquid-phase region with $T_{bt}^{*}\big|_{t=0}$ *= 30 ℃. (a) at times ranging from t =0.75 ms to 27.4 ms for a particle with* $R_{\max}^{*}$ *= 25 μm; (b) at times ranging from t = 0.14 s to 2.87 s for a particle with* $R_{\max}^{*}$ *= 350 μm.*

6.3 The flow characteristics of DPNT06-0182 slurries in a pipe

In Chapter 5, two methods were used to evaluate local heat transfer coefficients. One adopted the direct measured data, whereas the other applied a correction method to correct the measured errors of wall temperatures. Because water is a Newtonian fluid, empirical correlations can be conveniently used to calculate the value of the coefficient at each location. However, most MPCS are non-Newtonian fluids that involve more complicated momentum diffusivity problems which need to be clarified. Hence, some of the non-Newtonian features of 10% DPNT06-0182 slurries are analyzed in the following discussion.

6.3.1 Shear rate at the wall

Assume that we are dealing with laminar pipe flow. The velocity profile for a Newtonian fluid in laminar flow is parabolic, and can be expressed as:

$$v_x = 2u_m\left(1-\frac{r^2}{R_i^2}\right) \tag{6.1}$$

The wall shear rate for a Newtonian fluid $\dot{\gamma}_{WN}$ is given as:

$$\dot{\gamma}_{WN} = \frac{dv}{dr}\Big|_{r=R_i} = -\frac{4u_m}{R_i} == -\frac{8u_m}{D_i} \tag{6.2}$$

Here, the quantity $8u_m/D_i$ is known as the flow characteristic [129]. Two quantities K' and n' are defined to describe the $\tau_w -$ flow characteristic curve. The symbol n' is the gradient of τ_W against $8u_m/D_i$ on logarithmic axes (Eq. (6.3)), and K' is as defined by Eq. (6.4) [129].

$$n' = \frac{dLn\tau_W}{dLn\left(8u_m/D_i\right)} \tag{6.3}$$

$$\tau_w = K'\left(\frac{8u_m}{D_i}\right)^{n'} \tag{6.4}$$

The wall shear rate for non-Newtonian fluid can be expressed as the flow characteristic multiplied by a correction factor and is described by the Rabinowitsch- Mooney equation, which can be written as [129]:

$$\dot{\gamma}_W = -\frac{8u_m}{D_i}\left[\frac{3}{4}+\frac{1}{4}\frac{dLn\left(8u_m/D_i\right)}{dLn\tau_W}\right] = -\frac{8u_m}{D_i}\left[\frac{3n'+1}{4n'}\right] = \dot{\gamma}_{WN}\left[\frac{3n'+1}{4n'}\right] \tag{6.5}$$

Also, the wall shear stress of 10% DPNT06-0182 slurry may be calculated as:

$$\tau_W = \frac{D_i\Delta P}{4L} = \frac{10\times10^{-3}}{4\times2.4}\Delta P = 1.042\times10^{-3}\Delta P \tag{6.6}$$

The flow rate-pressure drop measurements for 10% DPNT06-0182 slurry are shown in Table 6.4:

Table 6.4: Flow rate-pressure drop measurements for 10% DPNT06-0182 slurry

Pressure drop Δp (Pa)	mean flow rate u_m (m/s)
1269.5	0.42
1855.6	0.56
4523.8	1.00
8536.1	1.48
13604.5	1.95
19223.3	2.37

Table 6.5: The shear rate and shear stress of wall for 10% DPNT06-0182 slurry at different flow rates

τ_w (pa)	$8u_m/D_i$ (s^{-1})	n'	$(3n'+1)/4n'$	$-\dot{\gamma}_W$ (s^{-1})
1.3228	335.36	1.3466	0.9357	313.80
1.9335	444.56	1.4546	0.9219	409.84
4.7138	803.36	1.5625	0.9100	731.06
8.8946	1180.6	1.6614	0.9005	1063.13
14.176	1558.6	1.7145	0.8958	1396.19
20.031	1895.6	1.7662	0.8915	1689.93

Using these values, some important characteristic parameters of 10% DPNT06-0182 slurry at different flow rates including the shear rate and shear stress at the wall have been calculated, and the results are shown in Table 6.5. With increase of the flow rate, both of the pressure drop and the shear stress at the wall increase, and the shear rate at the wall increases. However, all correction factors ($(3n'+1)/4n'$) for different flow rates are less than 1 and

it gradually decreases with the increase of the flow rate.

6.3.2 Generalized Reynolds number for non-Newtonian MPCS in pipe flows

In the case of a non-Newtonian fluid, it is necessary to define an appropriate viscosity so as to determine the Reynolds number. However, for a fluid in a pipe, the shear stress varies with radial location, so that the viscosity is a variable at a constant axial location. The quantity μ_{ap}, which may be called the apparent viscosity for pipe flow, is based on flow characteristics and is given by:

$$\mu_{ap} = \frac{\text{shear stress at wall}}{\text{flow characteristic}} = \frac{\tau_w}{8u_m/D_i} = K'\left(\frac{8u_m}{D_i}\right)^{n'-1} \tag{6.7}$$

A generalized Reynolds number Re' for a non-Newtonian fluid was suggested by Metzner and Reed [130] as:

$$\mathrm{Re}' = \frac{\rho u_m D_i}{\mu_{ap}} = \frac{\rho {u_m}^{2-n'} {D_i}^{n'}}{8^{n'-1}K'} \tag{6.8}$$

It should be noted that the shear thinning and shear thickening behavior is usually approximated by the power law, and such materials are called ‘power law fluids’, which can be defined for the pipe wall via

$$\tau_w = K\left(-\dot{\gamma}_w\right)^n \tag{6.9}$$

According to the Rabinowitsch-Mooney equation (Eq. (6.5)), then

$$\tau_w = K\left(\frac{8u_m}{D_i}\right)^n \left(\frac{3n'+1}{4n'}\right)^n . \tag{6.10}$$

A plot of $Ln\tau_w$ against $Ln\left(8u_m/D_i\right)$ has a constant gradient n, so that

$$n' = n \quad K' = K\left(\frac{3n+1}{4n}\right)^n \tag{6.11}$$

The generalized Reynolds number for 10% DPNT06-0182 slurry can now be calculated at different flow rates, and the various values of interest are shown in Table 6.6.

Table 6.6: Generalized Reynolds number Re′ for 10% DPNT06-0182 slurry at different flow rates

Re'	μ_{ap} (Pa s)	mean flow rate u_m (m/s)
1031.9	0.0039	0.42
1240.6	0.0044	0.56
1661.8	0.0059	1.00
1901.9	0.0075	1.48
2080.0	0.0091	1.95
2177.3	0.0106	2.37

Ryan and Johnson [131] suggested that the transition from laminar to turbulent flow for inelastic non-Newtonian fluids occurs at a critical value of the generalized Reynolds number Re', and that this depends on the value of n'. The results are shown in Fig.6.8. For a 10% DPNT06-0182 slurry at mean flow rates (u_m) of 0.42, 0.56 and 1.00 ms^{-1}, the slurries exhibit laminar flow; conversely, for u_m values of 1.48, 1.95 and 2.37 ms^{-1}, the slurries are in turbulent flow. In addition, as seen in Fig. 5.10, the relationships between pressure drop and mean velocity for DPNT06-0182 slurries and water are illustrated. For 10% DPNT06-0182 slurry, the pressure drop is approximately proportional to the mean flow rate for the three lower flow rates. The

pressure drop increases more rapidly for the higher flow rate values, implying that the slurry exhibits turbulent flow under these conditions. Note that turbulent flow has the advantage of enhancing convective heat and mass transfer, but this also means that an increased input power is required to pump the fluid.

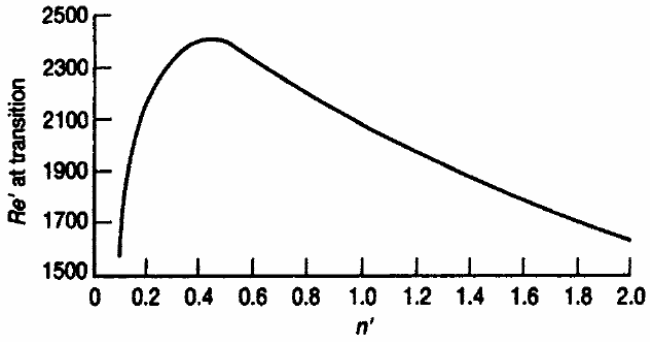

Figure 6.8: variation of the critical values of the Reynolds number with n' [131]

6.3.3 Velocity profiles of DPNT06-0182 slurries in a pipe

For a steady, fully developed laminar flow, the shear stress distribution is given:

$$\tau_{rx} = \frac{r}{2}\left(\frac{\Delta P}{L}\right) \quad , \tag{6.12}$$

and for a power law fluid, if v_x denotes the velocity of radius r location, then

$$\tau_{rx} = K\left(-\frac{dv_x}{dr}\right)^n \tag{6.13}$$

with the boundary condition:

$$v_x = 0 \quad at \quad r = R_i \tag{6.14}$$

Based on the above equations and boundary condition, the velocity profile

of a laminar fluid is given by [129]:

$$v_x = \left(\frac{\Delta P}{4KL/D_i}\right)^{1/n}\left(\frac{n}{n+1}\right)R_i\left[1-\left(\frac{r}{R_i}\right)^{(n+1)/n}\right]. \quad (6.15)$$

Eq. (6.15) can further simplified as [129]:

$$\frac{v_x}{u_m} = \left(\frac{3n+1}{n+1}\right)\left[1-\left(\frac{r}{R_i}\right)^{n+1/n}\right]. \quad (6.16)$$

The velocity equation of turbulent core was deduced by Dodge and Metzner [132] and corrected coefficients were given by Skelland [133], as follows:

$$v^+ = \frac{5.66}{n^{0.75}}\log y^+ - \frac{0.566}{n^{1.2}} + \frac{3.475}{n^{0.75}}\left[1.960 + 0.815n - 1.628n\log\left(\frac{3n+1}{n}\right)\right], \quad (6.17)$$

where v^+ and y^+ are a dimensionless velocity and distance from the wall, respectively, and are defined as:

$$v^+ = \frac{\overline{v}_x}{v_*} \quad (6.18)$$

$$y^+ = \frac{\rho v_*^{(2-n)} y^n}{K} \quad (6.19)$$

$$v_* = \sqrt{\frac{\tau_w}{\rho}} \quad (6.20)$$

The velocity profiles of 10% DPNT06-0182 slurry have been calculated using Eq. (6.16) and Eq. (6.17) at different flow rates, and the results are shown in Fig. 6.9. For turbulent fluids, the velocity increases very quickly in an extremely thin layer which is close to the wall. For laminar fluids at the lower flow rate values, the velocity gradually increases from the wall to the core. Thus, the velocity profile of the 10% DPNT06-0182 slurry is predicted to be much flatter as expected for the higher values of u_m , under which it is

turbulent (and hence requiring a greater pump power).

Here, we can provide a further analysis regarding the melting behavior of 10% DPNT06-0182 slurry at a mean flow rate of u_m = 0.42 ms^{-1}. As seen in Fig.6.9 (a), the maximum of velocity at the centre line is 0.90 ms^{-1} for this mean flow rate. This means that the more accurate time for a particle which is located at the centre line to pass through the defined phase change region is 1.55 s. Also, the time to pass through the test section will be 2.67 s. As can be seen in Table 6.3, the particles of $R^*_{\max} \leq$ 50μm will all melt if they pass along the centre line. However, the particles with their size ≥ 500 μm may not melt if they are located at the centre line, but they will melt if they flow along an axial position which is close to wall (following the analysis of section 6.2). Even though these particles which are close to the centre line may not melt, the effect can be neglected because as seen in Fig.6.2, the size of majority of particle sizes are within the 10 – 100 μm range, and less than 1% of particles have a size of 500 μm. There are also very few particles with a size greater than this. Thus, it can be assumed that the full phase change is basically realized in our system for DPNT06-0182 slurries.

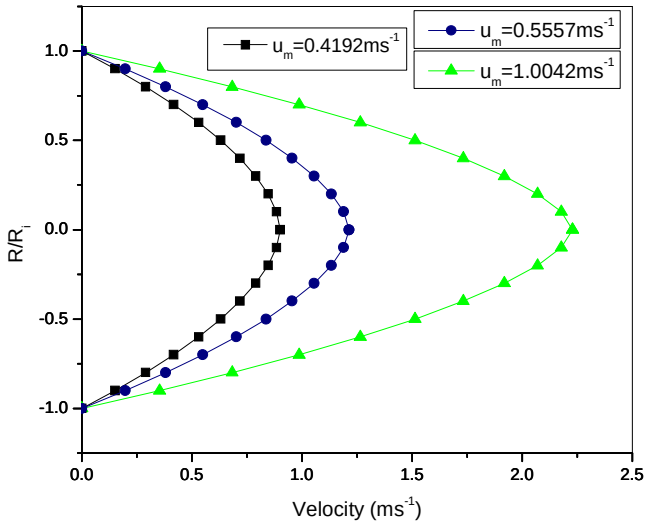

(a) Laminar fluids

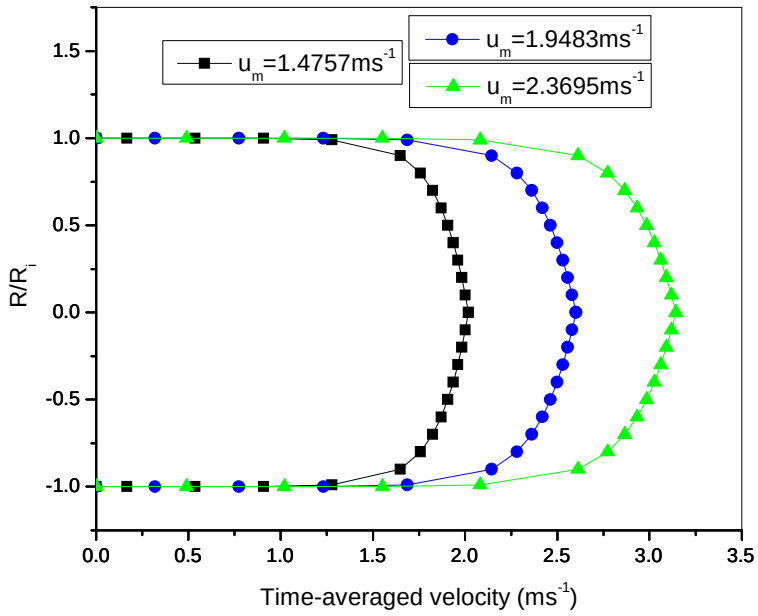

(b) Turbulent fluids

Figure 6.9: Velocity profiles of 10% DPNT06-0182 slurry at different flow rates

6.4 Conclusions

A two-phase melting model for micro/nano sized particles has been used to analyze the melting behavior of DPNT06-0182 particles in a heat transfer pipe flow. The results indicate that the model can be used to predict the melting time of particles of MPCS flowing in a heat transfer channel, and provide evidence to determine the relationship between heat transfer characteristics and phase change behavior of these materials. Based on a generalized Reynolds number defined for non-Newtonian fluid, the laminar and turbulent velocity profiles of 10% DPNT06-0182 slurry can be predicted under different flow rates. It has thus been shown that this modeling approach allows a greater understanding of the behaviour of these phase change materials, when present as a slurry.

Chapter 7
Conclusions and further work

7.1 Summary of the main conclusions

In this thesis, the solidification and melting models of a single PCM particle have been constructed. An effective numerical method for the problem of a spherical particle with a moving boundary was developed and validated by an iterative analytical series solution. A new liquid-solid interface model has been proposed, which is aimed at mixture PCM materials. The relationship between the material composition, the solid fraction and the freezing temperature was modeled as the solidification of a particle took place. A test rig has also been built, and the heat transfer behaviour of DPNT06-0182 slurries involving a phase change has been investigated and analyzed. A full, two-phase micro/nano melting model of a sphere has been solved, and has been used successfully to analyze the melting behavior of differently-sized DPNT06-0182 particles in a heat transfer pipe flow.

7.1.1 Solidification of a particle

Consider first the solidification of a single PCM particle. Here, the heat diffusion equation of a sphere with a liquid-solid moving interface model was used. The calculated results can be used to estimate several factors, such as the time taken for a phase change to occur, the temperature evolution of the solid regions, and the solidified volume fraction.

An effective and stable numerical method combined with mathematical transformation of dimensionless variables in equations was proposed and

developed for predicting the phase change of a spherical particle. The purpose of transformation of variables was to simplify the moving boundary problem to a fixed boundary for the diffusion equation of a sphere under phase change conditions could be considered. The resulting numerical method that was developed took advantage of both Explicit and Implicit Euler methods. An iterative analytical series solution was also used to solve the same equations for the solidification of a particle, and the results agree with the numerical method very well. Thus, the effective numerical solution was validated, and used as a basic method to solve the solidification and melting of a spherical particle involving more complicated physical problems.

7.1.2 New models for liquid-solid interface

New models were proposed for evolution of the liquid-solid interface temperature when the melting or freezing temperature was not a constant. A based solid fraction liquid-solid interface temperature model was proposed, and used to explore the effect of binary phase composition on the solidification of both an encapsulated metallic PCM particle and a PCM particle containing a mixture. The model depends on the characteristics of materials, and the solid fraction may be determined by experimental measurements or equilibrium phase diagrams. For a PCM with a complicated relationship between the freezing temperature and solid fraction, a numerical interpolation and a local linear rule was determined for tracking the changes in liquid-solid interface temperature. The new liquid–solid interface model can clearly explain the solidification behaviour of the alloy or mixture under different cooling conditions (e.g. the constant temperature or constant cooling rate boundary conditions).

A full two-phase melting model of micro/nano MPCM particles was constructed, and solved for modelling the melting point depression caused by the surface energy of the curved interface between the crystal and its own liquid as a phase change proceeds. MPCM particles of different sizes are defined as having their own initial melting points. These are dependent on the minimum melting temperature of the powder (tested by DSC), the particle size and the Gibbs-Thomson equation.

7.1.3 Construction of a test rig

A test rig was built to explore the phase change heat transfer behavior of MPCS flowing through a circular tube for a given constant heat flux. High accuracy sensors were used to measure key parameters including local fluid temperatures, local wall temperatures, flow rates and pressure drop throughout the test section. The cooling sub-system, which consisted of a powerful chiller and a matching heat exchanger, provided a flexible method for adjusting the inlet temperature of the test section. This meant that the effect of a complete phase change, a partial phase change and no phase change could all be observed within the test system.

The experimental system was first validated by using water as a test medium. The measured pressure drops were compatible with the predictions of Colebrook-White and Blasius equations, although the resultant errors were relatively greater at the lowest flow rates. In addition, system errors of local wall temperatures were analyzed and estimated by using an empirical Petukhov correlation.

7.1.4 Experimental investigation of MPCS slurries

A slurry containing microencapsulated PCM from Ciba Specialty Chemicals, UK has been investigated experimentally using the self-developed test rig. The thermophysical properties of DPNT06-0182 slurries such as specific heat capacity, thermal conductivity and dynamic viscosity were determined based on the measured data of particles and slurries by using differential scanning calorimetry (DSC), Hot Disk instruments and a rheometer, in order to provide basic parameters for further analysis of heat transfer characteristics of the MPCS. The local bulk mean temperature of slurries was calculated by the effective specific heat capacity which was determined by DSC measurements.

For the same energy efficiency, it was observed in experiments that the flow rate of MPCS was lower than that of water. A full phase change needs a lower flow rate to be realized, which will result in high wall temperatures in MPCS compared with water. Either using the direct measured data or corrected data, comparisons of MPCS with a 10% mass fraction to water and a 5% mass fraction slurry indicate that the heat transfer coefficient of a 10% mass fraction MPCS is the lowest and its pressure drop is also the lowest, but the most heat energy is stored during the passage through the heated test section.

Under higher flow rate conditions, and in the absence of a phase change, the bulk mean temperatures of a MPCS are higher than those of water under the same heating flux, due to the lower specific heat capacities of MPCS. However, the corresponding wall temperatures of MPCS increase less than water in relative terms, so that the local heat transfer coefficients of MPCS with a 10% mass fraction are bigger than both MPCS with a 5% mass

fraction and water. Correspondingly, the pressure drop of MPCS with a 10% mass fraction is the largest. Note that it is possible to control the flow rate so as to cause partial phase changes within the MPCS, so that a comparison of heat transfer coefficients between the above two situations could be obtained.

As a result, an MPCS exhibits a very flexible method for design of thermal energy transportation system compared to a single phase fluid; the outlet temperature of a heat transfer channel can be adjusted by mass fraction of MPCS. Thus, the experimental results can be used to design thermal energy transportation systems where an MPCS is considered as the heat transfer fluid.

7.1.5 Melting behavior of DPNT06-0182 particles in a heat transfer pipe flow

A two-phase melting model for micro-nano sized particles has been used to analyze the melting behavior of DPNT06-0182 particles in a heat transfer pipe flow. The boundary conditions of a single particle are based on the heat flux, the flow rate and the position of the particle in fluid, so that the shell boundary temperature of a particle will increase with an increase of the local bulk mean temperature. The results indicate that the model can be used to predict the melting time of particles within an MPCS flowing in a heat transfer channel, which agrees with the group melting behavior of MPCM as observed via the local bulk mean temperature. The model presents a unique method for estimating heat transfer characteristics involving phase change of micro/nano particles.

7.2 Future work

The enthalpy method is an effective numerical method for investigating the full two-phase melting or solidification problem, as it does not need to solve the moving boundary problem directly. However, it cannot be applied to more general problems. In this thesis, a numerical method was developed to solve a full two-phase melting model with a moving liquid-solid interface problem, but for the shell boundary only the condition where temperature changed with time was considered. Such models under convective boundary and periodic boundary conditions have not been solved in the current study. Thus, there is further work required to develop efficient numerical algorithms to solve these particular problems.

In construction of the test rig, I analyzed the system error of local wall temperatures due to the heating mode of rope heaters. In future work, the heating method will be improved, for example, to heat the internal fluid via the ends of the test section directly.

The existing theory related to heat transfer of a non-Newtonian fluid needs to be developed further. This is because some empirical equations that are based on the assumption of a Newtonian fluid cannot explain heat transfer behaviour of the micro/nano suspension fluids. The difficulty lies in the properties of fluid changes with temperature and the effect of particle size, especially involving latent heat absorption or release. This will result in more complicated heat transfer problems in a suspension fluid. In future work, we will study a new wall-function model to predict wall temperatures of MPCS in a heat transfer channel, so as to initiate an investigation into this important topic.

References

[1] P. Charunyakorn, S. Sengupta, S. K. Roy. Forced convection heat transfer in microencapsulated phase change material slurries: flow in circular ducts. Int. J. Heat Mass Transfer, 1991, 34: 819-833.

[2] F. Baylin, Low temperature thermal energy storage: a state of the art survey, Report no. SERI/RR/-54-164. Golden, Colorado, USA: Solar Energy Research Institute; 1979.

[3] A. Sharma, V. V. Tyagi, C. R. Chen, D. Buddhi, Review on thermal energy storage with phase change materials and applications, Renewable and sustainable energy reviews, 2009, 13: 318–345.

[4] A. Abhat, Low temperature latent heat thermal energy storage, In: C. Beghi, editor. Thermal energy storage. Dordrect, Holland: D. Reidel Publication Co., 1981.

[5] A. Heinz, W. Streicher, “Application of phase change materials and PCM-slurries for thermal energy storage”. http://intraweb.stockton.edu/eyos/energy_studies/content/docs/FINAL_PAPERS/8B-4.pdf

[6] L. Cabeza, Storage techniques with phase change materials, Thermal energy storage for solar and low energy buildings, State of the art by the IEA Solar Heating and Cooling Task 32, 2005, Seite 77-105.

[7] A. George, Hand book of thermal design, In: Guyer C, editor. Phase change thermal storage materials, McGraw Hill Book Co., 1989 [chapter 1].

[8] http://www.cristopia.com/cristopia/english/products/indproducts.html

[9]http://www.sglgroup.com/cms/international/products/product-

groups/gpnm/cold-storage-systems-for-engine-off-operation-of-truck-air-contioning/index.html?__locale=en

[10] P. Schossig, H.-M. Henning, S. Gschwandera, T. Haussmann, Micro-encapsulated phase-change materials integrated into construction materials, Solar Energy Materials & Solar Cells, 2005, 89: 297–306.

[11] D. A. Neeper, Thermal dynamics of wallboard with latent heat storage, Sol. Energy, 2000, 68: 393–403.

[12] A. Khudhair, M. Farid, N. Ozkan, J. Chen, Thermal performance and mechanical testing of gypsum wallboards with latent heat storage, in: Proceedings of Annex 17, Advanced Thermal Energy Storage Through Phase Change Materials and Chemical Reactions Feasibility Studies and Demonstration Projects, Indore, India, 2003.

[13] M. M. Farid, W. J. Kong, Under floor heating with latent heat storage, Proc. Inst. Mech. Eng, 2001, 215: 601–609.

[14] W. Meier, Polymer nanocapsules, Chemical Society Reviews, 2000, 29: 295-303.

[15] A. D. Dinsmore, Ming F. Hsu, M. G. Nikolaides, Manuel Marquez, A. R. Bausch, and D. A. Weitz, Colloidosomes: Selectively Permeable Capsules Composed of Colloidal Particles, Science, 2002, 298: 1006-1009.

[16] C. Clearly et al., ‘‘Hydraulic characteristics of ice slurry and chilled water flows,’’ IEA District Heating: Advanced Energy Transmission Fluid-Final Report of Research, Novem BV, Sittard, Netherlands, 1990.

[17] J. L. Alvarado, B. G. Jones, C. P. Marsh *et al.*, “Thermal performance of microencapsulated phase change material slurry,” US Army Corps of Engineers® Engineering Research and Development Center, 2008.

[18] http://www.microteklabs.com/technical_overview.html

[19] X. X. Zhang, Y. F. Fan, X. M. Tao, K. L. Yick, Fabrication and properties of microcapsules and nanocapsules containing *n*-octadecane, Materials Chemistry and Physics, 2004, 88: 300–307.

[20]http://worldaccount.basf.com/wa/EU~en_GB/Catalog/ACIndustry/pi/BASF/segment/new_building_materials

[21] M. L. Nuckols, Analytical modeling of a diver dry suit enhanced with micro-encapsulated phase change materials, Ocean Engineering, 1999, 26: 547–564.

[22] S. Gschwander, P. Schossig, H.-M.Henning, Micro-encapsulated paraffin in phase-change slurries, Solar Energy Materials & Solar Cells, 2005, 89: 307-315.

[23] B. M. Diaconu, S. Varga, A. C. Oliveira, Experimental assessment of heat storage properties and heat transfer characteristics of a phase change material slurry for air conditioning applications, Appl. Energy, 2010, 87: 620-628.

[24] http://www.fraunhofer.de/en/

[25]http://www.micronal.de/portal/load/fid443847/BASF_Micronal_PCM_Brochure%202009_English.pdf

[26] A. G. Entrop, H. J. H. Brouwers, A. H. M. E. Reinders, Experimental research on the use of micro-encapsulated Phase Change Materials to store solar energy in concrete floors and to save energy in Dutch houses, Solar Energy, 2011, 85: 1007–1020.

[27] A. de Gracia, E. Oró, M.M. Farid, L.F. Cabeza, Thermal analysis of including phase change material in a domestic hot water cylinder, Applied Thermal Engineering, 2011, 31: 3938-3945.

[28] F. L. Tan, C. P. Tso, Cooling of mobile electronic devices using phase change materials, Applied Thermal Engineering, 2004, 24: 159–169.

[29] M. Hunger, A. G. Entropa, I. Mandilaras, H. J. H. Brouwers, M. Founti, The behavior of self-compacting concrete containing micro-encapsulated Phase Change Materials, Cement & Concrete Composites, 2009, 31: 731–743.

[30] M. Rady, Granular phase change materials for thermal energy storage: Experiments and numerical simulations, Applied Thermal Engineering, 2009, 29: 3149-3159.

[31] S. T. Revankar, T. Croy. Visualization study of the shrinkage void distribution in thermal energy storage capsules of different geometry, Experimental Thermal and Fluid Science, 2007, 31: 181–189.

[32]http://www.sglgroup.com/export/sites/sglcarbon/_common/downloads/products/product-groups/eg/construction-materials-ecophit/ECOPHIT_PCM-Flyer_e.pdf

[33] P. Zhang, Z. W. Ma, R. Z. Wang, An overview of phase change material slurries: MPCS and CHS, Renewable and sustainable energy reviews, 2010, 14: 598–614.

[34] P.W. Griffiths, P. C. Eames, Performance of chilled ceiling panels using phase change material slurries as the heat transport medium, Applied Thermal Engineering 2007, 27: 1756–1760.

[35] X. Wang, J.L. Niu, A.H.C. van Paassen, Raising evaporative cooling potentials using combined cooled ceiling and MPCM slurry storage, Energy and Buildings, 2008, 40: 1691–1698.

[36] Y. Dutil, D. R. Rousse, N. B. Salah, et al., A review on phase-change materials: Mathematical modeling and simulations, Renewable and Sustainable Energy Reviews, 2011, 15: 112–130.

[37] J. Stefan, Uber einige probleme der theorie der warmeleitung, Sber Akad Wiss Wien, 1889, 98: 473–484.

[38] J. Crank, Free and moving boundary problems, Oxford: Clarendon Press, 1984.

[39] J. M. Hill, One-dimensional Stefan problems: an introduction. Harlow: Longman Scientific Technical, 1987.

[40] Y. P. Shih, S. Y. Tsay, Analytical solutions for freezing a saturated liquid inside or outside cylinders, Chem. Eng. Sci, 1971, 26: 809-816.

[41] Y. P. Shih, T. C. Chou, Analytical solutions for freezing a saturated liquid inside or outside spheres, Chem. Eng. Sci, 1971, 26: 1787-l793.

[42] R. I. Pedroso, G. A. Domoto, Inward spherical solidification-solution by the method of strained coordinates, Int. J. Heat Mass Transfer, 1973, 16: 1037-1043.

[43] D. S. Riley, F. T. Smith, G. Poots, The inward solidification of spheres and circular cylinders, Int. J. Heat Mass Transfer, 1974, 17: 1507-1516.

[44] G. B. Davis, J. M. Hill, A moving boundary problem for the sphere, Ima. J. Appl. Math, 1982, 29: 99-111.

[45] J. M. Hill, A. Kucera, Freezing a saturated liquid inside a sphere, Int. J. Heat Mass Transfer, 1983, 26: 1631-1637.

[46] J. Caldwell, S. Savovic, Y. Y. Kwan, Nodal integral and finite difference solution of one-dimensional Stefan problem, J. Heat Transfer, 2003, 125: 523-527.

[47] S. Savovic, J. Caldwell, Numerical solution of Stefan problem with time-dependent boundary conditions by variable space grid method, Therm. Sci, 2009, 13: 165-174.

[48] S. Savovic, J. Caldwell, Finite difference solution of one-dimensional Stefan problem with periodic boundary conditions, Int. J. Heat Mass Transfer, 2003, 46: 2911–2916.

[49] E. Javierre, C. Vuik, F.J. Vermolen, S. Van der Zwaag, A comparison of numerical models for one-dimensional Stefan problems, J. Comput. Appl. Math, 2006, 192: 445–459.

[50] C. J. Kim, M. Kaviany, A numerical method for phase-change problems, Int. J. Heat Mass Transfer, 1990, 33: 2721–2734.

[51] N. S. Asaithambi, A Galerkin method for Stefan problems, Appl. Math. Comput, 1992, 52: 239–250.

[52] N. S. Asaithambi, A variable time-step Galerkin method for a one-dimensional Stefan problem, Appl. Math. Comput, 1997, 81: 189–200.

[53] V. R. Voller, Fast implicit finite-difference method for the analysis of phase change problems, Numer Heat Transfer Part B, 1990, 17: 155–169.

[54] V. R. Voller, A fixed grid numerical modelling methodology for convection-diffusion mushy region phase-change problems, Int. J. Heat Mass Transfer, 1987, 30: 1709-1719.

[55] C. R. Swaminathan, V. R. Voller, On the enthalpy method, Int J Numer Methods Heat Fluid Flow, 1993, 3: 233–44.

[56] V. R. Voller, M. Cross, N. C. Markatos, An enthalpy method for convection/diffusion phase change, Int J Numer Methods Eng, 1987, 24: 271–84.

[57] V. Alexiades, A. D. Solomon, Mathematical modeling of melting and freezing processes, USA: Hemisphere Publishing Corporation; 1993.

[58] B. Nedjar. An enthalpy-based finite element method for nonlinear heat problems involving phase change. Comput Struct, 2002, 80: 9–21.

[59] S. W. Mccue, B. Wu, J. M. Hill, Micro/nanoparticle melting with spherical symmetry and surface tension, IMA Journal of Applied Mathematics, 2009, 74: 439−457.

[60] C. W. Chan, F. L. Tan, Solidification inside a sphere-an experimental study, Int. Commun, Heat Mass Transfer, 2006, 33: 335-341.

[61] T. Saitoh, K. Hirose, High-performance of phase change thermal energy storage using spherical capsules, Chem Eng Commun, 1986, 41: 39–58.

[62] M. Esen, T.Ayhan, Development of a model compatible with solar assisted cylindrical energy storage tank and variation of stored energy with time for different phase-change materials, Energy Conversion and Management, 1996, 37(12): 1775-1785.

[63] M. Esen, A.Durmus, A.Durmus, Geometric design of solar-aided latent heat store depending on various parameters and phase change materials, Solar Energy, 1998, 62(1): 19-28.

[64] M. Esen, Thermal performance of a solar-aided latent heat store used for space heating by heat pump, Solar Energy, 2000, 69(1): 15-25.

[65] A. F. Regin, S. C. Solanki, J. S. Saini. (2009) “An analysis of a packed bed latent heat thermal energy storage system using PCM capsules:

Numerical investigation", Renewable Energy, Vol. 34, pp. 1765–1773.

[66] Y. P. Zhang, K. P. Lin, Y. Jiang, G. B. Zhou, Thermal storage and nonlinear heat-transfer characteristics of PCM wallboard, Energy and Buildings, 2008, 40: 1771-1779.

[67] M. Rostamizadeh, M. Khanlarkhani, S. M. Sadramelib, Simulation of energy storage system with phase change material (PCM), Energy and Buildings, 2012, 49: 419–422.

[68] A. H. Mosaffa, C. A. Infante Ferreira, F. Talati, M. A. Rosen, Thermal performance of a multiple PCM thermal storage unit for free cooling Energy Conversion and Management, 2013, 67: 1–7.

[69] J. C. Kurnia, A. P. Sasmito, S. V. Jangam, A. S. Mujumdar, Improved design for heat transfer performance of a novel phase change material (PCM) thermal energy storage (TES), Applied Thermal Engineering, 2013, 50: 896-907.

[70] P. Dolado, A. Lazaro, J. M. Marin, B. Zalba, Characterization of melting and solidification in a real scale PCM-air heat exchanger: Numerical model and experimental validation, Energy Conversion and Management, 2011, 52, 1890–1907.

[71] J. Y. Long, D. S. Zhu, Numerical and experimental study on heat pump water heater with PCM for thermal storage, Energy and Buildings, 2008, 40: 666–672.

[72] W. K. Liu, E. G. Karpov, S. Zhang, H. S. Park, An Introduction to computational nanomechanis and materials, Comput. Methods. Appl. Mech. Engrg, 2004, 193: 1529-1578.

[73] M. Delgado, A. Lázaro, J. Mazo, et al., Experimental analysis of a

microencapsulated PCM slurry as thermal storage system and as heat transfer fluid in laminar flow, Appl Therm Eng, 2012, 36: 370-377.

[74] M. Goel, S. K. Roy, S. Senguptas, Laminar forced convection heat transfer in microcapsulated phase change material suspensions, Int. J. Heat Mass Transfer, 1994, 37: 593-604.

[75] S. K. Roy, S. Sengupta, An evaluation of phase change microcapsules for use in enhanced heat transfer fluids, Int. Commun. Heat Mass Transfer, 1991, 18: 495-507.

[76] Y. W. Zhang, A. Faghri, Analysis of forced convection heat transfer in microencapsulated phase change material suspensions, J. Thermophys Heat Transfer, 1995, 9: 727-723.

[77] E. L. Alisetti, Forced convection heat transfer to phase change material slurries in circular ducts, Ph.D. thesis, University of Miami, Dpt of Mech Eng, 1998.

[78] E. L. Alisetti, S. K. Roy, Forced convection heat transfer to phase change material slurries in circular ducts, J Thermophys Heat Transfer, 2000:14:115–118.

[79] S. K. Roy, B. L. Avanic, Turbulent heat transfer with phase change material suspensions, Int. J. Heat Mass Transfer, 2001, 44: 2277-2285.

[80] E. Choi, Forced convection heat transfer with water and phase-change material slurries: turbulent flow in a circular tube, Ph.D. thesis, PA: Drexel University; 1993.

[81] E. Choi, Y. I. Cho, H. G. Lorsch, Forced convection heat transfer with phase change material slurries: turbulent flow in a circular tube. Int J Heat Mass Transfer 1994,17: 207–215.

[82] X. X. Hu and Y. P. Zhang, Novel insight and numerical analysis of convective heat transfer enhancement with microencapsulated phase change material slurries: laminar flow in a circular tube with constant heat flux, Int. J. Heat Mass Transfer, 2002, 45: 3163-3172

[83] Y. Zhang, X. Hu, X. Wang, Theoretical analysis of convective heat transfer enhancement of microencapsulated phase change material slurries, Heat Mass Transfer, 2003, 40: 59–66.

[84] Y. Yamagishi, H.Takeuchi et al., Characteristics of microencapsulated PCM slurry as a heat-transfer fluid, AIChE Journal, 1999, 45: 696-707.

[85] J. L. Alvarado, C. Marsh, C. Sohn, G. Phetteplace, T. Newell, Thermal performance of microencapsulated phase change material slurry in turbulent flow under constant heat flux, Int. J. Heat Mass Transf, 2007, 50: 1938-1952.

[86] X. Wang, J. Niu, Y. Li, X. Wang, B. Chen, R. Zeng, Q. Song, Y. Zhang, Flow and heat transfer behaviors of phase change material slurries in a horizontal circular tube, Int. J. Heat Mass Transf, 2007, 50: 2480-2491.

[87] K.V. Liu, U.S. Choi, K.E. Kasza, Pressure drop and heat transfer characteristics of nearly buoyant particulate slurry for advanced energy transmission fluids, Int. Symp. Liquid–Solid Flows, 1988: 107–113.

[88] Y. Rao, F. Dammel, P. Stephan, G. Lin, Convective heat transfer characteristics of microencapsulated phase change material suspensions in minichannels, Heat Mass Transf, 2007, 44: 175-186.

[89] R. Sabbah, J. Seyed-Yagoobi, S. AI-Hallaj, heat transfer characteristics of liquid flow with micro-encapsulated phase change material: Experimental study, J. Heat Transfer, 2012, 134: 044501-1-044501-3.

[90] R. Sabbah, Numerical and Experimental Investigation of Heat Transfer

Characteristics of Liquid Flow With Micro-Encapsulated Phase Change Material, Ph.D. thesis, Mechanical, Material, and Aerospace Engineering Department, Illinois Institute of Technology, Chicago, IL, 2008.

[91] E. Assis, G. Ziskind, R. Letan, Numerical and experimental study of solidification in a spherical shell, J. Heat Transfer 131 (2009) 024502-1-024502-5.

[92] S. W. McCue, B. Wu, J. M. Hill, Classical two-phase Stefan problem for spheres, Proc. R. Soc. A, 2008, 464: 2055-2076.

[93] S. Tabakova, F. Feuillebois, S. Radev, Freezing of a supercooled spherical droplet with mixed boundary condition, Proc. R. Soc. A, 2010, 466: 1117-1134.

[94] http://arpa-e.energy.gov/Portals/0/Documents/FundedProjects/HEATS%20Slicksheets/HEATS_MIT-oncentratedSolarAndNuclear_Final.pdf

[95] C. L. Jackson, G. B. Mckenna, The melting behavior of organic materials confined in porous solids, J. Chem. Phys, 1990, 93(12): 9002-9011.

[96] J. Beau W. Webber, Studies of nano-structured liquids in confined geometries and at surfaces, Progress in Nuclear Magnetic Resonance Spectroscopy, 2010, 56: 78–93.

[97] P. Gordon, Principles of phase diagrams in materials systems, McGraw-Hill, Inc, 1968, pp. 64-65.

[98] K. C. Mills, Recommended values of thermophysical properties for selected commercial alloys, Woodhead, Cambridge, 2002, pp. 63-104.

[99] R. Kofman, P. Cheyssac, Y. Lereah, A. Stella, Melting of clusters approaching 0D, Eur. Phys. J. D, 1999, 9: 441-444.

[100] K. Shirahama, M. Kubota, S. Ogawa, et al., Size-dependent Kosterlitz-

Thouless superfluid transition in thin ^{4}He films adsorbed on porous glasses, Phys. Rev. Lett, 1990, 64: 1541–1544.

[101] Ph. Buffat, J-P. Borel, Size effect on the melting temperature of gold particles, Phys. Rev. A, 1976, 13: 2287-2298.

[102] P. R. Couchman and W. A. Jesser, Thermodynamic theory of size dependence of melting temperature in metals, Nature, 1977, 269: 481-483.

[103] F. Ehrburger and J. Lahaye, Thermoporometric study of the intra-aggregate porosity of pyrogenic silica dispersed in aqueous and non-aqueous liquids, Colloids Surf, 1987, 23: 105-117.

[104] J. D. Hoffman, G. T. Davis, J. I. Lauritzen, in Treatise on Solid-State Chemistry, edited by N. B. Hannay (Plenum, New York, 1976).

[105] G. H. Zhang, C. Y. Zhao, Thermal and rheological properties of microencapsulated phase change materials, Renewable Energy, 2011, 36: 2959-2966.

[106] Z. R. Liu, D. D. L. Chung, Calorimetric evaluation of phase change materials for use as thermal interface materials, Thermochimica Acta, 2001, 366: 135-147

[107]http://www.perkinelmer.co.uk/CMSResources/Images/44-74542GDE_DSCBeginnersGuide.pdf

[108] B. He, E.M. Gustafsson, F. Setterwall, Tetradecane and hexadecane binary mixtures as phase change materials (PCMs) for cool storage in district cooling system, Energy, 1999; 24:1015–28.

[109] B. He, V. Martin, F. Setterwall, Phase transition temperature ranges and storage density of paraffin wax phase change materials, Energy, 2004, 29:1785–1804.

[110] S. V. Patankar, Numerical heat transfer and fluid flow, Hemisphere Publishing Corporation, 1980.

[111] J. P. Holman, Heat transfer, 7th ed, in SI units, Mcgraw-HillInternational (UK) Limited, 1992.

[112] A. Bejan, Convection heat transfer, 3rd ed., John Wiley &Sons, Inc., 2004.

[113] Y. Peles, Chapter 8: Internal forced convection, The Mcgraw-Hill companies,2012.
http://wwwme.nchu.edu.tw/Enter/html/lab/lab516/Heat%20Transfer/chapter_8.pdf

[114] C. F. Colebrook, Turbulent flow in pipes, with particular reference to the transition region between smooth and rough pipe laws, Journal of the ICE, 1939, 11(4): 133-156.

[115] C. F. Colebrook, C. M. White, Experiments with fluid friction in roughened pipes, Proceedings of the Royal Society of London, Series A, Mathematical and Physical Sciences, 1937, 161(906): 367–381.

[116]http://www.engineeringtoolbox.com/water-thermal-properties-d_162.html.

[117] http://www.kayelaby.npl.co.uk/general_physics/2_3/2_3_6.html.

[118] E. N. Sieder, C. E. Tate, Heat transfer and pressure drop of liquids in Tubes, Ind. Eng. Chem., 1936, 28: 1429

[119] B. S. Petukhov, Heat transfer and friction in turbulent pipe flow with variable physical properties, in J. P. Hartnett and T. F. Irvine, (eds.), “Advances in heat transfer” Academic Press, Inc., New York, 1970, pp. 504-564.

[120] C. Binjiao, W. Xin, Z. Ruolang, *et al*., Experimental research on laminar forced convection heat transfer characteristics of microencapsulated phase change material suspension, Acta energiae solaris sinica, 2009, 30 (8): 1018-1022.

[121] S. K. Roy, B. L. Avanic, Laminar forced convection heat transfer with phase change material suspensions, Int. Comm. Heat Mass Transfer, 2001, 28(7): 895-904.

[122] P. Keblinski, S.R. Phillpot, S.U.S. Choi, J.A. Eastman, Mechanisms of heat flow in suspensions of nano-sized particles (nanofluids), Int. J. Heat Mass Transfer, 2002, 45: 855-863

[123] V. Gnielinski, New equations for heat and mass transfer in turbulent pipe and channel flow, Int. Chem. Eng., 1976, 16: 359-368.

[124] M. Freund, R. CsikÓs, S. Keszthelyi, G. Y. MÓzes, Paraffin products Properties, technologies, applications, Developments in Petroleum Science 14, Elsevier Scientific Publishing Company Amsterdam-Oxford-New York 1982.

[125] X. Z. Lan, Z. C. Tan, G. L. Zou et al., Microencapsulation of *n*-Eicosane as energy storage material**,** Chinese Journal of Chemistry, 2004, *22*: 411-414.

[126] C. Alkan, A. Sar, A. Karaipekli, Preparation, thermal properties and thermal reliability of microencapsulated *n*-eicosane as novel phase change material for thermal energy storage, Energy Conversion and Management, 2011, 52: 687–692.

[127] E. M. Alawadhi, Using wax in window external shutter to reduce the solar heat gain through it, Proceedings of the “International Conference on

Solar energy for MENA region (INCOSOL)". Amman, Jordan, 22-23 October 2012.

[128] P. Yi, G. C. Rutledge, Molecular simulation of bundle-like crystal nucleation from n-eicosane melts, The Journal of Chemical Physics, 2011, 135: 024903-1-11.

[129] F. A. Holland, R. Bragg, Fluid flow for Chemical Engineers, Elsevier Ltd, 1995.

[130] A. B. Metzner, J. C. Reed, Flow of non-Newtonian fluids - correlation of the laminar, transition, and turbulent-flow regimes, AIChE Journal, 1955, 1: 434-440.

[131] N. W. Ryan, M. M. Johnson, Transition from laminar to turbulent flow in pipes, AIChE Journal, 1959, 5: 433-435.

[132] D. W. Dodge, A. B. Metzner, Turbulent flow of non-Newtonian systems AIChE Journal, 1959, 5: 189-204.

[133] A. H. P. Skelland, Non-Newtonian flow and heat transfer, New York, John Wiley and Sons Inc, 1967.

[134] http://hyperphysics.phy-astr.gsu.edu/hbase/tables/thrcn.html

[135] D. Huber, H. Walter, Forced convection heat transfer in the transition region between laminar and turbulent flow for a vertical circular tube, Latest Trends on Theoretical and Applied Mechanics, Fluid Mechanics and Heat & Mass Transfer, International Conference on Fluid Mechanics and Heat & Mass Transfer, Greece, 2010, 132-136.

[136] B. S. Petukhov and V. V: Kirillov, To the question of heat transfer in turbulent pipe flow of liquids in tubes (Zur Frage des Wärmeübergangs bei

turbulenter Strömung von Flüssigkeiten in Rohren), Teploenergetika, 1958, 4(4): 63-68.

[137] V. Gnielinski, V., New equations for heat and mass transfer in turbulent pipe and channel flow (Neue Gleichungen für den Wärme- und den Stoffübergang in turbulent durchströmten Rohren und Kanälen), *Forschung im Ingenieurwesen*, 1975, 41(1): 8–16.

[138] V. Gnielinski, V., A new calculation procedure for the heat transfer in the transition region between laminar and turbulent pipe flow (Ein neues Berechnungsverfahren für die Wärmeübertragung im Übergangsbereich zwischen laminarer und turbulenter Rohrströmung),” Forschung im Ingenieurwesen, 1995, 61(9): 240-248.

[139] H. Zhang, X. Wang. Fabrication and performances of microencapsulated phase change materials based on n-octadecane core and resorcinol-modified melamine-formaldehyde shell, Colloids and Surfaces A: Physicochemical and Engineering Aspects, 2009, 332: 129-38.

Appendix: Publications related to this work

[1] **J. Yang**, C. Y. Zhao, D. Hutchins. Modelling the effect of binary phase composition on inward solidification of a particle. International Journal of Heat and Mass Transfer, Elsevier Science. 2012, 55: 6766-6744.

[2] **J. Yang**, C. Y. Zhao. Solidification analysis of a single particle with encapsulated phase change materials. Applied Thermal Engineering, Elsevier Science. 2013, 51: 338-346.

[3] **J. Yang**, D. Hutchins, G. H. Zhang, C. Y. Zhao. Experimental investigation of microcapsule phase change slurry as a heat transfer fluid. Manuscript in preparation.

[4] **J. Yang**, D. Hutchins, C. Y. Zhao. Melting behaviour of differently-sized micro-particles in a pipe flow under constant heat flux. Manuscript in preparation.